ABSTRACT

Title of Dissertation:	FUNCTIONALIZED THIN-FILM SHAPE MEMORY ALLOYS FOR NOVEL MEMS APPLICATIONS
	Sabrina M. Curtis, Doctor of Philosophy and Doctor of Engineering, 2023
Dissertation co-directed by:	Prof. Ichiro Takeuchi, Materials Science and Engineering, University of Maryland Prof. Eckhard Quandt, Faculty of Engineering, Kiel University

Nickel-titanium (NiTi) shape memory alloy (SMA) films are already implemented into microelectromechanical system (MEMS) devices such as sensors, actuators, and implantable medical devices. In this thesis, I used DC magnetron sputter deposition to study the influence of film composition, microstructure, and annealing conditions on the stability of the phase transformation for the NiTi-based SMA thin films TiNiCu, TiNiCuCo, and TiNiHf. SMAs are a type of smart material that can undergo stress or temperature-induced solid-to-solid phase transformation between two different crystalline phases. In NiTi-based SMAs, the two phases are known as martensite with a monoclinic crystalline structure and austenite with a cubic crystal structure. The temperature-induced phase transformations can be used to switch between the martensite and austenite phases, and thus switch between two sets of material properties in the SMA. For example, in NiTi-based SMAs the Young's modulus, electrical resistivity, and coefficient of thermal expansion of the austenite phase are typically 2X larger than that of the martensite phase. The transformation temperatures, recovery strains, enthalpy of transformation, and fatigue properties of NiTi SMAs can be tuned by alloying NiTi with other elements like copper

(Cu), cobalt (Co), and hafnium (Hf). For example, certain compositions of sputtered TiNiCu and TiNiCuCo are known to be ultra-low fatigue SMAs, able to reversibly undergo the phase transformation for 10+ million cycles without degradation in the mechanical or thermal properties. The primary focus of this thesis was the integration of these sputtered NiTi-based SMA thin-films into the following four novel MEMS devices: 1) TiNiCu for magneoelectric sensors, 2) TiNiHf for bistable actuators, 3) TiNiCuCo for stretchable electronics and 4) thin-film SMA stretchable auxetic structures for wearable and implantable medical devices.

The shape memory effect was observed in TiNiCu and TiNiHf films when the film thickness and lateral dimensions are downscaled to micro and nano dimensions. In the research publication "Integration of AlN piezoelectric thin films on ultralow fatigue TiNiCu shape memory alloys.", I showed the reproducibility of the thermal-induced phase transformation of $Ti_{50}Ni_{35}Cu_{15}$ is attractive for integration into MEMS devices that require a high cycle lifetime. I explained how the SMA's phase transformation can be used to tune the resonant of bending cantilever-type sensors like magnetoelectric sensors. I also demonstrated excellent thin-film piezoelectric and shape memory alloy properties for 2 μm AlN/ 5 μm TiNiCu films composites deposited onto silicon substrates. The large work densities and high strength-to-weight ratio offered by SMAs are attractive for the development of micro and nano actuators. The thermal-induced phase transformation between martensite and austenite is also used to develop bi-directional micro-actuators with TiNiHf/Si and TiNiHf/SiO_2/Si composites. In another research publication, "TiNiHf/SiO_2/Si shape memory film composites for bi-directional micro actuation", I demonstrated the influence of film thickness and substrate on the phase transformation properties of TiNiHf thin-films. $Ti_{40.4}Ni_{48}Hf_{11.6}$ films with thicknesses as low as 220 nm on SiO_2/Si substrates can undergo the phase transformation with high transformation temperatures (A_s > 100 °C) and a

wide thermal hysteresis ($\Delta T > 50$ °C). In this publication, we explain how the wide hysteresis and high transformation temperature obtained in TiNiHf films can be used to develop micro and nano-scale bistable actuators based on PMMA/TiNiHf/Si composites.

Even though thin-film NiTi-based SMAs are known to reversibly recover superelastic strains of up to 8%, surprisingly, they have not yet been exploited in the growing field of stretchable electronics. In the technical article "Thin-Film Superelastic Alloys for Stretchable Electronics" I demonstrate the first experimental and numerical studies of freestanding thin-film superelastic TiNiCuCo structured into a serpentine geometry for use as stretchable electrical interconnects. Fabricated electropolished serpentine structures were demonstrated to have low fatigue after cycling external strains between 30% - 50% for 100,000 cycles. The electrical resistivity of the austenite phase of a $Ti_{53.3}Ni_{30.9}Cu_{12.9}Co_{2.9}$ thin-film at room temperature was measured to be 5.43×10^{-7} Ω m, which is larger than reported measurements for copper thin-films (1.87×10^{-8} Ω m). Expanding upon this work, in the conference proceedings paper "Auxetic Superelastic TiNiCuCo Sputtered Thin-Films for Stretchable Electronics", I present a new platform for functionalized wearable electronics and implantable medical devices based on superelastic thin-film SMA substrates structured into novel stretchable auxetic geometries. Since thin-film SMAs are conductive, the structured substrate itself could serve as the current collector for such stretchable and flexible devices, or a more conductive electrode can be deposited on top of the stretchable auxetic SMA substrate. Overall, the results discussed in this doctoral thesis look to the future of harnessing the functional properties of thin-film sputtered SMAs for novel uses in next-generation MEMS devices.

FUNCTIONALIZED THIN-FILM SHAPE MEMORY ALLOYS FOR NOVEL MEMS APPLICATIONS

by

Sabrina M. Curtis

Dissertation submitted to the Faculty of the Graduate School of the
University of Maryland, College Park, in partial fulfillment
of the requirements for the degree of
Doctor of Philosophy
2023

Advisory Committee:

Professor Ichiro Takeuchi, Committee Co-chair
Prof. Dr.-Ing. Eckhard Quandt, Committee Co-chair
Prof. Dr.-Ing. Rainer Adelung
Professor Alison Flatau,
Prof. Dr.-Ing. Lorenz Kienle
Assistant Professor Carlos Rios Ocampo
Prof. Dr.-Ing Stephan Wulfinghof

ZUSAMMENFASSUNG

Titel der Dissertation:	Funktionalisierte Dünnschicht-Formgedächtnislegierungen für neuartige MEMS-Anwendungen
	Sabrina M. Curtis, Doctor of Philosophy and Doctor of Engineering, 2023
Dissertation unter der Leitung von:	Prof. Ichiro Takeuchi, Materials Science and Engineering, University of Maryland Prof. Eckhard Quandt, Faculty of Engineering, Kiel University

Schichten aus Nickel-Titan (NiTi)-Formgedächtnislegierungen (SMA) werden bereits in mikroelektromechanischen Systemen (MEMS) wie Sensoren, Aktoren und implantierbaren medizinischen Geräten eingesetzt. Im Rahmen dieser Arbeit nutzte ich DC-Magentronsputterabscheidung, um den Einfluss der Schichtzusammensetzung, der Mikrostruktur und der Glühbedingungen auf die Stabilität der Phasenumwandlung für die NiTi-basierten SMA-Dünnschichten TiNiCu, TiNiCuCo und TiNiHf zu untersuchen. SMAs sind eine eine Gruppe von intelligenten Materialien, die eine spannungs- oder temperaturinduzierte Festkörperphasenumwandlung zwischen zwei verschiedenen kristallinen Phasen durchlaufen können. Für SMAs auf NiTi-Basis wird die monokline Phase als Martensit und die kubische Phase als Austenit bezeichnet. Die temperaturbedingten Phasenumwandlungen können genutzt werden, um zwischen der Martensit- und der Austenitphase - und damit zwischen zwei Arten von Werkstoffeigenschaften im SMA - zu wechseln. In der Regel sind der Elastizitätsmodul, der elektrische Widerstand und der Wärmeausdehnungskoeffizient beispielsweise um das Zweifache größer in der Austenitphase als der der Martensitphase für SMAs auf NiTi-Basis. Die

Umwandlungstemperaturen, Erholungsdehnungen, Umwandlungsenthalpien und Ermüdungseigenschaften von NiTi-SMAs können durch Legierung von NiTi mit anderen Elementen wie Kupfer (Cu), Kobalt (Co) und Hafnium (Hf) angepasst werden. So sind beispielsweise bestimmte Zusammensetzungen von gesputtertem TiNiCu und TiNiCuCo als extrem ermüdungsarme SMAs bekannt, die eine reversible Phasenumwandlung über mehr als 10 Millionen Zyklen ohne Verschlechterung der mechanischen oder thermischen Eigenschaften durchlaufen können. Das Hauptaugenmerk dieser Arbeit lag auf der Integration dieser gesputterten SMA-Dünnschichten auf NiTi-Basis in die folgenden vier neuen MEMS-Bauteile: 1) TiNiCu für magnetoelektrische Sensoren, 2) TiNiHf für bistabile Aktoren, 3) TiNiCuCo für dehnbare Elektronik und 4) dehnbare SMA-Dünnfilmhilfsstrukturen für tragbare und implantierbare medizinische Geräte.

Dass der Formgedächtniseffekt in TiNiCu- und TiNiHf-Filmen wurde beobachtet wenn die Filmdicke und die lateralen Abmessungen auf Mikro- und Nanodimensionen herunterskaliert werden. In der Forschungspublikation "Integration of AlN piezoelectric thin films on ultralow fatigue TiNiCu shape memory alloys" (Integration von piezoelektrischen AlN-Dünnschichtenauf TiNiCu-Formgedächtnislegierungen mit extrem geringer Ermüdung) habe ich gezeigt, dass die Reproduzierbarkeit der thermisch induzierten Phasenumwandlung von $Ti_{50}Ni_{35}Cu_{15}$ für die Integration in MEMS-Bauteile, die eine hohe Zykluslebensdauer erfordern, attraktiv ist. Ich habe gezeigt, wie die Phasenumwandlung von SMAs genutzt werden kann, um die Resonanz von Cantilever-Biegesensoren wie magnetoelektrischen Sensoren abzustimmen. Außerdem habe ich hervorragende Eigenschaften von piezoelektrischen Dünnschichten und Formgedächtnislegierungen für 2 µm AlN/ 5 µm TiNiCu-Filme nachgewiesen, die auf Siliziumsubstraten abgeschieden wurden. Die große Arbeitsdichte und das hohe Verhältnis von

Festigkeit zu Gewicht, die SMAs bieten, sind für die Entwicklung von Mikro- und Nanoaktuatoren attraktiv.

Die thermisch induzierte Phasenumwandlung zwischen Martensit und Austenit wird auch zur Entwicklung bidirektionaler Mikroaktuatoren mit TiNiHf/Si und TiNiHf/SiO_2/Si Verbundwerkstoffen genutzt. In einer weiteren Forschungspublikation, "TiNiHf/SiO_2/Si shape memory film composites for bi-directional micro actuation" (TiNiHf/SiO_2/Si Formgedächtnisfilm-Verbundwerkstoffe für bidirektionale Mikrobetätigung), habe ich den Einfluss von Schichtdicke und Substrat auf die Phasenumwandlungseigenschaften von TiNiHf-Dünnschichten aufgezeigt. $Ti_{40.4}$ Ni $Hf_{4811.6}$ -Filme mit einer Dicke von nur 220 nm auf SiO_2 /Si-Substraten können die Phasenumwandlung mit hohen Umwandlungstemperaturen (A_s > 100 °C) und einer großen thermischen Hysterese (ΔT > 50 °C) durchlaufen. In dieser Veröffentlichung erläutern wir, wie die große Hysterese und die hohe Umwandlungstemperatur von TiNiHf-Filmen genutzt werden können, um bistabile Mikro- und Nanoaktoren auf der Basis von PMMA/TiNiHf/Si-Verbundwerkstoffen zu entwickeln.

Obwohl Dünnschicht-SMAs auf NiTi-Basis dafür bekannt sind, superelastische Dehnungen von bis zu 8 % reversibel wiederherzustellen, wurden sie überraschenderweise noch nicht im wachsenden Bereich der dehnbaren Elektronik eingesetzt. In dem technischen Artikel "Thin-Film Superelastic Alloys for Stretchable Electronics" (Dünnschicht-Superelastische Legierungen für dehnbare Elektronik) zeige ich die ersten experimentellen und numerischen Studien von freistehenden dünnen superelastischen TiNiCuCo-Filmen, die in einer Serpentinengeometrie für den Einsatz als dehnbare elektrische Verbindungen strukturiert sind. Die hergestellten elektropolierten Serpentinenstrukturen weisen eine geringe Ermüdung auf, nachdem sie 100.000 Zyklen lang äußeren Belastungen zwischen 30 % und 50 % ausgesetzt waren. Bei

Raumtemperatur wurde ein elektrischer Widerstand der Austenitphase eines $Ti_{53.3}Ni_{30.9}Cu_{12.9}Co_{2.9}$ Dünnfilms von $5{,}43 \times 10^{-7}$ Ω m gemessen, womit dieser größer ist als die gemeldeten Messungen für Kupferdünnfilme ($1{,}87 \times 10^{-8}$ Ω m). Aufbauend auf dieser Arbeit stelle ich in dem Konferenzbeitrag "Auxetic Superelastic TiNiCuCo Sputtered Thin-Films for Stretchable Electronics" (Auxetische Superelastische Gesputterte TiNiCuCo-Dünnschichten für Dehnbare Elektronik) eine neue Plattform für funktionalisierte tragbare Elektronik und implantierbare medizinische Geräte vor, die auf superelastischen Dünnfilm-SMA-Substraten basiert, die in neuartigen dehnbaren auxetischen Geometrien mit Dehnungsreduzierung strukturiert sind. Da Dünnfilm-SMAs leitfähig sind, könnte das strukturierte Substrat selbst als Stromkollektor für solche dehnbaren und flexiblen Geräte dienen, oder es kann eine leitfähigere Elektrode auf das dehnbare auxetische SMA-Substrat aufgebracht werden. Insgesamt geben die in dieser Dissertation diskutierten Ergebnisse einen Ausblick auf die Zukunft der Nutzung der funktionalen Eigenschaften von gesputterten Dünnfilm-SMAs für neuartige Anwendungen in MEMS-Bauteilen der nächsten Generation.

Functionalized Thin-Film Shape Memory Alloys for Novel MEMS Applications

in partial fulfillment of the requirements for the degree of
Doctor of Engineering
(Dr.-Ing.)

Dissertation by

Sabrina M. Curtis
from
Denver, CO, USA

Submitted to the Faculty of Engineering of
Christian-Albrechts-Universität zu Kiel

Kiel, May 2023

FUNCTIONALIZED THIN-FILM SHAPE MEMORY ALLOYS FOR NOVEL MEMS APPLICATIONS

by

Sabrina M. Curtis

Dissertation submitted to both the Faculty of the Graduate School of the University of Maryland, College Park, in partial fulfillment of the requirements for the degree of Doctor of Philosophy (Ph.D.)

and

Faculty of Engineering of Christian-Albrechts-Universität zu Kiel in partial fulfillment of the requirements for the degree of Doctor of Engineering (Dr.-Ing.)

2023

	Date of oral examination: 02.03.2023
Examiners	Prof. Ichiro Takeuchi
	Prof. Dr.-Ing. Eckhard Quandt

Eidesstattliche Erklärung

Ich versichere hiermit an Eides statt, dass ich die vorliegende Dissertation selbstständig und ohne unzulässige fremde Hilfe erbracht habe. Ich habe keine anderen als die angegebenen Quellen und Hilfsmittel benutzt sowie wörtliche und sinngemäße Zitate kenntlich gemacht. Die Arbeit hat in gleicher oder ähnlicher Form noch keiner Prüfungsbehörde vorgelegen. Der Inhalt der Arbeit wurde in Teilen bereits in meinen wissenschaftlichen Publikationen veröffentlicht. Dies ist in der Arbeit entsprechend vermerkt. Die Arbeit ist nach bestem Wissen und Gewissen konform mit den Regeln guter wissenschaftlicher Praxis, welche durch die Deutsche Forschungsgemeinschaft festgelegt sind. Außerdem ist mir noch nie ein akademischer Grad entzogen worden.

Silver Spring, MD, 19.05.2023

Ort, Datum

Sabrina M. Curtis

Digitally signed by Sabrina M. Curtis
DN: C=US, O=Kharpur R&D, CN=Sabrina M. Curtis, E=sabrina@kharpur.com
Reason: I am approving this document with my legally binding signature
Location: Silver Spring, MD
Date: 2023.05.19 16:33:57-04'00'
Foxit Reader Version: 10.1.1

Sabrina M. Curtis

Foreword

I, Sabrina M. Curtis, participated in a bi-national doctoral degree between Kiel University (Germany) and University of Maryland (USA) from August 2018 – March 2023. I was co-advised by Prof. Ichiro Takeuchi at the University of Maryland and Prof. Eckhard Quandt at Kiel University. To complete this bi-national doctoral thesis, I was a member of the Inorganic Functional Materials research group at the Faculty of Engineering at Kiel University, led by Prof. Eckhard Quandt. Our group primarily uses the Kiel Nanolabor to develop MEMS sensors, actuators, and medical devices using magentostrictive, piezoelectric, and shape memory alloy smart materials. I was also a member of the research group led by Prof. Ichiro Takeuchi in the Materials Science and Engineering Department at the University of Maryland. As a member of his research group, I used the FabLab at University of Maryland and the cleanroom at the U.S. Army Research Lab (Adelphi, MD) to build micro and nanodevices based on silicon technologies. I split time between these two research groups in Germany and the USA during my bi-national doctoral thesis to research and develop thin-film shape memory alloys for novel MEMS applications.

To complete the experiments presented in this thesis, I participated in two Deutsche Forschungsgemeinschaft (DFG) funded programs. The Collaborative Research Centre (CRC 1261 – Magnetoelectric Sensors: From Composite Materials to Biomagnetic Diagnostics) (2018) and the Special Priority Program (SPP 2206 - Cooperative Multistage Multistable Microactuator Systems) (2019-2022). Furthermore, my work was supported by the National Science Foundation Graduate Research Fellowship Program (NSF GRFP) (2018-2022).

The outcomes included in this thesis present the results on the research projects that I primarily lead during my doctoral studies between August 2018 – March 2023. The examining committee agrees that I have made a substantial contribution to the following three peer-reviewed, co-authored works. The following works were accomplished via collaborations between researchers from several research institutions and a company including Kiel University, the University of Maryland, the Army Research Lab, Karlsruhe Institute of Technology, and Acquandas. My direct contributions to the following peer-reviewed, co-authored, works can be found in Section 1.2 “Ph.D. Thesis Research Contributions”.

1. **Curtis, S.M.,** Wolff, N., Dengiz, D., Lewitz, H., Jetter, J., Bumke, L., Hayes, P., Yarar, E., Thormählen, L., Kienle, L., Meyners, D., and Quandt, E., (2020) Integration of AlN piezoelectric thin films on ultralow fatigue TiNiCu shape memory alloys. Journal of Materials Research, 35(10), pp.1298-1306. *Invited Feature Paper*
2. **Curtis, S.M.,** Sielenkämper, M., Arivanandhan, G., Dengiz, D., Li, Z., Jetter, J., Hanke, L., Bumke, L., Quandt, E., Wulfinghoff, S. and Kohl, M., (2022) TiNiHf/SiO_2/Si shape memory film composites for bi-directional micro actuation. International Journal of Smart and Nano Materials, 13(2), pp. 293-314.
3. **Curtis, S.M.,** Gugat, J.L., Bumke, L., Dengiz, D., Seigner, L., Schmadel, D., Lazarus, N.S., and Quandt, E. (2023) “Thin-Film Superelastic Alloys for Stretchable Electronics” *Shape Memory and Superelasticity,* pp. 1-15, *Invited Feature Paper*

Letter from Dissertation Co-Advisors

1242 Jeong H. Kim Engineering Building
College Park, MD 20742

October 6st, 2022

Dean of the Graduate School

Prof. Jason Farman
123 Lee Building
7809 Regents Drive
College Park, MD 20742

Dear Prof. Jason Farman,

The research results presented in the doctoral thesis "Functionalized Thin-Film Shape Memory Alloys for Novel MEMS Applications" reflect the findings of Sabrina M. Curtis, during her bi-national Ph.D. between Kiel University and University of Maryland from 2018 – 2022. The core topic of her Ph.D. thesis was to investigate the integration of sputtered thin-film shape memory alloys into novel microelectromechanical (MEMS) devices such as sensors, actuators, and stretchable electronics. This work was co-supervised by Prof. Eckhard Quandt, Vice President of Research at Kiel University, and myself, Prof. Ichiro Takeuchi, Director of the Graduate Program of Materials Science and Engineering at University of Maryland. Prof. Eckhard Quandt and I both have extensive research experience in the field of shape memory alloys. The doctoral examining committee has determined that Ms. Curtis has made a substantial contribution to the following three works:

1. **Curtis, S.M.,** Wolff, N., Dengiz, D., Lewitz, H., Jetter, J., Bumke, L., Hayes, P., Yarar, E., Thormählen, L., Kienle, L., Meyners, D., and Quandt, E., (2020). Integration of AlN

piezoelectric thin films on ultralow fatigue TiNiCu shape memory alloys. *Journal of Materials Research,* 35(10), pp. 1298-1306. *Invited Feature Paper*

2. **Curtis, S.M.,** Sielenkämper, M., Arivanandhan, G., Dengiz, D., Li, Z., Jetter, J., Hanke, L., Bumke, L., Quandt, E., Wulfinghoff, S. and Kohl, M., (2022). TiNiHf/SiO_2/Si shape memory film composites for bi-directional micro actuation. *International Journal of Smart and Nano Materials*, 13(2), pp. 293-394.
3. **Curtis, S.M.,** Gugat, J.L., Bumke, L., Dengiz, D., Seigner, L., Schmadel, D., Lazarus, N.S., and Quandt, E. (2023) "Thin-Film Superelastic Alloys for Stretchable Electronics" *Shape Memory and Superelasticity*, pp. 1-15, *Invited Feature Paper*

As the primary co-supervisors of Ms. Curtis' doctoral thesis research, we attest with this letter that she has made substantial contributions to the co-authored, peer-reviewed publications described in this dissertation. The inclusion of this work has the approval of the dissertation advisors, the materials science and engineering department chair, Prof. JC Zhao, and the Graduate Program Director.

Sincerely,

Prof. Ichiro Takeuchi 

(Graduate Program Director and Co-Advisor)

and

Prof. Eckhard Quandt 

(Co-Advisor)

Acknowledgments:

I am grateful to my research co-advisors Prof. Ichiro Takeuchi and Prof. Dr.-Ing. Eckhard Quandt for giving me the fantastic opportunity to pursue a bi-national Ph.D. between University of Maryland (USA) and Kiel University (Germany). Both advisors provided me with the opportunity, financial means, creative freedom, and the ability to pursue my own scientific pathways. They granted me the autonomy to dictate my time and experiments as if I was the PI of my project. They both supported my formation of international collaborations and government collaborations to bring my ideas to reality. I very much enjoyed splitting my time between both of their working groups.

Prof. Ichiro Takeuchi was the first person to recognize my research scientific abilities and suggest to me that I should consider going to graduate school while I was still an undergraduate back in 2015. He allowed me to conduct independent research during my Ph.D. while offering his mentorship, guidance, and support every step of the way. I also very much appreciate his support for my new startup company! I look forward to continuing to collaborate with Ichiro in the future.

Prof. Dr.-Ing. Eckhard Quandt provided me with the amazing opportunity to conduct scientific research in Germany for four years. I appreciate that Eckhard gave me the chance to serve as a “team leader” on the DFG SPP 206 project. As the team leader of this project, I directed the experiments of three Ph.D. colleagues that collaborated on the project with me, I hired and mentored over 10 bachelor and master students and supervised three master’s theses. As a member of his research group, I also had the chance to attend over 15 international scientific meetings, including conferences, workshops, and DFG focus group meetings. The Lindau Nobel Laureate Meeting was the most notable meeting I attended, thanks directly to the support of Eckhard.

I would like to thank the other doctoral thesis committee members for supporting the first bi-national Ph.D. between Kiel University and University of Maryland. I appreciate the experimental suggestions, guidance, feedback, and fertile discussions I gained from Prof. Stephan Wulfinghoff, Prof. Lorenz Kienle, Prof. Alison Flatau, Prof. Carlos Rios Ocampo, Prof. Rainer Adelung, and Prof. Hugh Bruck.

Prof. Nathan Lazarus and Dr. Don Schmadel have been my unofficial research mentors for the last six years. I credit and thank both of them for molding me into the scientist that I am today.

I thank Dr. rer. nat. Dirk Meyners, Dr. Heather Cavers, Dr.-Ing. Christine Kirchhof, Boris Kirchhof-Gudschun, M.Sc. Lisa Hanke, M.Sc. Hanna Lewitz, Carola Block, and Gislinde Schröder for their friendship, mentorship on how to navigate a Ph.D., and for making me feel welcome in Kiel.

I thank my colleagues Dr.-Ing. Patrick Hayes, M.Sc. Lisa Hanke, M.Sc. Hanna Lewitz, M.Sc. Lars Bumke, M.Sc. Lars Thormählen, M.Sc. Lea Jessen, Dr.-Ing. Prasanth Velvaluri, M.Sc. Justin Jetter, Dr.-Ing. Viktor Schell, Dipl.-Ing. Thomas Metzing, and Dr. rer. nat. Antonio Malavé for sharing their extensive knowledge about smart materials with me. These colleagues taught me certain fabrication steps and characterization tools and engaged me in fruitful discussions about the results. I would also like to thank the following fantastic research students that I mentored during my Ph.D., including M.Sc. Parikshit Manahor, Bobby Cozzette, and Meryem Gunes Ersahin. I would also like to thank the three master's thesis students that I directly supervised- M.Sc. Afrin Shara, M.Sc. Akpobome Onojeta, and M.Sc. Duygu Dengiz,

I thank Dr.-Ing. Christoph Bechthold, Dr.-Ing. Christoph Chluba, Dr.-Ing. Jascha Lukas Gugat, and Dr. Rodigo Lima de Miranda at Acquandas GmbH (www.acquandas.com) for sharing their knowledge about shape memory alloy thin-films with me.

I thank M.Sc. Rebecca Fedderwitz, Dr. Haotian Wang, M.Sc. Gabriel Smith, M.Sc. Josh Tyler, M.Sc. Abimael Santos, M.Sc. Austin Thomas, and M.Sc. Justin Pearson for their friendship and support while we struggled through classes together at University of Maryland at the beginning of my studies. I also appreciate their continued support, friendship, and encouragement to wrap up this Ph.D.!

I also would like to acknowledge the contributions of colleagues from other research groups and Universities in Germany, including Dr.-Ing. Niklas Wolff, M.Sc. Marian Sielenkämper, M.Sc. Gowtham Arivanandhan, M.Sc. Li Zixiong, M.Sc. Lena Seigner, M.Sc. Julian Kunze, and their research advisors Prof. Lorenz Kienle, Prof. Stephan Wulfinghoff, and Prof. Manfred Kohl.

Special thanks to my beloved partner- M.Sc. James Raymond, encouraging parents, family, friends, and business partners at Khanjur R&D, Nichole Adler, and David White. I couldn't have done it without all these amazing people in my life!

The work in this thesis led me to co-found a startup company, Khanjur R&D, established in August 2022. Check us out if you are interested in learning more (or potentially collaborating!) on projects similar to the work conducted in this thesis. www.khanjur.com, sabrina@khanjur.com

Table of Contents

List of Figures

List of Tables

Chapter 1. Ph.D. Thesis Motivation, Research Contributions and Chapter Organization

1.1 Ph.D. Thesis Motivation:

The research presented in this doctoral thesis aims to integrate thin-film shape memory alloys into novel nano- and micro- scale microelectromechanical systems (MEMS) devices such as sensors, actuators, and wearable electronics. Shape memory alloys (SMAs) are smart materials with a plethora of advantageous material properties including a large workout per unit volume and a large energy density. SMAs are famous for their ability to recover large intrinsic stresses/strains which allows them to "remember" a macroscopic shape. This property arises due to a stress-induced or temperature-induced solid-to-solid phase transformation between a martensite and austenite phase in the SMA material [1]. The most studied and commercially available SMA material is binary nickel-titanium (NiTi) and is implemented into numerous applications such as medical stents [2], self-sensing actuators [3, 4], and elastocaloric cooling technologies [5] in bulk form (e.g. wires, plates, tubes). SMAs have several material characteristics that make them attractive for integration into several industries including biomedical, aerospace, automotive, and the emerging field of elastocaloric cooling.

The unique properties offered by SMAs are scalable when the material is down-scaled in lateral dimensions and film thickness from micro to nano dimensions [6, 7]. In the last ~25 years, sputtered thin-film SMAs have gained attention for use in MEMS devices because high-quality polycrystalline thin films can be sputter deposited and structured onto standard MEMS substrates such as silicon [8]. Through photolithography or E-beam lithography, sputtered SMAs can be micro and nano-structured into virtually any desired geometry through lift-off and wet-chemical

etching methods. For example, nanoscale SMA/silicon bimorph actuators can be fabricated using sputter deposition and standard silicon etching techniques with silicon-on-insulator substrates [9]. There are several examples of clever fabrication schemes used to integrate sputtered NiTi thin-films into MEMS devices such as sensors and actuators [1, 6, 9, 10].

In 2012, *Lima de Miranda* at Kiel University (now Acquandas) developed a MEMS-compatible fabrication process that allows the development of freestanding SMA films with relatively low film stresses at thicknesses between 5 μm – 80 μm [11, 12]. Photolithography is used to structure the shape memory alloy into any desired 2D geometry with lateral feature sizes as small as 10 μm for standard photolithography devices [11, 12]. Wet chemical etching of a sacrificial layer allows for the release of the structured amorphous freestanding SMA film from the silicon wafer. To induce the shape memory effect, amorphous NiTi-based SMAs must be crystallized by annealing the film in a vacuum at temperatures between 500 °C – 800 °C. An advantage to using this process is 2D amorphous freestanding SMA films can be programmed to "remember" a 3D shape by annealing the film around an object of the desired 3D shape. Proper selection of time and temperature of the annealing step is critical as it determines the microstructure of the SMA [13] which is known to be directly related to the functional and structural fatigue properties of SMAs [14]. This fabrication process is primarily used to develop freestanding SMAs for micro-actuators [12, 15], medical devices such as self-expanding flow diverter stents [16], and functionalized stents with bioelectrodes [17]. The results presented below in my doctoral thesis are the first use of this fabrication process to create freestanding SMAs for use in the field of flexible and stretchable electronics.

While thin-film binary NiTi has already found several uses in MEMS devices, NiTi has cycling limitations and typical operating temperatures of a maximum of 100 °C, which reduce its

potential applications. The fatigue and transformation properties (e.g., strain, stress, transition temperatures, thermal hysteresis) of NiTi SMAs are dependent on the microstructural characteristics of the material which can be engineered by tuning the annealing parameters based on the material's composition. Additionally, these functional shape memory properties can be significantly adjusted by alloying NiTi with other elements (e.g., Cu, Hf, Co). When the composition and annealing parameters are properly selected, certain SMAs like TiNiCu and TiNiCuCo can display ultra-low fatigue functional properties [18].

My doctoral thesis research over the last 4 years has optimized and characterized the material properties of several compositions of the sputtered thin-film SMAs TiNiCu [19], TiNiHf [20], and TiNiCuCo [21]. I studied the thermo-mechanical and structural properties of freestanding SMA films and compared these properties to SMA thin-films on silicon substrates. My doctoral thesis research evaluated their use for several MEMS applications such as magnetoelectric sensors, bi-directional and bistable actuators, and stretchable electronics. In an additional chapter, I also describe the results of freestanding SMAs structured into novel stretchable auxetic SMA substrates that could be used for wearable and implantable medical devices. Finally, in the Summary and Outlook Chapter, I propose a few examples of how stretchable auxetic SMA substrates can be functionalized with other sputtered materials to develop novel stretchable power electronic devices (e.g. solar cells, energy harvesters, and batteries).

1.2 Ph.D. Thesis Research Contributions

This thesis is based on the works of three peer review, co-authored publications. Additionally, the work of one conference proceeding extended abstract is expanded upon. Below is a summary of the direct research contributions I made to each of the following works.

1. **Curtis, S.M.,** Wolff, N., Dengiz, D., Lewitz, H., Jetter, J., Bumke, L., Hayes, P., Yarar, E., Thormählen, L., Kienle, L., Meyners, D., and Quandt, E., (2020). Integration of AlN piezoelectric thin films on ultralow fatigue TiNiCu shape memory alloys. *Journal of Materials Research*, 35, pp. 1298-1306. *Invited Feature Paper* https://doi.org/10.1557/jmr.2020.106

This peer-reviewed manuscript presents a MEMS-based fabrication route to build magnetoelectric composites onto ultra-low fatigue TiNiCu shape memory alloy (SMA) thin-films on Si substrates. Since AlN is a high-temperature stable piezoelectric material, the presented fabrication route allows for rapid thermal annealing of the TiNiCu to 700 °C either (i) before AlN deposition or (ii) after AlN deposition. I explored the fabrication processing differences on the mechanical and electrical performance of AlN/ TiNiCu/ Si composites through a variety of SMA and piezoelectric characterization techniques. X-ray diffraction and transmission electron microscopy results obtained from my co-authors found that a perfect 0° tilt can be obtained when the TiNiCu heat treatment occurs (ii) after AlN deposition; this is likely because AlN was deposited onto an amorphous TiNiCu film with a low surface roughness. However, annealing the SMA/ piezoelectric composite was found to promote interdiffusion at the SMA (TiNiCu) / adhesion layer (Ta) / bottom electrode (Pt) interfaces. This resulted in an open polarization loop, which correspondingly would result in a loss of sensitivity in a magnetoelectric sensor. Therefore,

it was found from this work that AlN should be deposited (i) after TiNiCu crystallization to obtain high sensitivity for magnetoelectric sensor applications. I also performed analytical calculations to demonstrate how the thermal-induced phase transformation in the SMA layer can be used to tune the mechanical resonance frequency of the sensor.

2. **Curtis, S.M.,** Sielenkämper, M., Arivanandhan, G., Dengiz, D., Li, Z., Jetter, J., Hanke, L., Bumke, L., Quandt, E., Wulfinghoff, S. and Kohl, M., (2022). TiNiHf/SiO_2/Si shape memory film composites for bi-directional micro actuation. *International Journal of Smart and Nano Materials, 13*(2) pp.293-314. https://doi.org/10.1080/19475411.2022.2071352

The work reported in this manuscript was the culmination of a three-year-long research collaboration that was contributed to equally by Ph.D. students S.M. Curtis, M. Sielenkämper, and G. Arivanandhan. This research project was a part of the Deutsche Forschungsgemeinschaft (DFG) Special Priority Program (SPP 2206 - Cooperative Multistage Multistable Microactuator Systems). As the leader of the "Materials Development" team, my primary focus in this project was to research the functional properties of sputtered TiNiHf SMA films. The thermal transformation temperatures and thermal hysteresis of sputter-deposited TiNiHf films must satisfy the requirements of bistable actuators established by previous works on PMMA/TiNiHf/Mo/PMMA composites [22–26]. The primary requirement to develop a bi-stable actuator is that the glass transition temperature of the PMMA (T_g = 105 °C) polymer must fall within the thermal hysteresis of the TiNiHf SMA.

The results reported in this peer-reviewed manuscript presented experimental and computational simulation results on the research and development of bi-directional and bi-stable nano and microactuators based on the SMA material TiNiHf. Magnetron sputtered $Ti_{40.4}Ni_{48}Hf_{11.6}$ SMA films were deposited onto Si and SiO_2/Si substrates. Our characterization results revealed

that reducing TiNiHf film thickness from micro-scale down to nano-scale results in a reduction in transformation temperatures of the SMA. Despite the reduction in transformation temperatures, we showed that TiNiHf films as low as 220 nm can still display high-temperature actuation above 105°C (i.e austenite finish temperature, A_f > 105 °C) when deposited on SiO_2/Si substrates. In addition to high transformation temperatures, TiNiHf thin films also have a wide thermal hysteresis (ΔT > 50 °C). In this manuscript, we demonstrated how these favorable material properties of TiNiHf thin-films can be used to develop micro and nano-bistable actuators based on trimorph PMMA/TiNiHf/Si composites, whereby the PMMA undergoes a glass transition temperature at (T_g = 105 °C).

3. **Curtis, S.M.,** Gugat, J.L., Bumke, L., Dengiz, D., Seigner, L., Schmadel, D., Lazarus, N.S., and Quandt, E.. "Thin-Film Superelastic Alloys for Stretchable Electronics" (2023) *Shape Memory and Superelasticity*, pp. 1–15 *Invited Feature Paper* https://doi.org/10.1007/s40830-023-00422-4

The results presented in this peer-reviewed, co-authored manuscript represent the first experimental and numerical results of sputtered freestanding thin-film SMAs for stretchable devices. Copper is currently the most widely used thin-film metal for stretchable interconnects in the field of stretchable electronics. My co-author performed finite element analysis (FEA) simulations which predicted that ultra-low fatigue SMA TiNiCuCo structured into a serpentine structure can reach elastic strains 5X-7X larger than copper serpentines. I confirmed the FEA results by fabricating freestanding $T_{i53.3}Ni_{30.9}Cu_{12.9}Co_{2.8}$ thin-film serpentines with various thickness-to-width aspect ratios and characterizing the thermo-mechanical performance with tensile testing and infrared thermography imaging. Freestanding ultra-low fatigue TiNiCuCo superelastic serpentine interconnects were fabricated using the fabrication process established by

Lima de Miranda to fabricate functionalized freestanding NiTi films for medical devices like stents.

Our experimental results showed that the electrical resistivity of thin-film TiNiCuCo (5.43×10^{-7} Ωm) is higher than that of copper (1.87×10^{-8} Ωm). I demonstrated that the advantageous mechanical properties of superelastic materials can be combined with the excellent electronic properties of copper thin-films. Freestanding TiNiCuCo serpentines were coated in copper thin-films and were demonstrated to serve as functional stretchable electrical interconnects between two LEDs. Since the fabrication process developed by *Lima de Miranda* is based on a photolithography technique, it allows the development of freestanding patterned SMAs with feature sizes as low as 10 μm. Essentially the freestanding SMA can be micro-structured into any stretchable geometry using this fabrication procedure. This allows for the development of more complex stretchable geometries including fractal serpentines, archimedean spirals, and stretchable auxetic structures. Overall, our results only evaluate one alloy of TiNiCuCo, but I believe these results represent a significant breakthrough for the integration of any sputtered shape memory alloy thin films for use in stretchable MEMS devices as interconnects and electrodes.

4. **S.M. Curtis,** D. Dengiz, L. Bumke, and E. Quandt, (2022, May). "Auxetic Superelastic TiNiCuCo Sputtered Thin-Films For Stretchable Electronics." *In SMST2022* (pp. 11-13). ASM International. https://doi.org/10.31399/asm.cp.smst2022p0011

In this conference proceedings extended abstract, for the first time, I introduced two novel stretchable auxetic geometries called "rotating serpentine rectangle" and "rotating archimedean rectangle" auxetic structures. I used the same freestanding fabrication process described above to fabricate freestanding TiNiCuCo SMAs into these novel stretchable auxetic geometries. I characterize the mechanical properties of the structures to show their superelastic, stretchable, and

auxetic responses. The novel structures I introduced display enhanced stretchability and compressibility compared to traditional rotating polygon auxetic structures [27]. I also demonstrated that the 2D stretchable auxetic films can be shape-set to remember complex 3D macroscopic shapes like spheres and cylinders by annealing the SMA. These properties would be advantageous to integrate freestanding stretchable auxetic SMAs into applications that require crimping and deployment (e.g., aerospace solar cell deployment systems and implantable medical devices). In the "Summary and Outlook" Chapter of my thesis, I propose additional uses for these novel freestanding SMA stretchable auxetic structures as electrodes as well as substrates for wearable power electronics (e.g., energy harvester devices based on SMA/piezoelectric composites).

1.3 Ph.D. Thesis Chapter Organization:

This thesis is organized into eight chapters. Chapter 1 states the Ph.D. thesis motivation, research contributions, and thesis organization. Chapter 2 gives an introduction to the sputtered shape memory and superelastic materials NiTi, TiNiCu, TiNiCuCo, and TiNiHf and their implementation into MEMS applications. Additionally, a brief background on traditional stretchable electronics and auxetic meta-mechanical materials are given. Chapter 3 characterizes the performance of AlN/TiNiCu/Si/FeCoSiB composites for the development of magnetoelectric sensors with a tunable resonance frequency. A fabrication process is presented as well as analytical calculations to demonstrate how the phase change in the SMA can drive a resonance frequency change in magnetoelectric sensors. Chapter 4 investigates TiNiHf/Si and TiNiHf/SiO_2/Si bimorph composites for use as bi-directional and bistable microactuators through experimental methods and computation simulations. The influence of substrate, TiNiHf film thickness, and TiNiHf deposition parameters on thermal transformation properties was determined in this study. Chapter 5 presents the first results of superelastic TiNiCuCo freestanding films for stretchable electronics and demonstrates the advantages they offer over state-of-the-art copper thin-films. Chapter 6 expands on a conference proceeding paper that presents freestanding superelastic films in stretchable auxetic geometries for wearable electronics and implantable medical devices. Chapter 7 gives a summary and outlook of the major works in the thesis. Finally, Chapter 8 lists the research contributions of this work to the greater academic community.

Chapter 2. Introduction to Thin-Film Shape Memory Alloys (SMAs) for MEMS Devices

2.1 NiTi-based SMAs

2.1.1 Shape Memory Effect and Superelastic Effect

Shape memory alloys (SMAs) are smart materials with a plethora of advantageous material properties including a large work density, large energy density, and high strength-to-weight ratio. These properties arise from a reversible solid-to-solid phase transformation that can be thermal-induced (*shape memory effect*) or stress-induced (*superelastic effect*). In NiTi-based shape memory alloys, a structural phase transformation occurs between monoclinic martensite (B19') and cubic austenite (B2) [28]. Through a twinning/ detwinning process, the softer martensite phase can be deformed to extremely large strains of up to 8% [3]. The strains can be entirely recovered by heating the SMA above its austenite finish (A_f) temperature through the *shape memory effect*. This process can be purely thermally induced by heating above the A_f temperature to recover its original shape, and cooling below the martensite finish (M_f) temperature to remember that shape at room temperature. The temperature of the forward transformation is different than that of the reverse transformation, leading to thermal hysteresis. Since the phase transformation is reversible, the NiTi SMAs can undergo deformation and shape recovery by heating and cooling the SMA, as depicted in the "Shape Memory" image in **Figure 2.1** [2]**.**

The *superelastic effect* arises when strain-loading SMA materials at a temperature above A_f. Upon application of an applied stress/ strain, the SMA can reach superelastic strains as large as 10% by transforming from austenite to stress-induced martensite [29]. Upon removal of the applied load, the SMA can recover the strain and transform it back into the austenite phase. The

path taken during strain loading and unloading is different, leading to a stress-hysteresis, as shown in the "Superelastic" image in **Figure 2.1** [2]. Both stress-induced and temperature-induced phase transformations can be detected in SMA thin-films using micro-mechanical testing methods [30]. The elastic strains achieved by SMAs are extremely large compared to conventional metals like copper (Cu) which are known to undergo *ordinary plastic deformation* when subjected to strains ~0.3% [31] (also depicted in **Figure 2.1** [2].

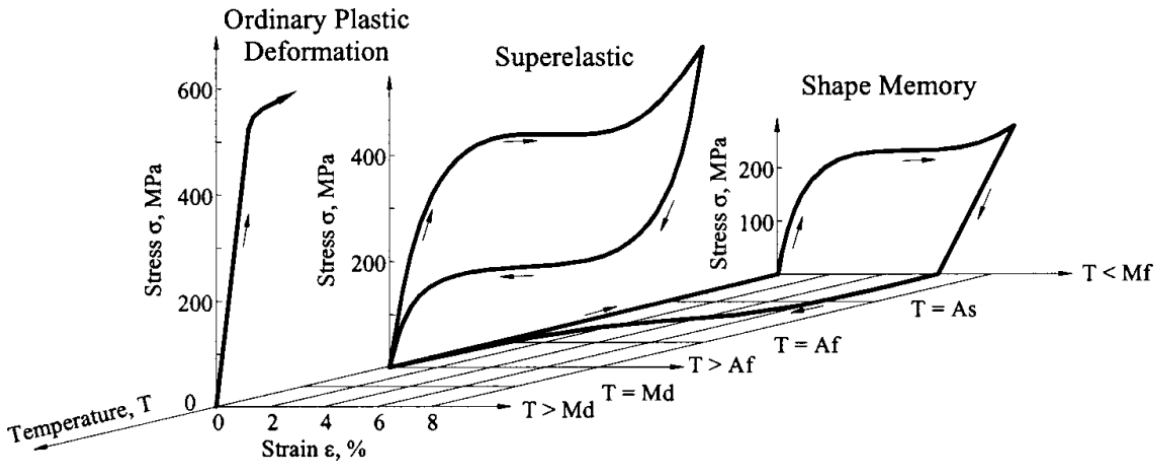

Figure 2.1: Stress-strain behavior of traditional metals (ordinary plastic deformation) and shape memory alloys displaying the superelastic effect ($T_{test} > A_f$), and shape memory effect ($T_{test} < A_s$). *Reproduced with permission from ref [2].*

2.2 Ultra-Low Fatigue TiNiCu and TiNiCuCo SMAs

SMA thin-films intended to be integrated into MEMS systems require a stable stress-induced or thermal-induced phase transformation for a high number of cycles [32]. The stability of the thermal and stress-induced phase transformation is dependent on the structural and functional fatigue properties of the material which are controlled by the microstructure of the SMA material [14]. The shape memory properties (transformation stress, transformation strain, transformation temperatures, and thermal hysteresis) are also influenced by the material's

microstructural characteristics [33]. In most cases, the microstructure properties (i.e., precipitate formation and homogeneity, and grain size) are controlled by the atomic composition of the SMA, and the heat treatment used to crystallize the SMA. Precise control over the film's microstructure can be obtained by optimizing the annealing heat treatment parameters (e.g., time, temperature, aging). The phase transformation properties (e.g. transition temperatures, enthalpy of transformation, critical stresses, and transformation strains) of SMAs can also be tuned by changing the NiTi atomic composition, or by alloying NiTi with other elements including Cu, Pd, Pt, Co, and Hf [34].

Adding Cu to the NiTi matrix (i.e TiNiCu) results in SMAs with moderate transformation temperatures (A_f > 60 °C) with extremely stable transformation properties and a complementary narrow thermal hysteresis (ΔT < 20 °C). Adding cobalt (Co) as a fourth element to the TiNiCu matrix (i.e TiNiCuCo) maintains a narrow thermal hysteresis, increases the brittleness of the SMAs film, and reduces the transformation temperatures below room temperatures (A_f < 15 °C). The reduction of thermal hysteresis width in TiNiCu and TiNiCuCo SMAs lead to lower recoverable superelastic transformation strains of 1.5% - 2% [35], compared to superelastic strains of 8% - 10% reported for binary NiTi.

The research group of Prof. Eckhard Quandt in Kiel Germany has shown that certain compositions of sputtered Ti-rich TiNiCu and TiNiCuCo (e.g., $Ti_{54}Ni_{34}Cu_{12}$ and $Ti_{54.7}Ni_{30.7}Cu_{12.3}Co_{2.3}$) are ultra-low fatigue SMAs when subjected to the right annealing parameters. These SMAs show a strong resilience to fatigue and were demonstrated to undergo the superelastic phase transformation reversibly for over 10 million cycles [18, 35, 36]. The reason for the improvement in fatigue is due to 1) reduction of oxides and carbides within NiTi matrix due to sputtering deposition, 2) control over microstructure during annealing leading to the

formation of homogeneously distributed nano-sized precipitates and nanoscale grain size, and 3) improvement in strain compatibility between the austenite and martensite phases [35]. The improvement in strain compatibility is also reflected by a narrow thermal hysteresis in SMA films [35].

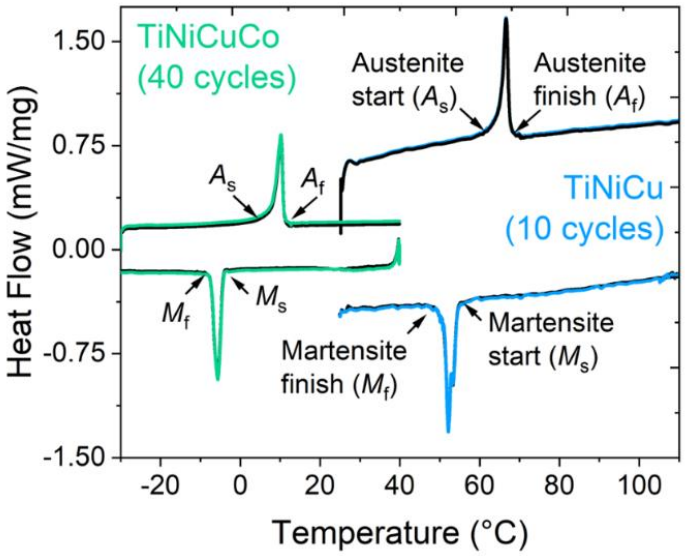

Figure 2.2: DSC result showing perfect thermal reversibility for 40 cycles in a TiNiCuCo thin-film and 10 cycles for a TiNiCu thin-film. Arrows indicate the austenite start/ finish temperatures (A_s, A_f), and martensite start/ finish temperatures (M_s, M_f).

Differential scanning calorimetry (DSC) is the primary method used during my Ph.D. to determine the transformation temperatures (e.g., austenite start/finish (A_s, A_f) and martensite start/finish (M_s, M_f) temperatures and thermal hysteresis width (ΔT)), and thermal reversibility of freestanding SMA films. **Figure 2.2** demonstrates exemplary DSC curves showing perfect thermal reversibility for 40 cycles for a TiNiCuCo thin-film, and for 10 cycles for a TiNiCu thin-film. There was a change in the transformation temperatures of less than 0.1 °C after 40 cycles for the TiNiCuCo alloy which indicates it has the prerequisite microstructure to be an ultra-low fatigue SMA [33]. Excellent thermal reversibility and a narrow thermal hysteresis were obtained for

almost all fabricated TiNiCuCo and TiNiCu films studied in this thesis, regardless of variations in composition, film thickness, or applied annealing conditions. While the transformation strains of TiNiCu and TiNiCuCo might be low compared to binary NiTi, both TiNiCu and TiNiCuCo SMAs are desirable for integration into MEMS devices because these SMA thin-films are extremely resistant to both structural and functional fatigue.

2.3 High-Temperature TiNiHf SMAs

Binary NiTi SMA films are typically limited by a maximum A_f < 100 °C. The phase transformation temperatures of NiTi can be increased dramatically by adding small amounts of Hf into the NiTi matrix [8]. TiNiHf is a high-temperature SMA (A_s > 100 °C) and in bulk form has many promising applications as high-temperature actuators in various aerospace and automotive applications. TiNiHf is desired for actuator applications due to its high actuation densities and large strength-to-weight ratios [37]. However, the stability against structural and functional fatigue is known to be poor in TiNiHf alloys due to their wide thermal hysteresis (ΔT > 50 °C). The wide thermal hysteresis reflects strain incompatibility at the austenite and martensite interface which can lead to the formation of dislocations and microcracks which are irreversible effects that are responsible for fatigue [38, 39].

Precisely controlling the shape memory properties of TiNiHf sputtered thin-films is essential in the development of bi-directional actuators with TiNiHf/Si bimorph composites and bistable actuators with PMMA/TiNiHf/Si trimorph composites [20]. As described in Chapter 4, TiNiHf/Si bimorph actuators can become bistable if they are combined with a polymer with a T_g

that falls within the thermal hysteresis of the TiNiHf ($M_s < T_g < A_s$) [23]. PMMA is selected as the polymer in the trimorph layer composite with TiNiHf SMA films as it is a standard resist material in various nano and micro-scale E-beam and X-ray lithography techniques and has a high glass transition temperature (T_g = 105 °C). The results presented on TiNiHf in this thesis are the findings of the "Materials Development" team in the DFG project SPP 2206. The aim of our team was to determine compositions of sputtered TiNiHf thin-films that can meet the requirements of bi-stable trimorph actuators using PMMA as the polymer layer.

Ni-rich TiNiHf alloys (Ni>50 at. %) are claimed to have better thermal cycling behavior than Ni-lean alloys. This is due to the formation of H-phase precipitates, which form after aging the Ni-rich alloy for several hours [40]. Ni-lean TiNiHf alloys (Ni < 50 at.%) are claimed to have lower transformation strains [41], unstable transformation temperatures with thermal cycling [39], and a low strength against dislocation plasticity [42]. Most experiments conducted on TiNiHf in the literature focus on bulk material [43–46]. Even though Ni-lean TiNiHf alloys are claimed to have poor functional stability, *Bechtold et. al* showed that 20 μm – 25 μm thick Ni-lean $Ni_{49.2}Ti_{31.4}Hf_{19.3}$ freestanding films can undergo the phase transformation for 1.5 x 10^6 cycles [15].

Even though the fatigue properties are claimed to be better in Ni-rich TiNiHf SMAs, our results were unsuccessful with thin-film Ni-rich TiNiHf compositions. Regardless of film composition or annealing treatment, all fabricated and characterized Ni-rich films were found to be in the austenite phase at room temperature. This is because Ni-rich (Ni > 50 at.%) TiNiHf film transformation temperatures are known to drop by 250 °C per 1 at.% of Ni. [47]. In agreement with the literature, our results on fabricated freestanding Ni-rich $Ti_{36.9}Ni_{50.1}Hf_{13}$ films showed no phase transformation between -100°C and 250 °C. For these reasons, Ni-rich SMAs were no longer

pursued in the development of bi-directional actuators based on TiNiHf/Si bimorph composites. Our research results suggested Ni-lean TiNiHf films are more suitable candidates as the SMA for TiNiHf/Si bimorphs as they can be heat treated at moderate temperatures for a short amount of time to produce a TiNiHf film that is in the martensite phase at room temperature. All fabricated freestanding TiNiHf films and bimorph TiNiHf/Si composites with a Ni content below 49.8 at.% displayed a high-temperature phase transformation temperature with A_f > 105 °C, which would be suitable for bi-directional and bi-stable actuation with TiNiHf/Si bimorph composites [6, 20].

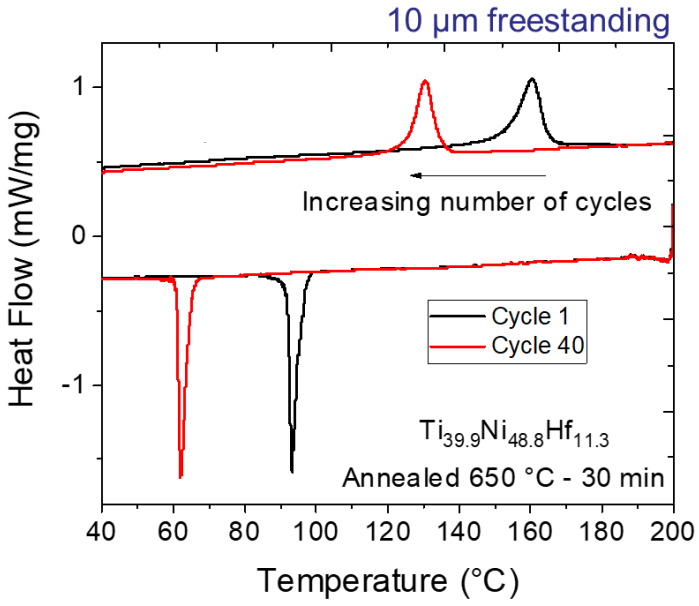

Figure 2.3: Demonstration of typical functional fatigue behavior with thermal cycling obtained in Ni-lean TiNiHf films. A 10 µm thick $Ti_{39.9}Ni_{48.8}Hf_{11.3}$ film annealed at 650 °C – 30 minutes showed a decrease in all martensitic phase transformation temperatures after 40 cycles.

2.3.1 Influence of Composition and Annealing on Thin-Film TiNiHf SMAs

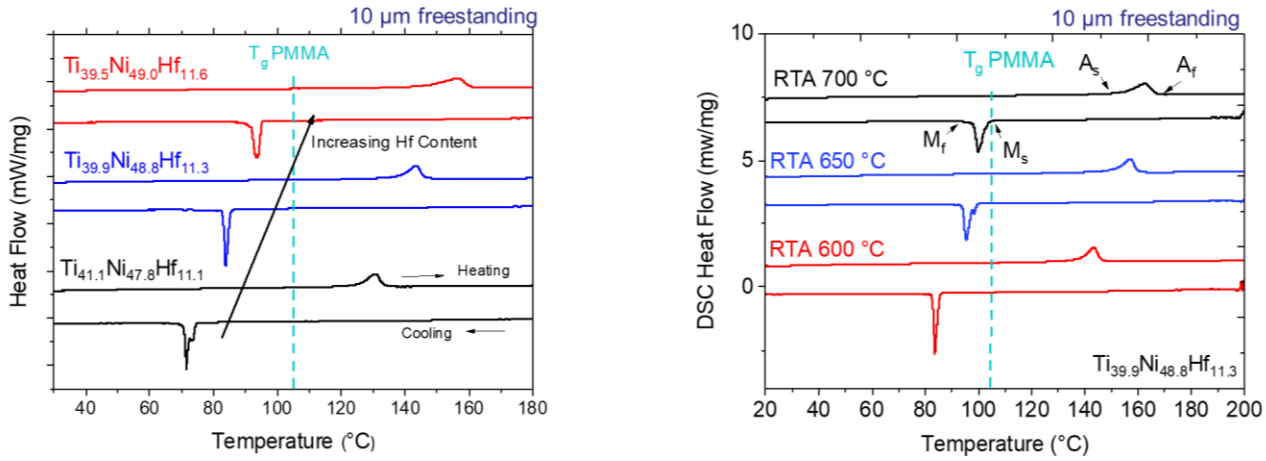

Figure 2.4: Differential scanning calorimetry scans showing the influence of a) atomic composition and b) RTA annealing temperature on the transformation properties of 10 µm thick Ni-lean TiNiHf films.

The influence of composition on the phase transformation properties of Ni-lean TiNiHf films was studied by adjusting the atomic composition between $Ti_{40.4}Ni_{48}Hf_{11.6}$ and $Ti_{41.4}Ni_{48.2}Hf_{10.4}$ using a multilayer sputter deposition approach with TiNiHf/Ti layers. Thermal fatigue was evaluated in fabricated freestanding TiNiHf films with decreasing film thickness from 21 µm to 2 µm. Several annealing conditions were tested with times ranging between 5 minutes and 60 minutes and temperatures ranging between 600 °C and 750 °C. The first DSC cycle of all tested freestanding Ni-lean TiNiHf films were found to have sufficient transformation temperatures to satisfy the requirements for the development of a bistable actuator with PMMA/TiNiHf/Si trimorph composites. However, all tested films displayed poor functional fatigue behavior with thermal cycling after 40 cycles (similar to the results shown in **Figure 2.3**) regardless of film composition or annealing conditions. This means after a certain amount of cycles, the TiNiHf film would no longer satisfy the requirements to achieve bistability with a PMMA/TiNiHf/Si trimorph composite.

Figure 2.4a) shows the influence of adjusting film composition on the transformation properties of 10 μm freestanding TiNiHf films, holding the annealing conditions constant. In general, slightly increasing the Hf at.% in TiNiHf films can result in a large increase in the phase transformation temperatures, an increase in the latent heat of transformation, and an increase in the thermal hysteresis width. However, the transformation temperatures, latent heat of transformation, and thermal hysteresis width of TiNiHf films can also be slightly increased by annealing the films at a higher temperature as shown in our previous work [6]. **Figure 2.4b)** demonstrates the influence of increasing the annealing temperature on the transformation temperatures of fabricated 10 μm thick $Ti_{39.9}Ni_{48.8}Hf_{11.3}$ films. Films were annealed at 600 °C, 650 °C, and 700 °C for 30 minutes each. In general, as the annealing temperature increases, the transformation temperatures also increase. It was also found in other experiments that longer annealing times typically result in larger transformation temperatures for TiNiHf films.

2.4 Sputtered SMAs for Sensors and Actuators

The reversible phase transformation between the monoclinic martensite phase and the cubic austenite phase in the SMA results in a reversible change between two different sets of material properties in the SMA. The different values between the martensite and austenite phases of NiTi SMA are given for a few mechanical, thermal, and electrical properties in **Table I.**

Table 2.1: Materials properties of the martensite and austenite phases of NiTi SMAs

	Young's Modulus [48]	Yield Strength [1]	Coefficient of Thermal Expansion [48]	Electrical Resistivity [1]
Martensite	28 GPa	150 MPa–300 MPa	6.6×10^{-6}	40–70 μΩ cm
Austenite	83 GPa	200 MPa–800 MPa	11×10^{-6}	70–110 μΩ cm

The difference in coefficient of thermal expansion (CTE) between the martensite and the austenite phase is one reason why they are implemented in actuator technologies [10]. When an SMA thin-film is sputtered onto a substrate structured into a cantilever geometry, a reversible bending effect occurs when thermally inducing the phase transformation in the SMA. This bending effect arises from the combined bimetallic effect of the SMA/substrate and the difference in CTE values that arise in the SMA during the phase transformation from martensite to austenite. Additionally, the phase transformation is associated with a change in the other mechanical properties of the SMA (i.e., Yield strength and Young's modulus).

The first work of my Ph.D. integrated an ultra-low fatigue TiNiCu SMA thin-film into a magnetoelectric sensor. Magnetoelectric sensors are a type of biomagnetic sensor based on mechanical coupling between a silicon substrate, piezoelectric thin-film layer, and magnetostrictive thin-film layer [49–51]. The mechanical resonance of the sensor is dependent on the mechanical properties (e.g., Young's modulus, density) of the mechanically coupled layers. The resonant frequency of a magnetoelectric sensor can be tuned by integrating a magnetoelectric sensor onto a bimorph SMA/Si composite. I was also able to show that the mechanical resonant frequency of the magnetoelectric sensor could be tuned by inducing the phase transformation within the SMA layer by heating/cooling the sensor device. I also showed in this work it was possible to develop high-performance AlN/TiNiCu/Si trimorph composites. The details of this work are given in Chapter 3 and in *Curtis et. al* [19].

The second work of my Ph.D. characterized the properties of freestanding TiNiHf films and micro and nanoscale thin-film TiNiHf SMAs when sputtered onto Si and SiO_2/Si substrates for bi-directional micro actuation applications. Investigations conducted during this thesis found the shape memory properties of magnetron-sputtered TiNiHf films were strongly influenced by

composition, the substrate, and film thickness. In general, the transformation temperatures of freestanding TiNiHf films were found to be slightly lower than bulk TiNiHf of similar atomic compositions. When TiNiHf thin-films are sputtered and annealed onto a substrate (e.g., Si or SiO_2/Si), it was found that there is a further reduction in transformation temperatures compared to freestanding films. There is a further reduction in transformation temperatures when the sputtered and annealed TiNiHf films are downscaled from micro to nanoscale film thicknesses. In this manuscript, we describe that there is a critical thickness limit for TiNiHf depending on the substrate used (e.g., Si or SiO_2/Si). The details of this work are given in Chapter 4 and in *Curtis et. al* [20].

2.5 The Need for SMAs in Stretchable Electronics

2.5.1 Traditional Stretchable Interconnects

The next generation of medical implants, wearable devices, and some aerospace components must be extremely lightweight while accommodating large levels of physical deformation. Electronics to be integrated on various body surfaces, e.g., blood veins, blood vessels, skin, heart valves, etc., must be able to withstand the extreme stretching, bending, and twisting deformations associated with the body's natural curvature changes. For example, electronic tattoos worn directly on the skin, e.g. skin sensors, and medical implants inserted inside the body should ideally conform to their environment to optimize device performance [52]. The research fields of flexible and stretchable electronics use microelectromechanical systems (MEMS) fabrication techniques to structure thin-film electronic components into new architectures that can withstand high levels of flexing, bending, and twisting deformations [53, 54]. Examples of bioelectronic applications that require stretchable electronic solutions are illustrated in **Figure 2.5** [55].

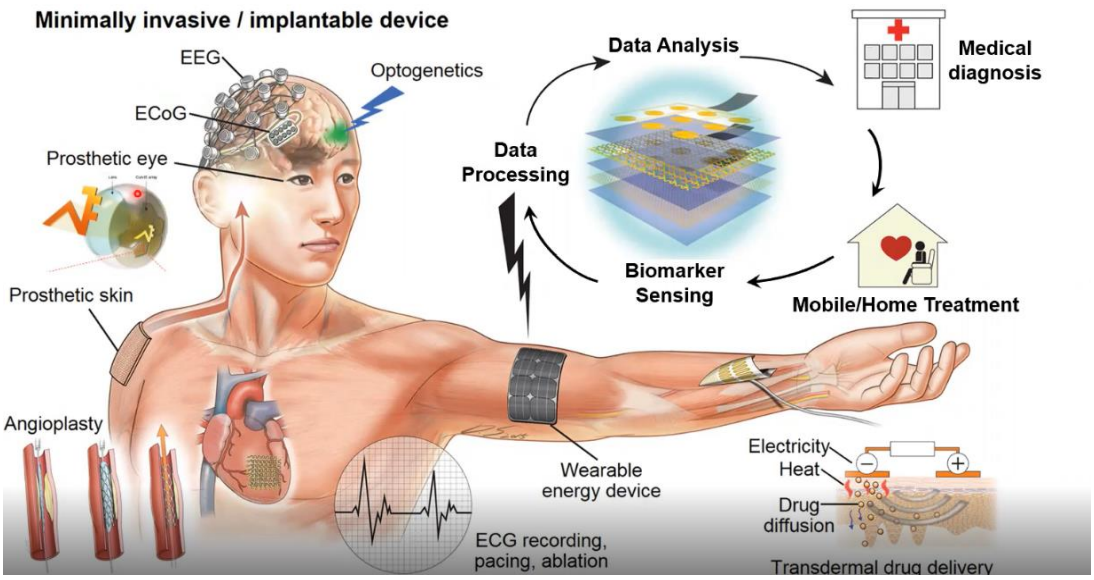

Figure 2.5: Various examples of state-of-the-art bio-integrated devices requiring co-integration of electronic components using stretchable electronic solutions. *Reproduced with permission from ref* [55].

The popular "island-bridge" method creates stretchable circuits by connecting small rigid functional device "islands" using wavy serpentine [56–59] or archimedean spiral [60, 61] interconnect "bridges". Under an applied force, the serpentine or archimedean interconnect will elongate and reconfigure its shape to accommodate the deformation of the stretchable circuit. In traditional "island-bridge" designs, essentially all strain is concentrated in the stretchable interconnect, and the islands undergo very little to no strain, which makes them suitable to house strain-sensitive MEMS electronics components. Large applied external strains in the archimedean spiral and serpentine interconnects arise from the non-uniform stress distribution along the regions of curvature in the stretchable interconnect [60–63].

Conductive serpentine interconnects based on thin-film metals like copper [64–66], and gold [56, 67] have countless applications as stretchable electrodes, antennas, and wires. The low intrinsic stresses provided by the serpentine structure allow even brittle semiconductor materials to become stretchable with examples including silicon [68–70] and gallium nitride [71–73]. Cu is

often the metal of choice for wires in stretchable circuits due to its excellent electronic conductivity and durability. Like most metals, Cu has a relatively low intrinsic elastic strain limit of ~0.3%, thus many demonstrated stretchable circuits suffer from plastic deformation at low-applied serpentine strains [31].

While thin-film shape memory alloys (SMAs) are known to have superior mechanical properties to traditional metals like copper, and similar electrical conductivities to liquid metals, SMAs have only been limitedly explored for use in stretchable devices [74]. The maximum reversible global strain reached by a serpentine or archimedean stretchable interconnect is ultimately limited by the intrinsic properties of the material (Young's modulus, Poisson's ratio, density) which determines the elastic strain limit of the material. I demonstrate in Chapters 5 and 6 that SMA thin-films patterned into stretchable interconnect geometries like serpentines and archimedean spirals can superelastically recover giant external strains of up to 150% and 454%, respectively. Chapter 5 presents both finite element analysis and experimental techniques which demonstrate the mechanical advantages superelastic TiNiCuCo serpentines offer over state-of-the-art copper serpentine for stretchable electronics.

2.5.2 Traditional Auxetic Metamechanical Materials

Auxetic mechanical metamaterials (also called just auxetic) are a class of man-made materials that display a negative Poisson ratio upon stretching/ compressing, due to the geometrical configuration of the material [75]. A unique feature of auxetic structures is that they display synclastic bending which allows 2D structures to conform around 3D curved surfaces. Other improved mechanical properties offered by auxetic structures in general include high impact resistance, reduced fatigue crack propagation, greater toughness and modulus strength, and

vibration damping [76]. Traditional "island-bridge" designs have a zero or positive Poisson's ratio upon stretching which leads to necking behavior and fracture of the stretchable device. Auxetic structures can distribute stress and strain more uniformly throughout the entire structure to overcome these necking issues.

Auxetic structures are commonly fabricated from polymer foams, and they are known to be highly adaptable structures to concave and convex surfaces due to the negative Poisson's ratio. To date, few studies have integrated auxetic structures into MEMS flexures and devices. *Bhullar et. al.* demonstrated 2D sheets of rotating square auxetic structures and re-entrant structures can be laser-welded into 3D cylindrical stent shapes to be used for medical devices [77, 78]. In 2019, *Jiang* pioneered the work to introduce auxetic meta-mechanical materials to the field of stretchable electronics [79]. *Jiang* demonstrated that the sensitivity of stretchable strain sensors is enhanced by attaching a thin-film to a 2D auxetic re-entrant PDMS frame. The PDMS elastomer only served as a stretchable substrate to support the active electrical materials [79]. The major drawback of classical auxetic structures (e.g. rotating polygons) is that the expandability and compressibility of the entire structure are limited by the stiffness of the connecting hinges (or pivot joints) of the structures [80, 81]. The stiffness of traditional auxetic structures may limit their practical use as implantable medical devices or other stretchable electronic applications, as volume expansion/compression requirements of implantable medical devices are met with traditional designs.

The superelastic and shape memory effects offered by SMAs are extremely beneficial to further improve the mechanical performance of auxetic meta-mechanical materials [82]. SMAs patterned into auxetic structures have been proposed for several applications including ballistics [83] and deployable antennas [84]. The process developed by *Lima de Miranda* [11, 12] is based

on photolithography and allows the fabrication of SMA freestanding thin-films films into any complicated design. In 2023, I co-authored a publication that investigated the auxetic behavior of NiTi SMAs patterned into traditional auxetic geometries [82]. In Chapter 6 of this thesis, I demonstrate two novel auxetic structures that display enhanced stretchability and compressibility. The structures are based on rotating polygon structures with rectangle islands, and with integrated stretchable serpentine and archimedean interconnect between the islands. I also show in this chapter the characterization results of the ultra-low fatigue SMA material, TiNiCuCo, patterned into these geometries. The combined effects of thin-film SMA materials patterned into geometries that display both stretchable and auxetic properties will be extremely useful for the development of next-generation implantable devices.

Chapter 3. Publication: Integration of AlN Piezoelectric Thin-Films on Ultra-Low Fatigue TiNiCu Shape Memory Alloys

Own contributions to the following article[1] ·

- analytical calculations (large fraction)
- sample fabrication (large fraction)
- shape memory alloy characterization (large fraction)
- piezoelectric characterization (moderate fraction)
- structural characterization (moderate fraction)
- microstructure characterization (small fraction)
- interpretation of the results (large fraction)
- writing of the manuscript (large fraction)

Reproduced from

Curtis, S.M., Wolff, N., Dengiz, D., Lewitz, H., Jetter, J., Bumke, L., Hayes, P., Yarar, E., Thormählen, L., Kienle, L. Meyners, D., and Quandt, E., (2020). Integration of AlN piezoelectric thin films on ultralow fatigue TiNiCu shape memory alloys. *Journal of Materials Research*, 35(10), pp.1298-1306. *Invited Feature Paper*

https://doi.org/10.1557/jmr.2020.106

[1] · this page is required by regulations

Motivation:

The Collaborative Research Centre (CRC 1261 – Magnetoelectric Sensors: From Composite Materials to Biomagnetic Diagnostics) in Kiel, Germany aims to research and develop different fabrication approaches for magnetoelectric sensors with high sensitivity at biomagnetic frequencies. In Kiel, the magnetoelectric sensors with the highest sensitivity are based on thin-film composites of a piezoelectric material (AlN), a magnetostrictive material (FeCoSiB), and a polycrystalline silicon substrate. Due to the mechanical coupling of all three material layers, there is one mechanical resonance frequency. The sensitivity and magnetoelectric voltage of a magnetoelectric sensor can be enhanced when driven at the mechanical resonance frequency.

When I joined the CRC 1261 in 2018, I was tasked to integrate a shape memory alloy (SMA) thin-film into the magnetoelectric sensor stack. As described in the manuscript below, the reversible thermal induced solid-to-solid phase transformation of the SMA TiNiCu can be used to tune the mechanical resonance frequency of the magnetoelectric sensor. As described in Chapter 2, the thin-film SMA TiNiCu was previously identified to be an ultra-low fatigue SMA, able to undergo phase transformations repeatedly for millions of cycles with essentially no change in the thermal or mechanical characteristics. In this co-authored manuscript, we show that the ultra-low fatigue properties of thin-film TiNiCu are advantageous for sensor applications that require a high life cycle. Furthermore, we demonstrate that the low surface roughness of crystallized TiNiCu films on silicon substrates allows the TiNiCu layer to serve as the substrate for other thin-film materials MEMS (e.g. AlN, Pt, Ta).

3.1 Abstract:

Biomagnetic field sensors based on AlN/ FeCoSiB magnetoelectric (ME) composites benefit from a resonant frequency that can be precisely tuned to match the biomagnetic signal of interest. A tunable mechanical resonant frequency is achieved when ME composites are integrated onto shape memory alloys (SMA) thin-films. Here, high-quality *c*-axis growth of AlN is obtained on (111) Pt seed layers on both amorphous and crystallized TiNiCu SMA thin-films on Si substrates. These composites show large piezoelectric coefficients as high as $d_{33,f}$ = 6.4 pm/V ± 0.2 pm/V. Annealing the AlN/ Pt/ Ta/ amorphous TiNiCu/ Si composites to 700 °C to crystallize TiNiCu promoted interdiffusion of Ti into the Ta/ Pt layers leading to an enhanced conductivity in AlN. Depositing AlN onto already crystalline TiNiCu films with low surface roughness resulted in the best piezoelectric films and hence is found to be a more desirable processing route for magnetoelectric composite applications.

3.2 Introduction

Thin-film magnetoelectric (ME) composites are attractive candidates for use in biomagnetic sensors, energy harvesters [85], highly efficient power converters, magnetometers, RF tunable inductors, and mechanical antennas [86–89]. Heterostructures with aluminum nitride (AlN) serving as the piezoelectric layer and amorphous iron-cobalt silicon boron (FeCoSiB) alloy as the magnetostrictive layer have demonstrated ME coefficients in a vacuum as large as 20 kV/cm Oe [49] with limits of detection as low as 1 $pT/\sqrt{Hz}$ [49, 50, 90]. The ME voltage and sensitivity can be enhanced by 1-2 orders of magnitude when driven at the mechanical resonant frequency [87, 91, 92]; therefore, many applications could benefit from a ME composite with a tunable resonant frequency. For example, deep brain stimulation (DBS) is a medical treatment

used on patients suffering from tremors or dystonia. In this treatment, an array of electrodes are implanted deep in the patient's brain and stimulated at a well-defined frequency between 130 Hz - 170 Hz [93]. For localization of the stimulated area near the electrode, it would be necessary to precisely tune the mechanical resonant frequency of a ME sensor to match the stimulation frequency of the electrode, or one of its multiples [93–95].

Nickel-titanium (NiTi) shape memory alloys (SMA) can reversibly undergo a diffusion-less solid-to-solid phase transformation between the martensite phase (monoclinic), austenite phase (cubic), and R-phase (orthorhombic). The Young's modulus of the high-temperature austenite phase is usually larger than the low-temperature martensite phase [96]. To change the resonant frequency of a ME sensor, *Röbisch et al.* [97] proposed harnessing the reversible and gradual change in the Young's modulus of NiTi SMA substrates with the phase change in the SMA [97]. The entire 2.5 mm x 15 mm SMA/ ME composite (1 μm AlN / 2 μm FeCoSiB / 50 μm NiTi) was annealed at 450 °C for 30 minutes, to crystallize the NiTi layer. Progressive heating and cooling of this AlN/ FeCoSiB/ NiTi cantilever induced the reversible phase transformation in the SMA, resulting in a mechanical resonant frequency shift (Δf) of 12%. Below room temperature, at T = 20 °C, the SMA was in the martensite phase with $f_{martensite}$ = 332 Hz. Heating the SMA to T = 130 °C induced the phase transformation to the austenite phase with $f_{austenite}$ = 351 Hz. Finally, cooling the SMA to T = 64 °C induced another transition to the R-phase with a corresponding change in the resonant frequency to $f_{R\text{-}phase}$ = 312 Hz [97]. While varying the temperature was used to experimentally induce the phase transformation in this study, one could also control this transformation through the application of stress.

The martensitic transformation temperatures and fatigue stability of NiTi-based SMAs can be tuned for the desired application by alloying with elements such as Pt, Au, Cu, Hf, Co, and Pd

[18, 98–100]. In this manuscript, the alloy $Ti_{50}Ni_{35}Cu_{15}$ is investigated because previously it was identified as an ultra-low fatigue SMA material, able to undergo this phase transformation for millions of cycles, reversibly [18, 35]. The sputter deposition process we use results in thin-film amorphous SMAs, therefore, all samples must be crystallized at high temperatures (450 °C – 700 °C) to enable the martensitic phase transformation [101]. The annealing process has a significant impact on the surface morphology of crystalline TiNiCu films, where higher post-sputter annealing temperatures increase the surface roughness and grain size of TiNiCu [102]. The integration of high-quality AlN piezoelectric and TiNiCu SMA thin-films is the key task for the future development of a ME sensor with a tuneable resonant frequency. The major aim of the presented work is to evaluate the influence of the annealing TiNiCu on the piezoelectric performance of AlN in fabricated AlN/ Pt/ Ta/ TiNiCu / Ta/ Si/ FeCoSiB composites.

3.3 Methods and Materials

3.3.1 Piezoelectric Characterization:

Double-beam laser interferometer, DBLI, measurements were performed on all samples in a parallel plate capacitor geometry on an aixACCT Systems aixDBLI tool. Polarization and displacement curves were taken at a minimum of three spots on each sample to generate an average $d_{33,f}$ at each applied voltage (i.e 10V, 20V, 50V, and 100V). The slope of the displacement curves at each applied voltage is used to obtain $d_{33,f}$.

3.3.2 Structural Characterization:

AFM measurements were obtained on an AIST-NP SPM 1000 instrument in non-contact tapping mode and were conducted using a 160 µm long arrow-head tip [NanoWorld Arrow NC]. XRD (SmartLab 9 kW, Rigaku) ω rocking curve measurements were performed in a ω range

+/- 10° around the (002) AlN peak (2θ = ~36°) with a step size of 0.02° and a scan speed of 1° per min.

3.3.3 Microstructural Characterization:

The samples were investigated using Transmission Electron Microscopy operated in scanning (STEM) mode on a Tecnai F30 G² Twin instrument equipped with a Si/Li- drift detector (EDAX system) for energy-dispersive X-ray spectroscopy (EDS) analysis. The samples have been prepared to electron transparency by the focused ion beam (FIB) method using Ga-ions and Pt protection layers during the thinning procedure.

3.4 Results and Discussion:

3.4.1 Analytical Calculation of Resonant Frequency:

Mechanical resonant frequencies are well-studied for cantilever systems composed of a substrate and a thin-film [97, 103, 104]. The theory and Matlab code presented by *Zannon et al*. [103] are adapted here to calculate the resonant frequency of a freestanding cantilever beam composed of three mechanically coupled thin-film layers (ME/ NiTi/ Si). The thick Si and NiTi substrates will dominate the elastic properties of the vibration, therefore the contributions of the adhesion and electrode layers are neglected. The magnetoelectric mechanical properties (E_{ME} and ρ_{ME}) are estimated in Equations A1 and A2 (Appendix, Section 3.6.1) using the thickness weighted average of the piezoelectric (2 μm AlN) and magnetostrictive (2 μm FeCoSiB) functional layers. Adding additional thin-film materials layers to the composite will shift the center of mass (y_{cm}) and inertia (I_x) of the beam layers which can be calculated for using Equations A3 – A6 (Appendix, Section 3.6.1). Equation 1 shows the resonant frequency is dependent on the geometrical dimensions of the cantilever: width (w), length (L), and thickness (t_x), as well as Young's modulus

(E_x), density (ρ_x), the moment of inertia (I_x), and in-plane surface area (A_x) of each material layer (x = ME, NiTi, Si). λ is an integration constant determined by the boundary conditions for the first bending mode of a cantilever beam (λ = 1.875) [92].

$$f_r = \frac{1}{2\pi} * \frac{\lambda^2}{L^2} * \sqrt{\frac{(E_{ME}I_{ME})+(E_{NiTi}I_{NiTi})+(E_{Si}I_{Si})}{(\rho_{ME}A_{ME})+(\rho_{NiTi}A_{NiTi})+(\rho_{Si}A_{Si})}} \quad \text{(Equation 1)}$$

The largest Young's modulus difference for NiTi occurs between the martensite phase ($E_{Martensite}$ = 28 - 41 GPa) and austenite phase ($E_{Austenite}$ = 41 - 83 GPa) [105]. Therefore, the maximum Δf will occur when there is a full transformation from martensite to austenite as shown in Equation 2.

$$\Delta f = ((f_{austenite} - f_{martensite})/ f_{austenite}) \times 100 \quad \text{(Equation 2)}$$

The analytical calculations presented in this manuscript use the standard literature values of sputtered thin-film binary NiTi [96] to generalize the resonant frequency calculation for other shape memory alloys (i.e TiNiCu, TiNiCuCo, NiTiPd, NiTiPt) since the mechanical properties of thin-film NiTi [101, 105] are similar to TiNiCu. A summary of all materials properties used in the following calculations and experiments are shown in **Table 3.1.**

Table 3.1: Mechanical properties ME/SMA/Si composite used in analytical calculations

Material	NiTi [96]	TiNiCu [102]	(100) Silicon [106]	(002) AlN [97]	FeCoSiB [97]	ME Layer
Thickness	Varied: 1 – 80 μm	Not used in calculation	Varied: 0, 100, 350 μm	2 μm	2 μm	4 μm
Young's Modulus	E_{Mart}: 41 GPa E_{Aust}: 83 GPa	E_{Aus}: 78 GPa	169 GPa	310 GPa	150 GPa	230 GPa
Density	6450 kg/m^3	6500 kg/m^3	2330 kg/m^3	3300 kg/m^3	7250 kg/m^3	5275 kg/m^3

ME sensors fabricated onto smooth Si and polycrystalline Si substrates are known to have large mechanical quality factors [107]. The mechanical resonant frequency of both the martensite and austenite phases are evaluated as a function of NiTi thickness on 350 μm and 100 μm thick Si substrates in **Figures 3.1(a)** and **3.1(b)**, respectively. As the NiTi thicknesses increase, Δf also increases, due to a larger volume of material undergoing the phase transformation. However, due to the thick Si layers, only a small shift is theoretically achievable ($\Delta f_{Si=350\mu m}$ = 0.1% - 2%) and ($\Delta f_{Si=100\mu m}$ = 0.3% – 5.4%). As shown in **Figure 3.1(c)**, when the Si substrate is eliminated, Δf can be significantly enhanced ($\Delta f_{freestanding}$ = 7.6% to 28.3%). Without the Si substrate present, one must consider if the neutral plane (y_{cm}, Equation A3) were to lie within the AlN layer in the ME stack, the sensor could lose its sensitivity due to a balance in compressive and tensile stresses causing a loss of polarization of AlN [108]. This would likely prevent the magnetoelectric effect and must be considered when ME composites are fabricated onto freestanding SMA substrates.

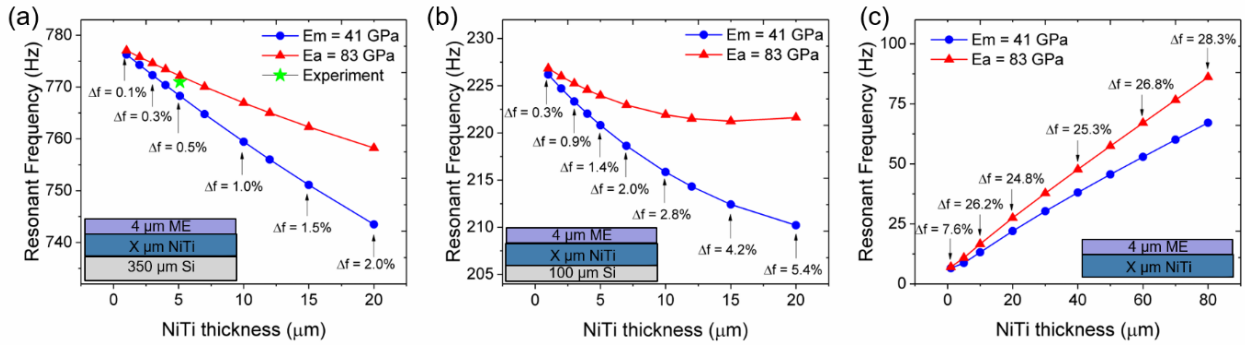

Figure 3.1: Analytical calculation demonstrating resonant frequency dependence on NiTi thickness on (a) 350 μm, (b) 100 μm, and (c) 0 μm thick Si substrates. The largest shift in resonant frequency (Δf) occurs when there is a full phase transformation from martensite ($E_m = E_{martensite}$ = 41 GPa) to austenite ($E_a = E_{austenite}$ = 83 GPa).

The validity of the analytical calculations was checked by obtaining an experimental resonant frequency measurement on a fabricated (2 μm AlN / 5.1 μm TiNiCu / 350 μm Si / 2 μm FeCoSiB) ME composite at room temperature. Analytical calculations predicted a resonant

frequency of 768 Hz in the martensite phase and 772 Hz in the austenite phase for a 2.5 mm x 25 mm cantilever ME composite of similar thicknesses. The experimental resonant frequency ($f_{experiment}$ = 771 Hz) of the sensor at room temperature is in close agreement with the calculated resonant frequency, as indicated by the green star in **Figure 3.1(a)**. These results are further discussed in the Appendix (**Figure A3.1**, Section 3.6.1).

3.4.2 SMA ME Sensor Fabrication:

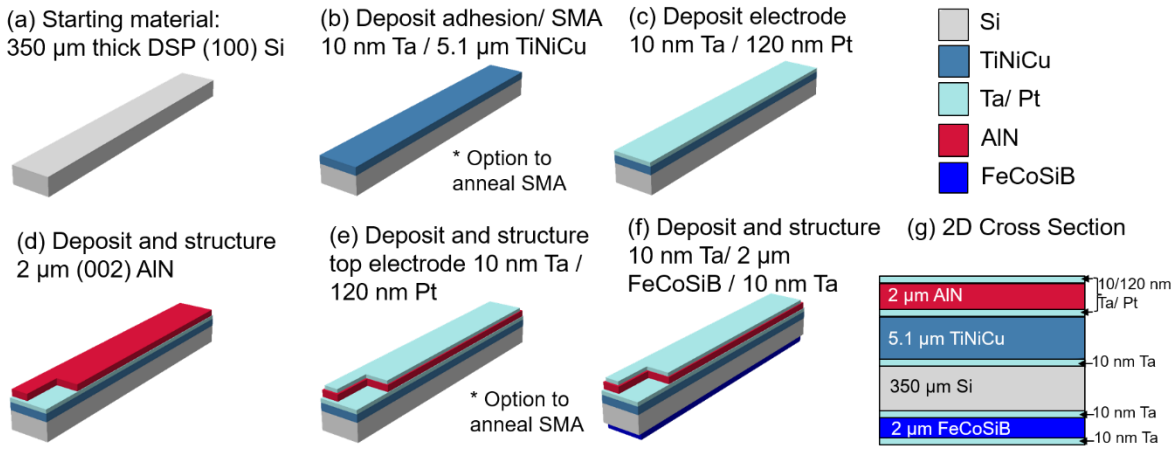

Figure 3.2: Process flow for SMA/ ME magnetoelectric composite fabrication
(a) Starting material 350 µm thick Si
(b) Sputter deposition of amorphous 5 µm thick TiNiCu*
(c) Deposit bottom electrode 120 nm (111) Pt
(d) Low-temperature pulsed DC reactive sputtering of piezoelectric layer 2 µm (002) AlN, structured via wet etching with H_3PO_4
(e) Deposit top electrode 120 nm (111) Pt, structured via ion beam etching*
(f) Deposit magnetostrictive layer 2 µm FeCoSiB, and structured via ion beam etching
**Rapid thermal anneal (RTA) heat treatment to crystallize the TiNiCu SMA can occur either before step (b) or after step (e)*

As depicted in **Figure 3.2**, Pt/Ta/AlN/Pt/Ta/TiNiCu/Ta/Si/Ta/FeCoSiB/Ta composites were deposited via magnetron sputtering (Von Ardenne CS 730S) and structured through a combination of photolithography (Karl Suss MA6), and wet and dry etching techniques. Starting with a 350 μm thick double side polished (100) Si wafer (**Figure 3.2(a)**), an adhesion layer (10 nm Ta) and amorphous SMA film (5.1 μm $Ti_{55}Ni_{30}Cu_{15}$) are deposited (**Figure 3.2(b)**). Next, the piezoelectric component is formed into a parallel plate capacitor configuration through deposition of the adhesion layer (10 nm Ta), the bottom electrode (120 nm (111) Pt) (**Figure 3.2(c)**), piezoelectric layer (2 μm AlN) (**Figure 3.2(d)**), another adhesion layer (10 nm Ta) and the top electrode (120 nm (111) Pt) (**Figure 3.2(e)**). A (111) Pt orientation for the bottom electrode is critical to promote *c*-axis (002) AlN texture during the low-temperature pulsed DC reactive sputtering process used here [109]. The top electrode and AlN layer are structured using ion beam etching (IBE- Oxford Instruments Ionfab 300 IBE), and a wet etchant (85 wt.% H_3PO_4, 80 °C) [109], respectively. Finally, the deposition of the amorphous phase magnetostrictive layer, sandwiched between an adhesion layer and protection layer (10 nm Ta/2 μm FeCoSiB/10 nm Ta), is executed via RF sputtering on the backside of the Si wafer and structured through photolithography and IBE as shown in **Figure 3.2(f)**. The annealing step required to crystallize the TiNiCu SMA must occur prior to magnetostrictive deposition since amorphous FeCoSiB is known to crystallize at temperatures above 300 °C [50, 110]. An advantage to putting FeCoSiB on the backside is the Si substrate is providing a smooth surface for the deposition of FeCoSiB because previously it was shown to significantly improve the soft magnetic properties [111, 112]. The specific sputter parameters (pressure, power, Ar flow, etc) of each material layer in the composite are given in the Appendix (**Table 3.3**, Section 3.6.2).

Polycrystalline sputtered AlN is able to withstand annealing temperatures of up to 1350 °C [113]. The workflow offers two possibilities: crystallization of TiNiCu at 700 °C for 15 minutes by rapid thermal annealing (RTA, CreaTec Fischer and Co. GmBh) (i) before or (ii) after deposition of AlN, as reflected in steps 2(b) and 2(e) in **Figure 3.2**. The annealing step is the most critical part of the process flow because it will set the SMA's microstructure which ultimately will determine the SMA's thermal and mechanical properties. Additionally, the annealing temperature will control the martensitic transformation temperatures of the SMA [101]. We only investigated an annealing temperature of 700 °C in this manuscript, however, temperatures between 450 °C – 800 °C would be suitable for most NiTi-based SMA materials.

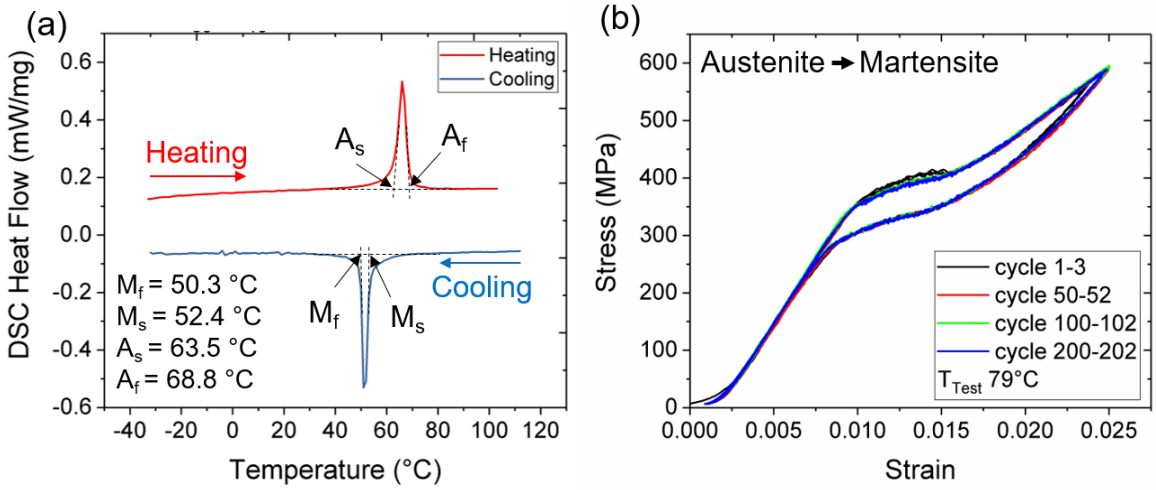

Figure 3.3: Shape memory alloy characterization of free-standing TiNiCu film annealed to 700°C for 15 minutes. (a) Differential scanning calorimetry curves show the austenite and martensite transformation temperatures of the sample. (b) An exemplary tensile testing plot of a TiNiCu dogbone reversibly stretching to a strain of 0.025 (2.5%), 200 times with no observable fatigue.

Figure 3.3(a) shows a differential scanning calorimetry (DSC Netzsch 204F1Phoenix) measurement of a 20 µm thick TiNiCu film after annealing at 700°C for 15 minutes. The austenite

and martensite transformation temperatures (i.e A_s = 63.5 °C, A_f = 68.8 °C, M_s = 52.4 °C, M_f = 50.3 °C) occur at moderate temperatures suitable for ME sensor operations. These transformation temperature measurements are in good agreement with temperature-dependent XRD measurements on the fabricated composites, discussed in the Appendix (**Figure A3.2,** Section 3.6.3). A tensile testing (Zwick Roell Z.05) plot of TiNiCu after annealing is shown in **Figure 3.3(b)**. When TiNiCu is pulled to an elongation of 2.5% (strain = 0.0025) for 200 cycles there was very little observed structural and functional fatigue demonstrated in the SMA's hysteresis loop. This is also in agreement with the literature where previously TiNiCu thin-films of similar composition were found to be ultra-low fatigue materials, reversibly undergoing the phase transformation 10^7 times with minimal functional fatigue demonstrated in the hysteresis loop [18].

3.4.3 Piezoelectric Characterization of (002) AlN:

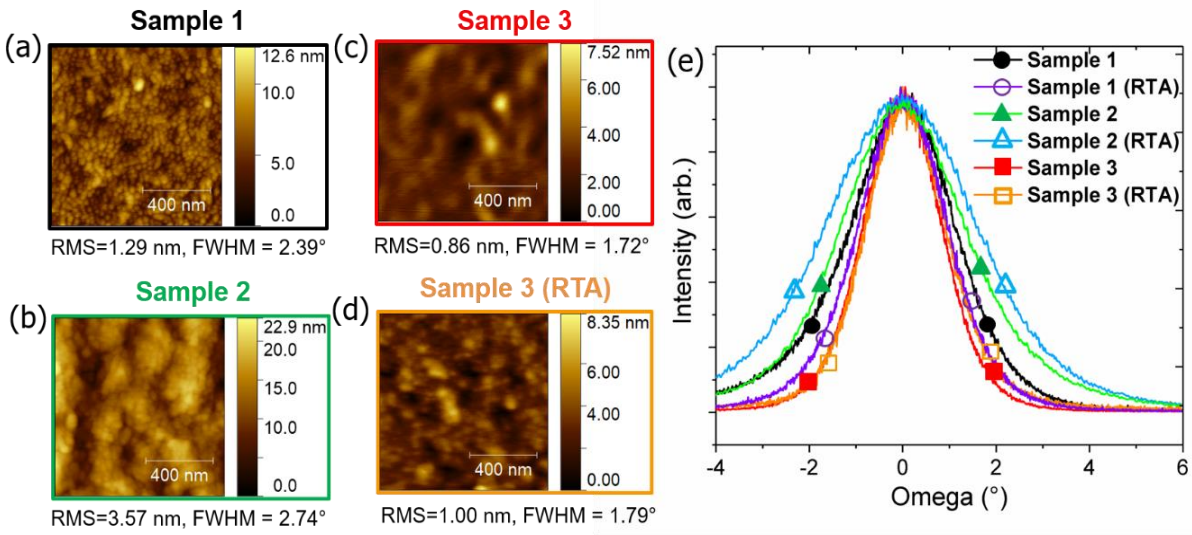

Figure 3.4: Structural characterization of (002) AlN grown onto various substrate types. AFM surface roughness measurements and X-ray diffraction curves. (a) Sample 1: (100) Si (reference sample) (black), (b) Sample 2: already crystalline TiNiCu (green), (c) Sample 3: amorphous TiNiCu (red), and (d) Sample 3 after annealing: amorphous TiNiCu then crystallized (orange). (e) X-ray diffraction rocking curve (ω scans) of the (002) AlN peak (2θ = ~36.7°) and FWHM for each sample shown in Figure (a) – (d).

C-axis (002) AlN polycrystalline thin-film growth is known to be highly dependent on the underlying substrate surface roughness [109, 114]. Variations in the structural and piezoelectric properties are evaluated for sputtered polycrystalline AlN onto (111) Pt seed layers on three substrates: Si (Sample 1), already crystalline TiNiCu on Si (Sample 2), and amorphous TiNiCu on Si (Sample 3). Sample 3 must be annealed after AlN deposition in order to crystallize the underlying TiNiCu film (Sample 3: annealed). To provide a complete comparison, Sample 1 and Sample 2 were also characterized after annealing the composites (i.e. Sample 1: annealed and Sample 2: annealed).

Nanoscale imaging of the surface topography (root mean squared – RMS) with atomic force microscopy (AFM) in tapping mode was conducted on at least three different locations on all samples. These surface roughness measurements were then correlated to the structural crystallinity of AlN, revealed by the full width at half maximum (FWHM) XRD rocking curve (ω scans) about the (002) AlN peak (2θ = ~36.7°). A narrow FWHM typically indicates a highly textured (002) AlN with columnar *c*-axis growth, thus better quality AlN film and higher $d_{33,f}$ [115]. **Figure 3.4(a)** shows a 1 μm x 1 μm AFM image of Sample 1: as-deposited (reference sample), (002) AlN on smooth Si substrate with a low surface roughness of RMS = 1.29 nm ± 0.39 nm and FWHM = 2.39°. **Figure 3.4(b)** shows AlN deposited onto already crystalline TiNiCu (Sample 2: as-deposited) has a larger surface roughness RMS = 3.57 nm ± 0.23 nm and larger FWHM = 2.74°. As shown in **Figure 3.4(c)**, the lowest surface roughness is obtained when AlN is deposited onto an amorphous TiNiCu film RMS = 0.86 nm ± 0.26 nm with the narrowest FWHM = 1.72° (Sample 3: as deposited). The AFM map in **Figure 3.4(d)** shows upon annealing the AlN/ amorphous TiNiCu/ Si composite to 700 °C (Sample 3: annealed), the surface roughness slightly increased from 0.86 nm ± 0.26 nm to

1.00 nm ± 0.14 nm which only corresponded to a slight increase in the FWHM from 1.72° to 1.79°. The rocking curve measurements used to calculate the FWHM value for all samples are shown in **Figure 3.4(e)**.

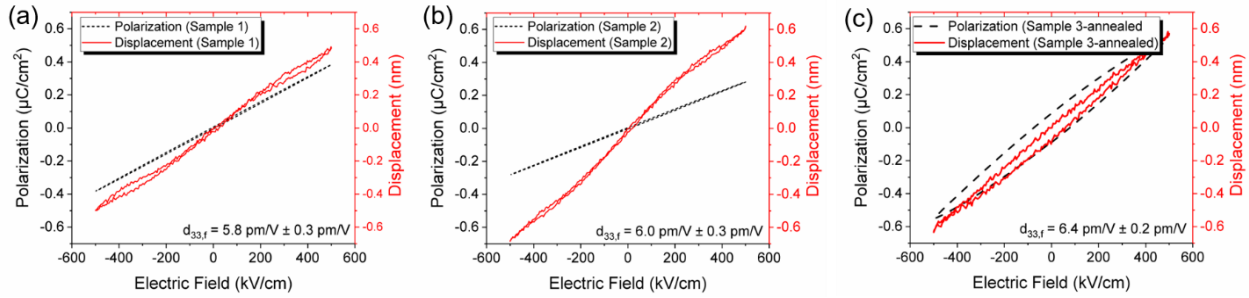

Figure 3.5: Polarization and displacement curves obtained from DBLI measurements with an applied electric field between ± 500 kV/cm for AlN on Si and TiNiCu substrates. (a) Sample 1: As-deposited, (b) Sample 2: As-deposited, and (c) Sample 3: Annealed.

The effective longitudinal piezoelectric coefficient ($d_{33,f}$ ± standard deviation) was determined through standard double beam laser interferometry (aixACCT Systems, aixDBLI) measurements [116, 117]. DBLI polarization and displacement curves were compared for Samples 1 – 2 in the as-deposited state and Sample 3 after annealing. Polarization measurements in **Figure 3.5(a)** demonstrate Sample 1 has an average $d_{33,f}$ coefficient of 5.8 pm/V ± 0.3 pm/V, on par with the state-of-the-art values reported for low-temperature sputtered AlN [109]. Sample 1 also displays typical linear polarization behavior with similar characteristics to AlN sputtered onto other electrodes (Ti, Pt, and Al) on Si substrates [114]. The $d_{33,f}$ value is found to be slightly improved when AlN is sputtered onto (111) Pt on both amorphous and crystalline TiNiCu thin-films on Si substrates. Despite the large surface roughness in Sample 2, the typical linear polarization behavior of AlN was observed in **Figure 3.5(b)**, with a high longitudinal piezoelectric coefficient $d_{33,f}$ = 6.0 pm/V ± 0.3 pm/V. A linear polarization loop and an even larger $d_{33,f}$ coefficient was obtained when AlN was deposited onto amorphous TiNiCu for Sample 3 as-

deposited ($d_{33,f}$ = 6.3 pm/V ± 0.2 pm/V). However, **Figure 3.5(c)** shows the annealing step results in an open polarization loop for Sample 3-annealed. This indicates the AlN layer in Sample 3-annealed has a higher conductivity and higher resistive losses than the other samples. A summary of all DBLI measurements is given in the Appendix (**Table 3.5**, Chapter 3.6.4). The $d_{33,f}$ and polarization curves of all samples in the as-deposited state and after annealing state are shown in the Appendix, (**Figure A3.3,** Chapter 3.6.4). These results prompted investigation of the interfaces to correlate microstructure changes to the electrical and structural properties of sputtered AlN. **Table 3.2** shows a summary of all investigated piezoelectric properties of each sample in both the as-deposited state, and after annealing at 700 °C for 15 minutes.

Table 3.2: Summary of investigated (002) AlN piezoelectric properties of samples as-deposited and after annealing at 700 °C for 15 minutes.

	Sample 1:		Sample 2:		Sample 3:	
Processing Difference:	AlN on Si Reference Sample		AlN on already crystalline TiNiCu		AlN on amorphous TiNiCu	
Device Cross Section:	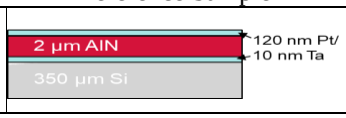				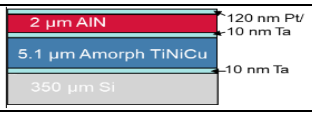	
Piezoelectric Property:	Sample 1: As-Deposited	Sample 1: Annealed	Sample 2: As-Deposited	Sample 2: Annealed	Sample 3: As-Deposited	Sample 3: Annealed
DBLI: $d_{33,f}$	5.8 pm/V ± 0.3 pm/V	5.9 pm/V ± 0.3 pm/V	6.0 pm/V ± 0.3 pm/V	6.4 pm/V ± 0.1 pm/V	6.3 pm/V ± 0.2 pm/V	6.4 pm/V ± 0.2 pm/V
XRD: FWHM	2.39 °	2.34 °	2.74 °	3.94 °	1.72 °	1.79 °
AFM: RMS	1.29 nm ± 0.39 nm	2.66 nm ± 1.12 nm	3.57 nm ± 0.23 nm	4.64 nm ± 1.30 nm	0.86 nm ± 0.26 nm	1.00 nm ± 0.14 nm

3.4.4 Microstructural Characterization of AlN on Crystallized and Amorphous TiNiCu:

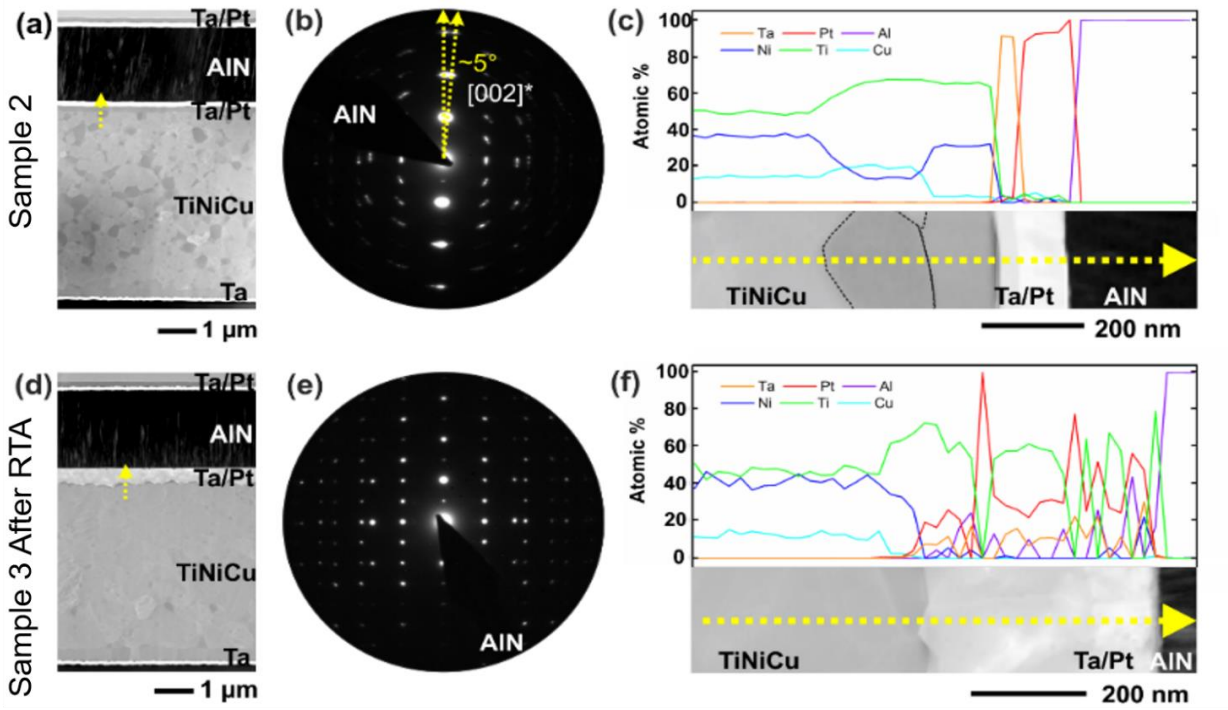

Figure 3.6: (a) STEM image of the cross-section through Sample 2. The yellow arrow labels the position of the EDS profile. (b) ED pattern of the AlN film demonstrating partial out-of-plane tilt of 5° columnar grains. (c) EDS profile showing the quantitative atomic distribution across the interface between AlN and TiNiCu. (d) STEM image of the cross-section of Sample 3 after annealing. (e) ED pattern of the AlN film. (f) EDS profile showing the quantitative atomic distribution across the interface between AlN and TiNiCu.

The chemical integrity, surface morphology, and interface study of the composites fabricated by the two different approaches are analyzed with STEM *Z*-contrast images and energy-dispersive X-ray spectroscopy (EDS). A cross-section image of Sample 2 is shown in **Figure 3.6(a).** The crystalline texture of the AlN film was analyzed by electron diffraction (ED) experiments which show a 5° out-of-plane tilt for the *c*-axis columnar texture of the (002) AlN film depicted in **Figure 3.6(b).** Annealing the TiNiCu before AlN deposition results in a polycrystalline structure with grains sizes of TiNiCu in the range of 100 nm - 400 nm and of different stoichiometry apparent from the brighter and darker *Z*-contrast. To link the observed

differences in *Z*-contrast and morphology in the TiNiCu film to the chemical composition, **Figure 3.6(c)** shows the EDS profiles along the interface region (yellow arrow) and quantified according to the stoichiometry at each measured data point.

The dashed black lines differentiate between grains of different *Z*-contrast and grain morphology, especially at the 140 nm thick interface region. Following the element profiles from left to right, the high *Z*-contrast grains of TiNiCu yield the targeted composition of ~$Ti_{50}Ni_{35}Cu_{15}$. However, upon entering the first low Z-contrast grain the amounts of Ti and Cu increase while Ni decreases yielding an average composition of ~$Ti_{66}Ni_{14}Cu_{20}$. Close to the interface, the Ni content increases while Cu decreases giving a different average composition of ~$Ti_{65}Ni_{31}Cu_{4}$, followed by separate and distinct layers of Ta, Pt, and AlN. A detailed characterization of further common precipitates present in TiNiCu films such as Ti_2Cu was not performed in this study. However, for an in-depth discussion of the Ti_2Cu role the reader is referred to *Dankwort et al.* [118]. The heterogeneous variation in TiNiCu grain stoichiometry would be problematic for reliable ME sensor operation because the stoichiometry is known to strongly influence the formation of enthalpies leading to the degeneracy of the transformation temperatures within the film, hence only partial transformations would be observed upon heating to a specific temperature [35, 119].

In comparison, the cross-section and ED pattern of the AlN film of Sample 3 are presented in **Figure 3.6(d) and 3.6(e)** together with the EDS profiles given in **Figure 3.6(f)**. The most apparent difference between the two composites is the formation of a ~ 420 nm wide diffusion region expanded over the Ti-enriched and Cu-poor TiNiCu grains at the interface to the bottom Ta/Pt electrode by interdiffusion upon RTA. Further discussion about the envisioned diffusion process can be found in the Appendix (**Figure A3.5**, Section 3.6.5). This Ti-enriched and Cu-poor interface grain structure (~340 nm) is evidenced also at the Si substrate/Ta interface. The ED

pattern on the AlN film provides evidence of an excellent *c*-axis texture without any misalignment in the analyzed area of the film.

Concerning the stoichiometry of the SMA film, smaller variations in the *Z*-contrast images are observed, and an average composition of ~$Ti_{50}Ni_{33}Cu_{17}$was measured by EDS. However, close to the diffusion region, the EDS profiles indicate larger stoichiometric deviance of the TiNiCu composition compared to the average composition. Here, it is assumed that Ti diffused into the Ta/Pt layers, breaking up the electrode structure. As a result, Ni (~ 40 at.%) accumulated in the intermediate interface region with respect to the average film stoichiometry. The transformation from the martensite phase (room temperature) into the austenite (120 °C) phase was probed by *in- situ* heating experiments collecting diffraction information at room and high temperatures for both samples. The results are discussed in the Appendix, (**Figure A3.4**, Section 3.6.5).

3.5 Conclusions

High-quality *c*-axis oriented (002) AlN films were obtained on ultra-low fatigue TiNiCu shape memory alloy thin-films on Si substrates. Analytical calculations demonstrate that a wide range of tunability is possible by incorporating magnetoelectric composites onto thin-film shape memory alloys. Variations in the piezoelectric performance of AlN are found to be strongly correlated to the underlying film's surface roughness, grain size, and thickness. While the best crystalline (002) AlN films were obtained on amorphous TiNiCu (Sample 3: As-deposited, $d_{33,f}$ = 6.3 pm/V ± 0.2 pm/V), annealing the composite to 700 °C to crystallize the SMA promoted interdiffusion of Ti into the Ta adhesion layer and Pt electrode layer. There was little observed change in the large longitudinal piezoelectric coefficient from the annealing step (Sample 3: annealed, $d_{33,f}$ = 6.4 pm/V ± 0.2 pm/V); however, an open polarization loop was observed, which indicates a high leakage current in the AlN film. In the case where AlN is

sputtered onto already crystalline TiNiCu, a large piezoelectric coefficient is obtained (Sample 2: as-deposited, $d_{33,f}$ = 6.0 pm/V ± 0.3 pm/V), despite the large surface roughness of crystalline TiNiCu causing a 5° misalignment in the *c-axis* direction. Furthermore, the expected linear polarization [114] of AlN is obtained for this sample; therefore, this method is found to be the most promising fabrication route for tunable magnetoelectric composite applications.

Polycrystalline sputtered AlN will display its best mechanical and electrical performance when deposited onto a substrate with low surface roughness [109, 114]. Since the structural quality of TiNiCu is dependent on the annealing conditions of the composite, future studies should consider significantly lower annealing temperatures (~500 °C) because it was reported to reduce the small grain size and surface roughness for TiNiCu [102]. Another possible solution to reduce the surface roughness of the SMA before AlN deposition is through a chemical-mechanical polish or an electropolishing treatment [120]. Alternatively, these issues could entirely be circumvented if one were to deposit and crystallize the SMA on one side of the silicon wafer followed by the structuring of an AlN / FeCoSiB inverse bi-layer sensor onto the other side of the wafer [111].

Acknowledgments: This work was supported by the German Research Foundation (Deutsche Forschungsgemeinschaft, DFG) through the Collaborative Research Centre CRC 1261 Magnetoelectric Sensors: From Composite Materials to Biomagnetic Diagnostics. This material is based upon work supported by the National Science Foundation Graduate Research Fellowship under Grant No DGE 1840340. The authors acknowledge Prof. Dr. Klaus Rätzke for his assistance in discussing the diffusion processes.

3.6 Appendix

3.6.1 Analytical Calculation and Experimental Demonstration of Resonant Frequency

A. Theory

The primary goal of the analytical calculations performed in this study is to quantify the contribution of the Si thickness (t_{Si}) and NiTi thickness (t_{NiTi}) on the change in mechanical resonant frequency (Δf). The maximum shift is achieved by thermally inducing a reversible phase transformation in the shape memory alloy from martensite to austenite. The resonant frequency of a cantilever-based magnetoelectric (ME) / shape memory alloy (NiTi) / silicon (Si) composites is modeled as the first bending mode of a freestanding cantilever composed of three mechanically coupled thin-film layers: ME / NiTi / Si. The theory behind the calculation of the resonant frequency of a two-layer thin-film cantilever beam is well known [97, 103, 104]. The theory and MATLAB code presented in *Zannon et al.* [103] are employed to expand the calculation to three-layers in order to investigate ME/ NiTi/ Si composites.

The Si and NiTi functional layers will dominate the elastic properties of the vibration due to their large film thickness; therefore, the mechanical contributions of the adhesion and electrode layers can be neglected. To simplify the calculations, the magnetoelectric layer uses the mechanical properties of the piezoelectric layer (AlN) and magnetostrictive layer (FeCoSiB) mechanically coupled together. In all calculations, the ME thickness is assumed t_{ME} = 4 μm to match the functional layer thickness (i.e t_{AlN} = 2 μm, $t_{FeCoSiB}$ = 2 μm) of the fabricated composites experimentally analyzed in this manuscript. Taking a similar approach to *Röbisch et al.* [97] the combined mechanical properties of AlN and FeCoSiB are used to calculate the Young's Modulus (E_{ME} = 230 GPa) and density (ρ_{ME} = 5275 kg/m$^{3)}$ of the ME layer as shown in Equation A1 and

Equation A2, respectively. These properties are estimated by using the thickness weighted average of the AlN and FeCoSiB functional layers.

$$E_{ME} = \frac{t_{AlN}}{t_{AlN}+t_{FeCoSiB}}(E_{AlN}) + \frac{t_{FeCoSiB}}{t_{AlN}+t_{FeCoSiB}}(E_{FeCoSiB}) \quad \text{(Equation A1)}$$

$$\rho_{ME} = \frac{t_{AlN}}{t_{AlN}+t_{FeCoSiB}}(\rho_{AlN}) + \frac{t_{FeCoSiB}}{t_{AlN}+t_{FeCoSiB}}(\rho_{FeCoSiB}) \quad \text{(Equation A2)}$$

As described in *Zannon et al.* [103], the resonant frequency of multi-layer composites in cantilever structures can be described in terms of the moment of inertia, and elastic modulus of the individual layers. As additional thin-film materials layers are added to the composite stack, it will induce a shift in the center of mass (y_{CM} and inertia ($I_X$of the beam layers, as shown in Equations A3 – A6.

$$y_{CM} = (E_1 t_1) * \left(\frac{t_1}{2} + t_2 + t_3\right) + (E_2 t_2) * \left(\frac{t_2}{2} + t_3\right) + (E_3 t_3) * \left(\frac{t_3}{2}\right) \quad \text{(Equation A3)}$$

$$I_1 = \left(\frac{w * {t_1}^3}{12}\right) + (w * t_1) * (\left(\frac{t_1}{2} + t_2 + t_3\right) - y_{CM})^2 \quad \text{(Equation A4)}$$

$$I_2 = \left(\frac{w * {t_2}^3}{12}\right) + (w * t_2) * (\left(\frac{t_2}{2} + t_3\right) - y_{CM})^2 \quad \text{(Equation A5)}$$

$$I_3 = \left(\frac{w * {t_3}^3}{12}\right) + (w * t_3) * * (\left(\frac{t_3}{2}\right) - y_{CM})^2 \quad \text{(Equation A6)}$$

Equation A7 demonstrates the resonant frequency is dependent on the geometrical dimensions of the cantilever: width (w), length (L), and thickness (t_x), as well as the Young's modulus (E_X), density (ρ_x), moment of inertia (I_x), and in-plane surface area (A_x) of each material layer (x = ME, NiTi, Si or 1, 2, 3). Here A is the in-plane surface area: $A_x = w * t_x$ (i.e short-axis cross-section) of the cantilever. λ is an integration constant determined by the boundary conditions (λ = 1.875) for the first bending mode of a cantilever beam [92]. The same cantilever geometry (w = 2.5 mm, L = 25 mm) is held consistent in all calculations.

$$f_r = \frac{1}{2\pi} * \frac{\lambda^2}{L^2} * \sqrt{\frac{(E_1 I_1)+(E_2 I_2)+(E_3 I_3)}{(\rho_1 A_1)+(\rho_2 A_2)+(\rho_3 A_3)}} = \frac{1}{2\pi} * \frac{\lambda^2}{L^2} * \sqrt{\frac{(E_{ME} I_{ME})+(E_{NiTi} I_{NiTi})+(E_{Si} I_{Si})}{(\rho_{ME} A_{ME})+(\rho_{NiTi} A_{NiTi})+(\rho_{Si} A_{Si})}} \quad \text{(Equation A7)}$$

Since it is possible to gradually and reversibly change the Young's modulus of NiTi by inducing a partial phase transformation, a gradual change in the resonant frequency can be obtained. The largest Δf will occur when there is a complete phase transformation from the low-temperature martensite phase ($E_{NiTi,martensite}$ = 41 GPa) to the high-temperature austenite phase ($E_{NiTi,austenite}$ = 83 GPa). Equation A8 demonstrates the expression used to calculate the maximum Δf_r.

$$\Delta f_r = \frac{f_{r,NiTi_{austenite}} - f_{r,NiTi_{martensite}}}{f_{r,NiTi_{martensite}}} * 100\% \quad \text{(Equation A8)}$$

B. Experimental Verification of the Model:

The MATLAB code output of the first bending mode of a 4 μm ME / 5.1 μm NiTi / 350 μm Si composite predicts a maximum resonant frequency shift (Δf = 0.5%) from 768 Hz to 772 Hz. The mechanical properties of binary NiTi ($E_{Martensite}$ = 41 GPa, $E_{Austenite}$ = 83 GPa, ρ = 6450 kg/m^3) [96] are well studied and like that of TiNiCu ($E_{Austenite}$ = 78 GPa, ρ = 6500 kg/m^3) [102]. Therefore, we expect a maximum deflection (i.e first bending mode resonant frequency) of the fabricated 2 μm AlN/ 5.1 μm TiNiCu/ 350 μm Si/ 2 μm FeCoSiB cantilever composite to fall within this range. **Figure A3.1(a)** demonstrates the cross-section of the ME/ SMA/ Si composites investigated through analytical calculations. This is the analytical equivalent composite to the fabricated experimental composite, shown in **Figure A3.1(b)**

The experimental resonant frequency was obtained using an optical read-out deflection set-up, similar to the one described elsewhere [121]. The end 1 mm of the fabricated 2.5 mm x 26 mm

cantilever ME/ SMA/ Si composite was fixed onto a holder (freestanding length 25 mm). A time varying magnetic field, having a nonzero DC component matching the working point of the ME composite, is used to excite the magnetostrictive FeCoSiB layer, which is mechanically coupled to the piezoelectric layer of AlN, thus inducing the composite magnetoelectric effect. When this composite is sent into mechanical resonance, a vast increase in deflection amplitude is observed. **Figure A3.1(c)** shows the obtained experimental mechanical resonance frequency at 771 Hz with a corresponding phase change also at 771 Hz which indicates a maximum deflection. This result is in excellent agreement with the analytical calculation, using the mechanical properties of binary NiTi, which predicts a resonant frequency of 768 Hz - 772 Hz.

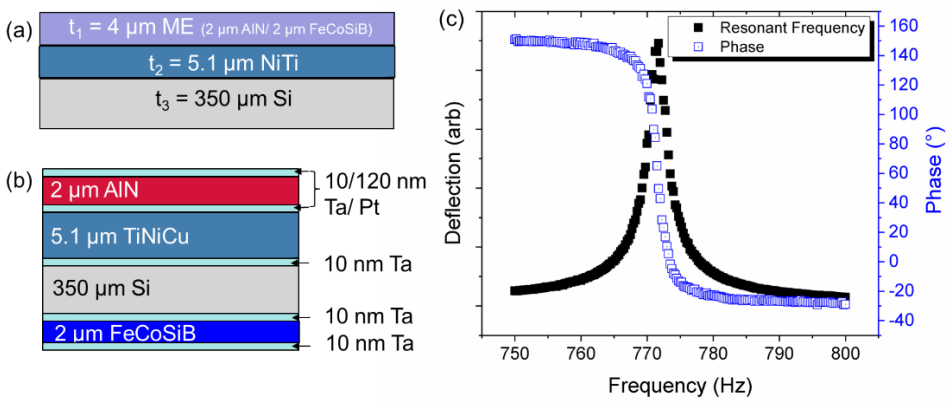

Figure A3.1: (a) Cross-section of the modeled ME / NiTi / Si composite used in analytical frequency calculations. (b) Cross-section of the fabricated AlN / TiNiCu/ Si/ FeCoSiB composite. (c) The resonant frequency and phase measurement of AlN / TiNiCu/ Si/ FeCoSiB composite taken by optical beam deflection while magnetically excited. An experimental resonant frequency of 771 Hz was obtained.

3.6.2 Fabrication Parameters:

The texture and smoothness of the underlying substrate will strongly influence the piezoelectric performance of AlN thin-films [114]. To remove any impurities from the substrates, all Si substrates were first cleaned in a series of acetone, isopropyl alcohol, and water ultra-sonic baths, followed by heating on a hot plate to 100 °C. All layers were sputtered using a Von Ardenne (CS 730S) magnetron cluster system, capable of DC, RF, and Pulsed DC sputtering. Prior to all depositions, a free-sputter for a minimum of 5 minutes took place on all targets to ensure the removal of impurities. Prior to deposition of the adhesion layer (Ta) and piezoelectric layer (AlN), the first few nm of the sample was plasma etched in Ar atmosphere.

Low-temperature magnetron sputtering of AlN from an aluminum (Al) target in a reactive environment is a well-established process. Here, we follow the recipe established by *Yarar et al.* [109]. AlN is deposited through a pulsed DC reactive sputtering process using ultra-pure (5N) N_2 gas and a high-purity Al-target (99.999%). The Al target was first conditioned via DC free-sputtering with Argon gas (Ar) on an empty carrier plate for 15 minutes. Afterward, AlN was also conditioned for 15 minutes on the carrier plate via pulsed DC reactive sputtering, powered by a Pinnacle Plus+ 10kW (Advanced Energy) asymmetric bipolar pulsed DC power supply sputtering operating at a frequency of 250 kHz with 1.6 µs reverse time. After these conditioning steps took place, ~2 µm of AlN was sputtered under the same conditions on the sample for 42 minutes. Finally, ~2 µm FeCoSiB is sandwiched between two layers of Ta (adhesion and protection layers) by means of RF sputtering on the backside of the wafer. The sputtering parameters used for depositions of all material layers in the fabricated composite are shown in **Table 3.3**.

Table 3.3: Sputter deposition and fabrication processing parameters of each material in the AlN/ TiNiCu/ Si/ FeCoSiB composites

Material Layer	Sputter Target [diameter]	Power	Sputter Pressure	Ar / N_2 flow	Time	Film thickness	Additional Processing Notes
Standard DC Sputtering:							
Pre-etch	-----	100 W	5E-3 mbar	30 Ar	1 min	----	Removes first few nm
Adhesion	Ta [8in]	200 W	4E-3 mbar	30 Ar	1 min	20 nm	
SMA	$Ti_{50}Ni_{35}Cu_{15}$ [8 in]	600 W	2E-3 mbar	25 Ar	66 min	5.1 µm	
Adhesion	Ta [8 in]	200 W	4E-3 mbar	30 Ar	0.5 min	10 nm	
Bottom Electrode	Pt [4 in]	100 W	8E-3 mbar	25 Ar	1.5 min	100 nm	
Free Sputter	Al [8 in]	200 W	6E-3 mbar	30 Ar	15 min	----------	
Pulsed DC Reactive Sputtering: (after Al and AlN conditioning steps)							
Piezoelectric (AlN)	Al [8 in]	1500 W pDC	1.7E-3 mbar	10 N_2	42 min	2 µm	Time = 1.6 µs, Frequency = 250 kHz
Standard DC Sputtering:							
Adhesion	Ta [8 in]	200 W	4E-3 mbar	30 Ar	0.5 min	10 nm	
Top Electrode	Pt [4 in]	100 W	8E-3 mbar	25 Ar	1.5 min	100 nm	
RF Sputtering:							
Adhesion	Ta [8 in]	400 W	4E-3 mbar	30 Ar	17 seconds	10 nm	
Magnetostrictive (FeCoSiB)	$(Fe_{90}Co_{10})_{78}Si_{12}B_{10}$ [8 in]	200 W	6E-3 mbar	40 Ar	230 min	2 µm	
Protection	Ta [8 in]	400 W	4E-3 mbar	30 Ar	17 seconds	10 nm	

3.6.3 Shape Memory Alloy Characterization:

Temperature-dependent XRD (Anton-Paar DHS 1100) measurements on a fabricated AlN/TiNiCu/ Si composite were performed to observe a fully reversible phase transformation. between 30 °C to 100 °C to ensure a full reversible phase transformation from martensite to austenite and again at 30 °C to evaluate if TiNiCu fully returns to martensite. **Figure A3.2(a)** demonstrates upon heating to 100 °C in 10°C steps, no observable change in the (002) AlN peak position ($2\theta = \sim 36°$) or intensity is detected. This indicates that the phase transformation does not

affect the structural properties of the piezoelectric material. **Figure A3.2(b) - Figure A3.2(d)** show selected temperature-dependent XRD peaks confirming a full phase transformation from the B19 (martensite orthorhombic structure, space group PMMB #51) to the B2 (austenite simple cubic structure) upon heating to temperatures above 70 °C. The expected peak position of the martensite (M) and austenite (A) peaks obtained from the TOPAS software are listed in **Table 3.4.** These transformation temperatures are in good agreement with the DSC data performed on the 20 μm thick freestanding TiNiCu films shown in **Figure 3.3** in the main manuscript.

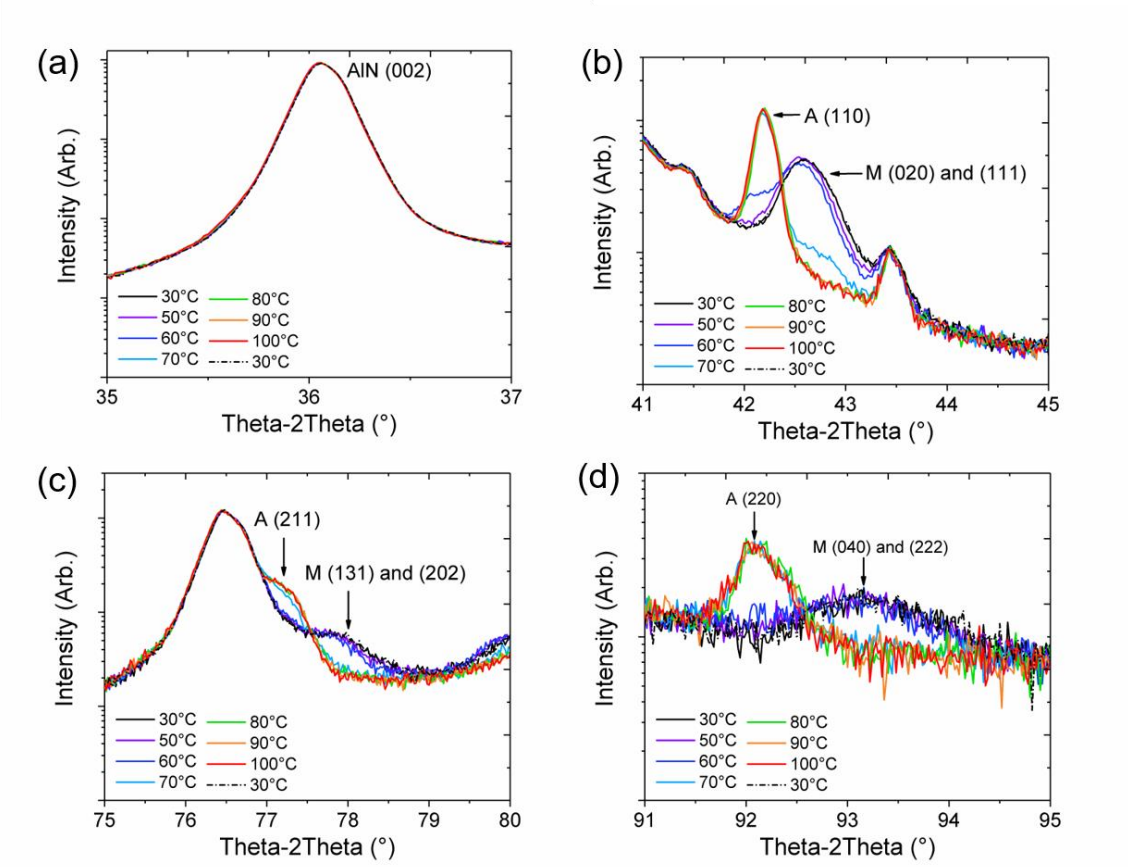

Figure A3.2: Temperature-dependent XRD measurements on an AlN/ TiNiCu/ Si composite (Sample 3 after annealing) heated from 30 °C to 100 °C and back to 30 °C. (a) (002) AlN peak demonstrating no change upon heating to 100 °C. (b) – (d) Shows the select temperature-dependent diffractograms demonstrating the phase transformation from martensite (M) to austenite (A) occurs between 60 – 70 °C in TiNiCu films after annealing at 700 °C for 15 minutes.

Table 3.4: Select data-base x-ray diffraction peak positions for TiNiCu martensite and austenite phases

Martensite Peaks (B19)				Austenite Peaks (B2)	
Angle	Plane	Angle	Plane	Angle	Plane
42.44°	(020)	42.64°	(111)	42.09°	(110)
77.79°	(131)	78.25°	(202)	76.77°	(211)
92.75°	(040)	93.34°	(222)	91.60°	(220)

3.6.4 Piezoelectric Characterization of (002) AlN:

The work function of the electrode material may have an impact on the electrical properties of AlN [114]. Our composites use standard (111) Pt as both the bottom and top electrodes because previously (111) Pt was shown to promote a (002) AlN texture [109]. The electrical properties (polarization and displacement) of Samples 1, 2, and 3 were obtained via double beam laser interferometer (DBLI) measurements. The samples were prepared into a parallel plate capacitor geometry by sputter depositing Pt through a 1000 μm diameter shadow mask. This resulted in a top electrode area ranging between 0.968 mm^2 – 1.19 mm^2. Previously, annealing AlN to temperatures as high as 500 °C was found to improve the piezoelectric performance [50]. We analyze the structural and piezoelectric properties of AlN in Samples 1-3 after annealing at 700 °C for 15 minutes. Polarization and displacement curves were taken at a minimum of three spots on each sample to generate an average $d_{33,f}$ at each applied voltage (i.e 10V, 20V, 50V, and 100V). The slope of the displacement curves at each applied voltage are used to obtain $d_{33,f}$. The average of all values was used to obtain the mean $d_{33,f}$ ± standard deviation of each sample, as shown in **Table 3.5.**

Table 3.5: Average $d_{33,f}$ measurements obtained via DBLI on Samples 1 – 3 before (as deposited) and after annealing, varying the voltage between 10V – 100V

Voltage	Sample 1: As-deposited	Sample 2: As-deposited	Sample 3: As-deposited	Sample 1 - Annealed	Sample 2 - Annealed	Sample 3 - Annealed
10 V	6.1 pm/V	5.6 pm/V	6.1 pm/V	5.8 pm/V	6.4 pm/V	6.3 pm/V
20 V	5.9 pm/V	6.0 pm/V	6.3 pm/V	5.7 pm/V	6.2 pm/V	6.5 pm/V
50 V	5.4 pm/V	5.9 pm/V	6.3 pm/V	5.7 pm/V	6.5 pm/V	6.6 pm/V
100 V	5.6 pm/V	6.3 pm/V	6.5 pm/V	6.4 pm/V	6.4 pm/V	6.2 pm/V
Average $d_{33,f}$	5.8 pm/V ± 0.3 pm/V	6.0 pm/V ± 0.3 pm/V	6.3 pm/V ± 0.2 pm/V	5.9 pm/V ± 0.3 pm/V	6.4 pm/V ± 0.1 pm/V	6.4 pm/V ± 0.2 pm/V

Figure A3.3 demonstrates the polarization and displacement curves taken at 100V (i.e electric field of ± 500 kV/cm) for Samples 1 – 3. Polarization is well-known to be dependent on grain size, domain structure, and domain mobility [114]. The difference in the polarization hysteresis loop behavior between the as-deposited and after-annealed state of each sample is likely due to the variation in leakage current from changes in the grain size, surface roughness, and *c*- axis growth [114]. Previously, it was found that grain boundaries act as pinning centers for polarization, thus polarization switching was easier for large AlN grains [114]. In general, it was found a lower surface roughness of the bottom electrode results in a lower leakage current. All samples in the as- deposited state show similar $d_{33,f}$, values and expected linear polarization behavior. In agreement with other studies [50], annealing AlN was found to improve the $d_{33,f}$, values. However, upon annealing all samples, an open polarization loop is obtained which generally indicates a larger leakage current and higher resistive losses. The polarization behavior shown in **Figure A3.3** is similar to the behavior of AlN grown on Ti, Pt, and Al electrodes [114]. These results prompted the investigation of the interfaces to correlate microstructure changes to the electrical and structural properties of AlN. Future studies should consider a more in-depth analysis of the underlying SMA effects on the electric properties of sputtered AlN films.

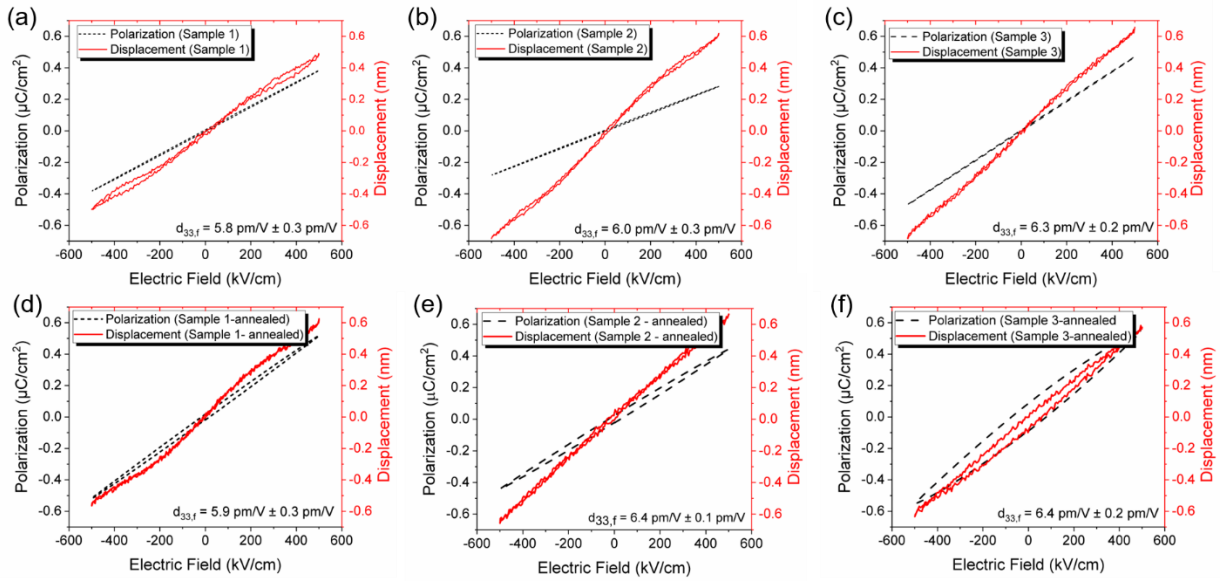

Figure A3.3: Polarization and displacement curves obtained from DBLI measurements at 100V. Samples 1, 2, and 3 (a-c) in the as-deposited state and (d-f) after rapid thermal annealing (RTA).

3.6.5 Micro-structural characterization of SMA ME composites:
A. In-Situ Temperature Dependent TEM:

The average structural transformation of the TiNiCu film was investigated by heating the samples *in-situ* to temperatures above the austenite finish temperature A_f = 69 °C. The results are presented in **Figure A3.4** showing the electron diffraction (ED) patterns and rotational average plots of the intensity distribution at room temperature and at 120°C, respectively. The phase transformation from the martensite into the parent austenite phase is evidenced for both films by smoothing of the ED patterns and the profiles. This is because the low-symmetry orthorhombic B19 phase is transformed into the high-symmetry cubic B2 austenite phase; thereby the number of reflections is significantly reduced. Prior studies on the phase transformation mechanism in Ti- rich TiNiCu films revealed Ti-rich nano-precipitates embedded in the base alloy to serve as epitaxial misfit strain mediators between the B19 and B2 phases [18]. These precipitates promote

the transformation upon temperature cycling by epitaxial stabilization of a B2 transition layer, even in the martensite stable regime. In addition, at least in the case for Sample 2 where the TiNiCu film crystallized prior to AlN deposition, the presence of larger precipitates presumably of the kind Ti_2Cu and Ti_2Ni was evidenced and contributed as non-active phases to the ED series. More details of the microstructure of Ti-rich TiNiCu films can be found in *Dankwort et al.* [118]. Hence, despite the presence of precipitate phases, the *in-situ* analysis demonstrated the transformation of the active martensite to the austenite phase for both Samples 2 and 3.

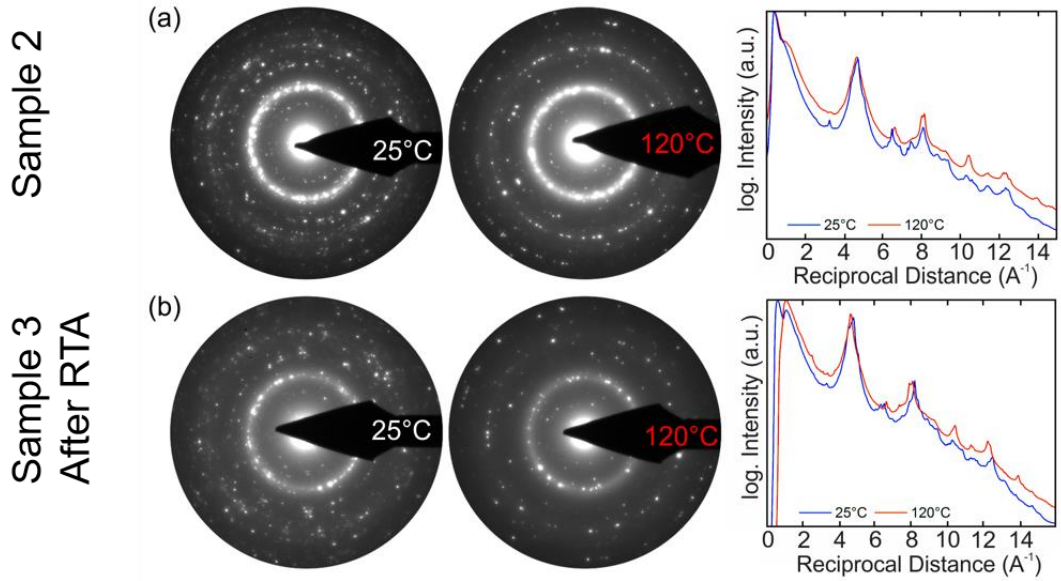

Figure A3.4: ED pattern of TiNiCu at room temperature and at 120°C and rotational average (RA) plots showing the structural change upon transformation. (a) Composite SMA was crystallized prior to AlN growth (Sample 2) (b) SMA was crystallized after AlN growth (Sample 3: annealed). After heating the films above the austenite finish temperature A_f both samples show distinct smoothing of the RA plots indicating the structural transformation.

B. Discussion of Diffusion

The formation of a diffusion region is sketched in **Figure A3.5** resembling simplified experimental EDS concentration profile data. Herein, the stages of the envisioned diffusion process at the TiNiCu/Ta/Pt interface are depicted under the following assumptions: The situation where Ta/Pt/AlN is deposited after rapid thermal annealing of TiNiCu (Sample 2), is shown in **Figure A3.5** (top). At the beginning of the annealing process, ($t < 20$ s) a Cu-poor and Ti-enriched interface region is formed immediately (blue box). Such interface morphology was also observed at the Si substrate/ Ta-adhesion interface layer in both investigated composites after 15 minutes of annealing. The situation where Ta/Pt/AlN is annealed with TiNiCu (Sample 3) promotes diffusion originating from the grains at the interface, resulting in a mixed polycrystalline region under complete dissolution of the electrode structure, shown in **Figure A3.5** (bottom).

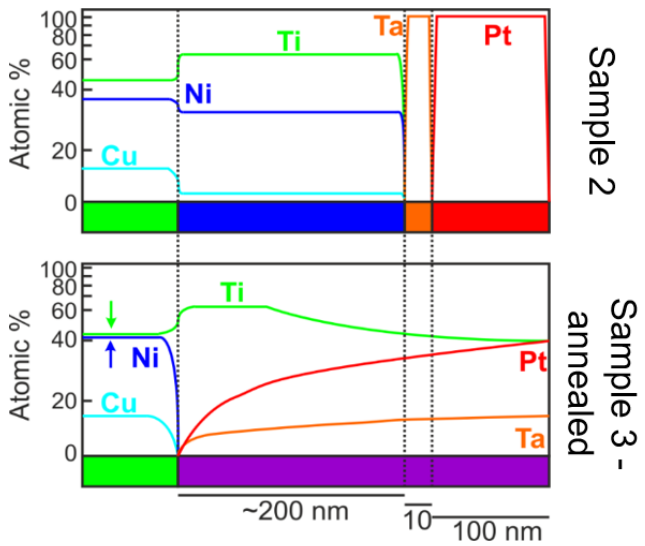

Figure A3.5: Sketch showing the measured EDS concentration profile across the TiNiCu/Ta/Pt interface. (top) Sample 2, the situation after rapid crystallization, no diffusion took place and a Cu-poor and Ti-enriched interface layer is established. (bottom) Sample 3: annealed, situation after diffusion, Ti diffuses towards the Pt layer and Ta, Pt diffuses towards the TiNiCu matrix. green box: TiNiCu matrix, blue box: Cu-poor and Ti-rich crystal interface, orange box: Ta-layer, red box: Pt-layer, violet box: diffusion region.

The complete interpretation of diffusion in a multicomponent system with only two sets of data is not possible. In the following, we will give a coarse idea of the diffusion mechanisms taking place along the following lines and boundary conditions.

Upon annealing, TiNiCu crystallizes immediately, as the 700 °C annealing temperature is much larger than the crystallization temperature of most NiTi films which is in the vicinity of 500°C [122]. From TEM it is clear that all layers are polycrystalline with lateral grain sizes of around 200 nm in the TiNiCu alloy due to crystallization and around 10 nm and 100 nm in Ta and Pt layers (grain size on the order of the film thickness). This setup is regarded as an interdiffusion experiment in a multicomponent alloy with fine grain size.

To discuss this, thermodynamics (i.e. attractive and repulsive interactions of the up to five components, possible intermetallic phase formation, solubility limits) as well as kinetics (tracer and chemical diffusion in the bulk as well as grain boundary diffusion) must be taken into account. We start by estimating the diffusivities needed to explain the change in the concentration profiles, using the well-known parabolic growth law [123]

$$\varkappa = 2\sqrt{D(T) \cdot t}$$

with t = 15 min and $\varkappa$ = 100 nm being roughly half of the length of the diffusion zone (see **Figure A3.5**) results in diffusivities of the order of 10^{-18}m²/s.

However, it is not clear, whether bulk or grain boundary diffusion is dominant, with the latter being orders of magnitude faster than the former. No data for grain boundary diffusion in this system are available [124]. Bulk diffusivities can be estimated from known data collections [123] depending on the matrix and diffusing element. Calculations result in diffusivities between 4.2×10^{-21}m²/s for Fe in Ta and 5.6×10^{-21} for Al in Ta (according to tables in *Neumann et al.*

[125]). These values for bulk diffusivity are much too small compared to the needed 10^{-18}m²/s. However, it must be stressed that grain boundary diffusion might occur as well and is known to be three to five orders of magnitude larger than the bulk values calculated here [123, 124, 126]. Thus, from a kinetics and diffusion point of view, such concentration profiles as shown in **Figure A3.5** are possible.

To understand the sequence of processes and the shape of the concentration profiles in detail, the thermodynamics of the binary systems serve as acceptable approximations to estimate solubility limits (thermodynamic factor of diffusion) [123] in multiple phase systems. The binary phase diagrams describe the system {Ti-Ta}: good solubility with two intermetallic phases (IPs) [127], for {Ta-Pt}: little solubility and a large number of IPs [128], for {Ti-Pt}: little solubility with a large number of IPs [129], for {Ni-Ta}: medium solubility and large number of IPs [130], and for {Cu-Ta}: no solubility [131].

From the good solubility of Ti in Ta and the small grain size of the Ta-layer we expect that first the 10 nm Ta barrier is dissolved by interdiffusion via grain boundary diffusion. Then, without an intact Ta barrier, Ta and Pt start to diffuse towards the boundary of the Ti-enriched interface layer, Ta also diffuses into the Pt-layer. Formation of binary or ternary Ti-Ta-Pt phases having no solubility of Ni, causes a push-back of Ni towards the matrix resulting in a detectable Ni-enrichment there. Cu is also pushed back due to the low solubility of Ta in Cu. Note, the exact nature of phases formed within this diffusion region and the respective grain sizes have not been determined and are assumed to be strongly heterogeneous.

In summary, it is consistent with kinetics and phase diagrams that first crystallization occurs, then the dissolution of the Ta barrier via grain boundary diffusion and then grain boundary diffusion of Ta and Pt into the remaining matrix pushing back Ni and Cu.

Chapter 4. Publication: TiNiHf/SiO_2/Si Shape Memory Film Composites for Bi-Directional Micro Actuation

Own contributions to the following article[1].

- sample fabrication (large fraction)
- differential scanning calorimetry (large fraction)
- structural characterization (moderate fraction)
- electrical resistance measurements (minor fraction)
- cantilever deflection measurements (moderate fraction)
- constitutional modeling (minor fraction)
- interpretation of the results (large fraction)
- writing of the manuscript (large fraction)

Reproduced from

Curtis, S.M.*, Sielenkämper, M.*, Arivanandhan, G.*, Dengiz, D., Li, Z., Jetter, J., Hanke, L., Bumke, L., Quandt, E., Wulfinghoff, S. and Kohl, M., 2022. TiNiHf/SiO_2/Si shape memory film composites for bi-directional micro actuation. International Journal of Smart and Nano Materials, pp.1-22. https://doi.org/10.1080/19475411.2022.2071352

* Authors contributed equally to this work

[1] this page is required by regulations

Motivation:

The first phase of the DFG Priority Program SPP 2206 - Cooperative Multistage Multistable Microactuator Systems (KOMMMA) took place between 2019 – 2022. Specifically, I lead the "Materials Development" team on the sub-project Cooperative Actuator Systems for Nanomechanics and Nanophotonics. This was an interdisciplinary collaboration between three professors in Inorganic Functional Materials (Prof. Eckhard Quandt) and Computational Materials Science (Prof. Stephan Wulfinghoff) at Kiel University, and Microstructure Technology (Prof. Manfred Kohl) at Karlsruhe Institute of Technology. The following chapter describes results that cumulated after a three-year-long collaboration between the Ph.D. students of the professors. M.Sc. Marian Selenkamper, M.Sc. Gowtham Arivanandhan, and I contributed equally to the results discussed in this chapter.

The primary focus of my project was to research the functional properties of sputtered TiNiHf shape memory alloy (SMA) films with micro and nanoscale thicknesses for the development of bi-directional and bistable actuators. The thermal transformation temperatures (e.g., austenite start/finish (A_s, A_f) and martensite start/finish (M_s, M_f) temperatures and thermal hysteresis width (ΔT)) of fabricated TiNiHf films are investigated for use in novel PMMA/TiNiHf/Si trimorph composites. TiNiHf films should meet the requirements of bistable actuators established by previous works on PMMA/TiNiHf/Mo/PMMA composites [22–25]. The primary requirement is that the glass transition temperature of the PMMA (T_g = 105 °C) polymer must fall within the thermal hysteresis ($M_s < T_g < A_s$) of the TiNiHf SMA. The results presented in the manuscript below evaluate the influence of substrate and film thickness on the phase transformation properties of $Ti_{40.4}Ni_{48}Hf_{11.6}$ films scaled down from 21 μm to 110 nm.

4.1 Abstract:

The martensitic phase transformation in $Ti_{40.4}Ni_{48}Hf_{11.6}$ shape memory alloys is leveraged for bi-directional actuation with TiNiHf/SiO_2/Si composites. The shape memory properties of magnetron sputtered $Ti_{40.4}Ni_{48}Hf_{11.6}$ films annealed at 635 °C – 5 minutes are influenced by film thickness and the underlying substrate. Decreasing TiNiHf film thickness from 21 μm to 110 nm results in the reduction of all characteristic transformation temperatures until a critical thickness is reached. Particularly, $Ti_{40.4}Ni_{48}Hf_{11.6}$ thin-films as low as 220 nm show transformations above room temperature when deposited on SiO_2 buffer layer which is of great interest in nano-actuation. In comparison, 220 nm films on Si substrates are austenitic at room temperature, and thus not suitable for actuation. Thermal fatigue tests on TiNiHf/SiO_2/Si bimorphs demonstrate better functional fatigue characteristics than free-standing films, with an average reduction of 15 °C after 125 cycles, with temperature stabilization subsequently. Experimental bi-directional actuation results are promising in the development of bistable actuators within a PMMA/TiNiHf/Si trimorph composite, whereby the additional PMMA layer undergoes a glass transition at 105 °C. With the aid of constitutive modeling, a route is elaborated on how bistable actuation can be achieved at micro- to nano-scales by showing favorable thickness combinations of PMMA/TiNiHf/Si composite.

4.2 Introduction:

Next-generation of silicon (Si)-based nanophotonic and nanomechanical devices, such as optical waveguide switches and routers in advanced communication technology, demand for ultra-small (micro and nano) actuators allowing for large displacements compared to their footprint size [132]. In particular, bi-directional and bistable actuators that could be directly integrated onto Si

chips are attractive for such applications [133]. Actuators based on sputtered thin-film NiTiX (X= Zr, Hf, Pd, Cu Pt, Au) shape memory alloys (SMAs) have the largest power-to-weight ratio among lightweight technologies. SMA actuators are known to exhibit limited speed. However, heat transfer scales favorably with downscaling allowing for an increase of actuation frequency. At the nano-scale, frequencies may reach the kHz regime depending on the heat transfer rate and the fraction of transforming SMA material [134]. This investigation focuses on a route for the design and fabrication of quasi-stationary bi-directional and bistable switching devices with large strokes and forces that could be scaled down to nm dimensions, which may not be achieved by other technologies. Sputtered TiNiHf SMAs are attractive for this investigation due to its lower cost, large transformation temperatures, and it offers high work density among various SMAs [41, 135, 136]. SMA/Si bimorph nano-actuators have been fabricated using standard E-beam lithography, wet etching, and micro-machining with conventional plasma etching techniques (e.g. RIE, IBE) [1, 6, 7] [9]. These bimorph actuators take advantage of the combined bimorph and shape memory effect which arises when SMAs are sputtered on a substrate with a different coefficient of thermal expansion (CTE) [7, 137]. In the case of this work, this is between the substrate, silicon ($\alpha_{Si} = 2.6 \times 10^{-6} K^{-1}$) [138], and the two different crystallographic phases of TiNiHf (cubic and monoclinic), which are dependent on atomic composition. For example, for a $TiNiHf_{20}$ alloy, austenite's CTE is $\alpha_A = 49 \times 10^{-6} K^{-1}$ and the isotropic polycrystalline CTE value for martensite phase is calculated to be $\alpha_M = 9.5 \times 10^{-6} K^{-1}$ [139, 140]. Another advantage of TiNiHf/Si bimorph actuators is the prospect of developing bistable actuation by adding a third layer of polymer with a glass transition temperature (T_g) that falls in between the martensite and austenite phase transformation temperatures of the SMA [23–25]. Alternatively, bistable actuation

can be achieved by adding an SMA with a narrow hysteresis (e.g. TiNiCu) as the third layer [99, 137, 141].

Controlling actuation precisely with Ni-lean TiNiHf is challenging compared to other SMAs like Ni-rich TiNiHf, NiTi, and TiNiCu, as they suffer from lower transformation strains [41], unstable transformation temperatures with thermal cycling [39], and they have low strength against dislocation plasticity [42]. Furthermore, the large thermal hysteresis reflects poor crystallographic compatibility between the martensite and austenite phases [47, 142] which is known to lead to unwanted effects such as structural/functional fatigue, and a change in volume during the phase transformation, known as the volume effect [139]. The larger thermal hysteresis is detrimental to the lifetime and energy efficiency of TiNiHf devices [15]. These problems may be overcome by training TiNiHf SMAs [143, 144], aging Ni-rich NiTiHf compositions [40, 42, 47, 145], or designing TiNiHf-based layered bi-/multimorph composites [146]. The functional and structural fatigue properties in TiNiHf can be controlled by composition and microstructure (grain size, precipitate size, precipitate homogeneity) which is dependent on annealing conditions [39, 135]. Even though Ni-lean TiNiHf alloys are claimed to have poor functional stability, previously *Bechtold et. al* [15] showed that 20 μm–25 μm thick $Ni_{49.2}Ti_{31.4}Hf_{19.3}$ films can undergo a phase transformation for an average of 1.5 x 10^6 actuation cycles when tested to a maximum critical stress of 300 MPa. However, when the maximum critical stress was increased to 450 MPa, the number of cycles until failure was reduced to an average of 65K. Improved fatigue in these sputtered Ni-lean TiNiHf alloys samples could be due to small grain size (~100 nm) and finely dispersed small precipitates at the grain boundaries [15]. Another advantage of Ni-lean TiNiHf alloys is they can be heat treated at moderate temperatures for a short amount of time to generate

fine, homogeneous distributions of coherent zone structures and Ti_2Ni-type precipitates, which can strengthen the lattice against slip [135, 147].

Film thickness effects on the transformation temperatures of TiNiHf/Si bimorphs must be taken into account when designing TiNiHf actuators. This is specifically of interest for bistable nano-actuators because the SMA transformation temperatures need to be coupled to the transition temperatures of the third layer (e.g., polymer, additional SMA). Decreasing SMA film thickness from micro to nano-scale is known to decrease the martensitic transformation temperatures for several SMA systems [148–150]. Sputtered TiNiHf thin-films are also reported to have lower transformation temperatures compared to bulk material of similar compositions, attributed possibly to be due to finer grain structures [147]. Several studies explore the properties of bulk TiNiHf [43–46], freestanding TiNiHf films [15], TiNiHf films on Mo substrates [137, 151], and TiNiHf films on silicon substrates [143, 147, 152]; however, there are only a few studies that show the properties of sputtered TiNiHf films on silicon oxide (SiO_2) buffer layers on Si substrates [135].

In this work, thickness effects and functional fatigue characteristics are investigated in free-standing TiNiHf films (21 µm – 5 µm) and films 5 µm down to 110 nm on Si substrates with and without SiO_2 buffer layers. The influence of film thickness on the transition temperatures of TiNiHf/Si and TiNiHf/SiO_2/Si bimorphs are compared and limits for downscaling to a scale usable for nanodevices are discussed. The possibilities of downscaling and tailoring the properties make TiNiHf a promising material in the development of bistable nano actuators with an additional PMMA layer to the bimorph. A thermomechanically coupled finite element model is also implemented to guide the design of favorable thickness combinations of the PMMA/TiNiHf/Si composite layers to achieve such bistable nanoactuators.

4.3 Methods and Materials

4.3.1 Preparation of Freestanding TiNiHf Films:

Structured freestanding amorphous $Ti_{40.4}Ni_{48}Hf_{11.6}$ films were fabricated into dogbone geometries through a combination of UV-lithography, DC magnetron sputtering, and a wet chemical etching process, as described in detail by *Lima de Miranda et. al* [29]. A Von Ardenne CS730S (Von Ardenne, Germany, base pressure $< 3 \times 10^{-7}$ mbar) cluster magnetron sputtering device was used to sputter amorphous $Ti_{40.4}Ni_{48}Hf_{11.6}$ films onto a pre-structured substrate using a multilayer sputter deposition approach. A 4-inch $Ti_{42}Ni_{43}Hf_{15}$ target (Ingpuls, Germany) was sputtered for 35 seconds (deposition layer thickness of ~57 nm, pressure of 2.3×10^{-3} mbar, argon flow of 25 sccm, and power of 150 W). Next, an 8-inch pure Ti target was sputtered for 10 seconds (deposition layer thickness of ~10 nm, pressure of 2.3×10^{-3} mbar, argon flow of 25 sccm, and power of 100W). By repeating this multilayer deposition sequence, amorphous freestanding Ti/TiNiHf films were sputtered with varying thicknesses (5±0.5 μm, 10±1 μm, and 21±2 μm). Due to the sputter yield, films are typically 10-15% thinner at the edge of a 4-inch wafer compared to the center. Rapid thermal annealing (Createc Fischer RTA-6 SY09, Germany) was used to crystallize the amorphous films and homogenize the microstructure. Different RTA temperatures between 635 °C – 750 °C and times between 5 minutes and 60 minutes were tested before selecting on final heat treatment for all samples of 635 °C – 5 minutes.

The nominal film composition was determined using a Helios NanoLab 600 scanning electron microscopy (SEM) (FEI, Germany) equipped with an energy-dispersive X-ray spectroscopy (EDX) silicon drift detector (Oxford Instruments, UK). Qualitative analysis used $Ti_{49.60}Ni_{50.40}$ binary standard, however, the error on all reported compositional data is around ± 0.5 at.%. EDX measurements were taken for sputtered amorphous TiNiHf film on a 100 mm

silicon substrate. The average film composition was determined to be $Ti_{40.4}Ni_{48}Hf_{11.6}$ for all samples. Slight compositional variations are expected to be sources of error in the following experiments.

4.3.2 Preparation of TiNiHf/Si and TiNiHf/SiO_2/Si Bimorphs

TiNiHf/Si and TiNiHf/SiO_2/Si bimorph structures were prepared using the same multilayer sputter approach described above onto chips with lateral dimensions of 20 mm x 20 mm. Amorphous $Ti_{40.4}Ni_{48}Hf_{11.6}$ films of different thicknesses (5±0.5 µm, 2±0.2 µm, 0.88±0.08 µm, 0.44±0.04 µm, 0.22±0.02 µm, and 0.11±0.01 µm) were deposited and annealed on 525±20 µm (001) silicon substrates (Siegert Wafer, Germany) and 1.5 µm SiO_2/ 525±25 µm (001) silicon substrates (MicroChemicals, Germany). TiNiHf films on SiO_2/Si substrates are ~10 % thicker than the films on Si substrates because the SiO_2/Si substrates were sputtered in the direct center of the device, while the pure Si substrates were sputtered adjacent to the SiO_2/Si sample. TiNiHf films with two different thicknesses (2±0.1 µm and 0.88±0.04 µm) were also sputtered onto 100 nm SiO_2/ 300±3 µm (100) Si substrates (Si-mat silicon, Germany), pre-structured into cantilevers (3.5 mm x 20 mm) for bi-directional actuation measurements. All film composites were annealed via RTA at 635 °C – 5 min.

4.3.3 Tensile Testing

The mechanical properties of TiNiHf films were determined using a high-temperature tensile test on freestanding TiNiHf films. The dogbone geometry has been chosen with width and length of 500 µm and 4 mm, respectively. The tensile tests were conducted using a displacement-controlled micro-tensile setup equipped with a load cell (KM26z-0.2kN, ME measuring systems) for force measurements and a digital camera (Pike 505, Allied Vision Technology) to record

images for measurement of corresponding strain values using non-contact digital image correlation (DIC) method. The cross-correlation of images with speckle patterns is evaluated using MATLAB code.

4.3.4 Differential Scanning Calorimetry (DSC):

Thermal analysis, as well as thermal cycling on freestanding SMA films (thickness of 5 µm, 10 µm, 21 µm) were conducted on a differential scanning calorimeter (DSC) 204 F1 Phoenix (Netzsch, Germany) with a heating and cooling rate of 10 °C min^{-1}. The transformation temperatures and latent heat of the SMA are determined using the software Proteus 7.1.0 by the tangent method. Thermal hysteresis is calculated according to $\Delta T = (A_s + A_f - M_s - M_f)/2$, where A_s/A_f correspond to austenite start and finish temperatures and M_s/M_f correspond to martensite start and finish temperatures.

4.3.5 Electrical Resistance Measurements:

Four-point resistance measurements were carried out inside a cryostat to determine the temperature-dependent electrical resistance of TiNiHf films constrained by Si and SiO_2/Si substrates. Quasi-stationary conditions guaranteed that influence of temperature change is negligible during measurement. For films of µm-thickness, probes contacting the film surface were used to connect to the setup, and for films of nm-thickness, films were connected by wire bonding. Phase transformations were determined by change in resistance with temperature and transformation temperatures were calculated using the tangent method.

4.3.6 X-Ray Diffraction (XRD):

The martensitic crystal structures and transformation temperatures of TiNiHf films on Si and SiO_2/Si substrates were confirmed using temperature-dependent X-ray diffraction (XRD) with a SmartLab 9 kW diffractometer (Rigaku, Japan), CuK_α radiation (λ = 1.5406 Å) and 2-D Hypix3000 detector operated in 1D mode. θ-2θ scans in the range of 10–100° were conducted with a step size of 0.02°, and a scan speed of 20°/min. A heating stage (AntonPaar DHS 1100, Germany) and cooling stage (AntonPaar DCS 350, Germany) was used in the temperature range between - 100 °C and 130 °C.

4.3.7 Cantilever Deflection Measurements:

Functional fatigue behavior in bi-directional actuators was characterized by measuring cantilever deflection as a function of temperature. The cantilever deflection measurement setup contains a laser, a mirror for directing the laser onto the surface, a position-sensitive detector (PSD) to detect deflection, a Peltier element for heating and cooling, and a thermocouple.

The actuator's stroke, D, of a cantilever can be calculated using Equation (1):

$$D = \frac{\Delta x l}{4a} \qquad \text{(Equation 1)}$$

where Δx corresponds to laser dislocation on the PSD surface, l is the length of the cantilever beam, a is the distance between the cantilever tip and PSD (a = 117 mm), and deflection is measured as volts on the PSD (V) which is converted to displacement (mm) by using a factor dx/dU = 0.794 mm/V. Each cantilever has a size of 3.5 mm x 20 mm, with a freestanding cantilever

length of 14 mm. The experiments were performed under vacuum (10^{-4} mbar) for each sample with a 10 °C/min heating/cooling rate within a temperature range of 30 °C to 170 °C.

4.3.8 Constitutive Modeling:

The model used to describe the shape memory alloy is in line with the model by *Sedlak et al.* [153], extended to the finite strain case with inhomogeneous temperature fields. The model details regarding numerical procedures are given in ref [154]. In contrast to other phenomenological finite strain shape memory alloy models, it makes use of a projection method to satisfy the inelastic volume preservation constraint [155, 156]. Further, we assume a multiplicative split of the deformation gradient in the form of $F = F^e F^i F^\theta$, where F^e is the elastic, F^i the inelastic and F^θ the thermal part of the deformation gradient F. Moreover, the volume fraction of martensite $\xi \in [0,1]$ and the inelastic right Cauchy-Green tensor $C^i = F^{iT} F^i$ are used as the internal variables of the model at hand. Additionally, the model is implemented into the framework of generalized standard materials [157], which ensures thermodynamic consistency when carefully choosing the potentials. This framework is then extended to non-constant temperatures θ using a variational formulation [158].

Thus, the total potential is given by $\pi = \dot{\psi} + \phi$, where $\dot{\psi}$ is the rate of the Helmholtz free energy density and ϕ is the dissipation potential. This potential is integrated over the system and minimized to solve the energy balance as well as the linear momentum balance in the bodies considered. We assume ψ to be the sum of an elastic, a chemical, and a hardening-type energy. The elastic energy is given by

$$\psi_e = \frac{\lambda(\xi)}{4}(J^{e2} - 1 - 2lnJ^e) + \frac{\mu(\xi)}{2}(tr(b^e) - 3 - 2lnJ^e) \qquad \text{(Equation 2)}$$

where $\lambda(\xi)$ and $\mu(\xi)$ are the Lamé parameters determined by a Reuss-like rule of mixture and J^e is the determinant of F^e. Further, the Kirchhoff stress τ is given by $\tau = 2b^e \partial \psi_e / \partial b^e$, where $b^e = F^e F^{eT}$ is the elastic left Cauchy-Green tensor. For the chemical energy, we assume a standard relationship [159, 160]:

$$\psi_c = u_0^A - \theta s_0^A + \xi(\theta - \theta_0)\Delta s^{AM} + c\left(\theta - \theta_0 - \theta ln\left(\frac{\theta}{\theta_0}\right)\right) \quad \text{(Equation 3)}$$

with the volume specific internal energy of the austenite phase u_0^A, the specific entropy of the austenite phase s_0^A, the specific heat capacity c, the difference in specific entropy of the austenite and martensite phase Δs^{AM}, the equilibrium temperature θ_0 and the absolute temperature θ. Since the inelastic strains vanish with $\xi \to 0$, the inelastic strain $E^i = \frac{1}{2}(C^i - I)$ is assumed to be given by $E^i = \xi E^t$, where E^t is a measure of the effective transformation strain in twinned regions. Additionally, the hardening-type energy is given by (compare to *Sedlak et al.* [153])

$$\psi_h = kE^{int}\,\frac{\xi E^{t2}}{1-E^{t4}} + H\left(tr\left(C^i\right) - 3\right), E^t = \sqrt{\frac{2}{3}}\frac{\|E^t\|}{k} \quad \text{(Equation 4)}$$

where k is the maximum transformation strain and E^{int} and H are hardening parameters. The thermal strains and jump in volume between martensite and austenite cells are modeled by $F^\theta = det\left(F^\theta\right)^{\frac{1}{3}} I = \left(1 + \varepsilon^\theta(\xi, \theta)\right) I$ with the thermal strain

$$\varepsilon^\theta = \xi\alpha_M\left(\theta - \theta_{refM}\right) + (1 - \xi)\alpha_A\left(\theta - \theta_{refA}\right) \quad \text{(Equation 5)}$$

where $\alpha_{A/M}$ are the coefficients of thermal expansion and $\theta_{refA/M}$ are the reference temperatures of austenite and martensite, respectively. To model the inelastic behavior, we define the dissipation potential, depending on the direction of the transformation, to be

$$\phi\left(\dot{\xi}, I, \xi\right) =$$

$$\begin{cases} \dot{\xi}\Delta s^{AM}\left((\theta_0 - M_s) + \xi\left(M_s - M_f\right)\right) + \sqrt{\frac{2}{3}}\sigma^{reo}\left\|D^i\right\| & \dot{\xi} \geq 0 \wedge tr\left(D^i\right) = 0 \\ \dot{\xi}\Delta s^{AM}\left(\left(\theta_0 - A_f\right) + \xi\left(A_f - A_s\right)\right) + \sqrt{\frac{2}{3}}\sigma^{reo}\left(\left\|\frac{\dot{\xi}}{\xi}\varepsilon^i\right\| + \left\|D^i - \frac{\dot{\xi}}{\xi}\varepsilon^i\right\|\right) & \dot{\xi} < 0 \wedge tr\left(D^i\right) = 0 \\ \infty & else \end{cases} \quad \text{(Eq. 6)}$$

where $D^i = sym\left(\dot{F}^i F^{i-1}\right)$ is the symmetric part of the inelastic 'velocity gradient', $\varepsilon^i = \frac{1}{2} ln\left(b^i\right)$ with $b^i = F^i F^{iT}$ and σ^{reo} the stress at which reorientation occurs. Furthermore, the heat conduction is assumed to follow Fourier's law with thermal conductivity κ. After further numerical treatment of the volume preservation constraint and differentiability problems of the dissipation potential, we solve the problem using an active set algorithm, which is embedded into the finite element analysis software FEAP [161]. The material parameters employed are given in the Appendix (**Table 4.5**, Chapter 4.7).

4.4 Results:

4.4.1 Functional Properties of Free-Standing TiNiHf Films

A. Thermal Fatigue Evaluation

The characteristic martensitic phase transformation temperatures, austenite start (A_s), austenite finish (A_f), martensite start (M_s), and martensite finish (M_f), and latent heat of transformation of forward (ΔH^{MA}) and reverse transformations (ΔH^{AM}) are determined by differential scanning calorimetry (DSC). **Figure 4.1(a)** shows the first DSC cycle of 21 µm, 10 µm, and 5 µm thick freestanding films depicting a reduction in all characteristic transformation temperatures, with decreasing film thickness. The thermal transformation temperatures, latent heat, and thermal hysteresis (ΔT) are given for all samples in **Table 4.1**. Only a minor influence on thermal hysteresis

is noticeable with a reduction in TiNiHf film thickness from 21 μm to 5 μm. However, the transition temperatures, latent heat of transformation, and thermal hysteresis width of TiNiHf films can also be slightly increased by annealing the films at a higher temperature as shown in our previous work [6].

Bi-directional and bistable SMA-based micro and nano actuators ideally should last for thousands of actuation cycles with little functional fatigue. The wide thermal hysteresis of ~ΔT = 57 °C indicates poor crystallographic compatibility between the martensite and austenite phase for the fabricated TiNiHf alloy [47]. **Figure 4.1(b)** shows functional fatigue of 5 μm thick film after 150 thermal cycles between 0 °C and 140 °C. A decrease in all characteristic transformation temperatures can be seen where the largest change occurs within the first ~20 cycles. The A_s, A_f, M_s and M_f temperatures continue to steadily decrease with every cycle without stabilization up to 150 cycles. A decrease in transition temperatures with thermal cycling is expected TiNi-based alloys due to the introduction of dislocations that compensate for the crystallographic compatibility between the martensite and austenite phases [47]. This fatigue behavior is observed in fabricated freestanding TiNiHf alloys indicated by a slight increase in ΔT with every cycle. Decreasing film thickness and thermal cycling lead to a significant reduction in the latent heat of both the forward and reverse transformation (ΔH^{AM}, ΔH^{MA}), which might be beneficial for SMA actuation [162].

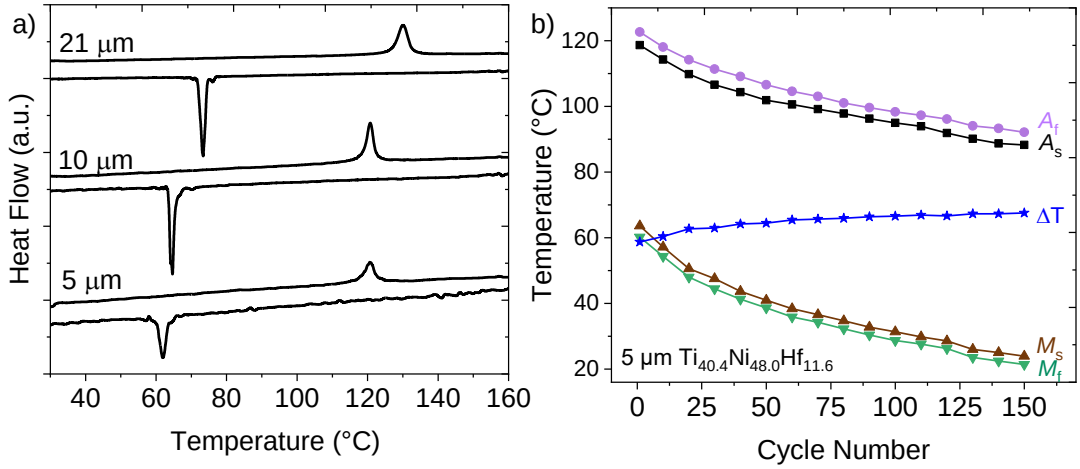

Figure 4.1: a) First DSC cycle showing $Ni_{47.7}Ti_{40.7}Hf_{11.6}$ freestanding films annealed at 635 °C – 5 min with decreasing film thickness from 21 µm to 5 µm. b) Change in characteristic transformation temperatures in 5 µm freestanding sample in first 150 thermal cycles.

Table 4.1: Thermal transformation properties of fabricated freestanding TiNiHf films, determined by DSC

Cycle #	Thickness /µm	A_s /°C	A_f /°C	ΔH^{MA} /J·g^{-1}	M_s /°C	M_f /°C	ΔH^{AM} /J·g^{-1}	ΔT /°C
1	21	127.3	132.6	17.5	71.9	74.5	21.9	56.8
1	10	119.0	122.2	14.7	65.3	63.5	19.5	56.2
1	5	118.7	122.4	9.2	63.6	60.2	15.8	58.7
50	5	101.9	106.6	15.0	41.0	38.6	17.0	64.4
90	5	96.3	99.6	12.1	32.8	30.4	16.9	66.4
120	5	91.9	96.1	10.3	28.6	26.2	15.9	66.6
140	5	88.7	93.3	11.4	25.0	22.4	14.2	66.9

B. Tensile Testing

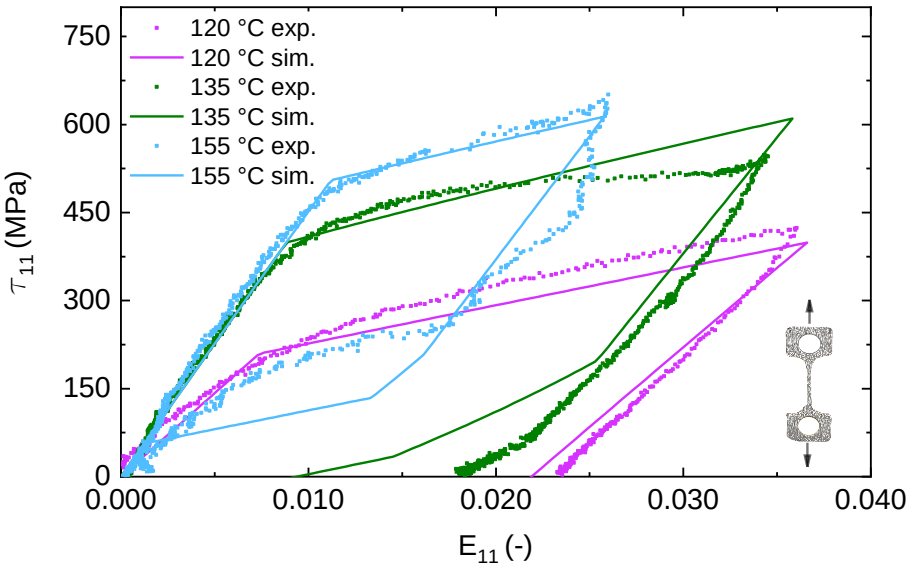

Figure 4.2: Experimental and simulated stress-strain curve of the investigated 21 µm thick TiNiHf freestanding films of dogbone geometry size of 500 µm × 4 mm (see inset). The tests are performed at three different ambient temperatures of 120 °C, 135 °C, and 155 °C with a strain rate of $1 \cdot 10^{-3}$ s^{-1}.

Figure 4.2 shows a comparison between experimental and simulated stress-strain characteristics of 21 µm thick freestanding TiNiHf films annealed at 635 °C – 5 min, structured into a dogbone geometry, at various temperatures in the phase transformation regime. The samples are investigated at three different ambient temperatures of 120 °C, 135 °C, and 155 °C at a constant strain rate of $1 \cdot 10^{-3}$ s^{-1}. Simulation results are fit to the experimental results to obtain mechanical parameters such as elastic modulus, maximum transformation strain, critical loading stress, and critical unloading stress values for the stress-induced martensitic transformation.

At 120 °C, one-way shape memory behavior is obtained upon loading/unloading the samples up to 3.5 % strain, indicating the material is in the martensite phase [163]. Reorientation of the martensite variants (detwinning) is suggested to introduce the slip of dislocations. The lack of a stress plateau in Ni-lean TiNiHf alloys is characterized by their low critical stress for slipping [47], strong work hardening behavior, and continuous yielding [144]. The open hysteresis loop with a residual strain of 2.4 % indicates the retained stress-induced martensite that is known to form when loading an SMA at a temperature $M_s < T < A_f$ [163]. At 135 °C, the critical stress (σ_{crit}) for phase transformation to martensite is about 430 MPa and a maximum tested strain of 3.4 %. The open hysteresis loop with a residual strain of 1.8 % indicates the sample is not fully transformed to the austenite phase by 135 °C. Upon loading and unloading at 155 °C, the critical stress for martensitic transformation shifts to 490 MPa, and the reverse transformation starts at 260 MPa. As a result, a superelastic behavior is obtained with recoverable strain up to 2.6 %. The simulated model fit for the 135 °C tensile test shows a certain discrepancy with experimental data. Upon unloading, the simulation model overestimates the recoverable strain from 1.8 % to 0.95 %. However, the superelastic and martensitic forward transformation behavior for all three test conditions is well described by the simulation model. The small discrepancy could be due to microstructural and grain size effects currently are not captured by the model. This includes the hardening effect that is responsible for the steep slope instead of a stress plateau for TiNiHf films.

4.4.2 Functional Properties of TiNiHf/Si and TiNiHf/SiO_2/Si Bimorphs

A. Electrical Resistance

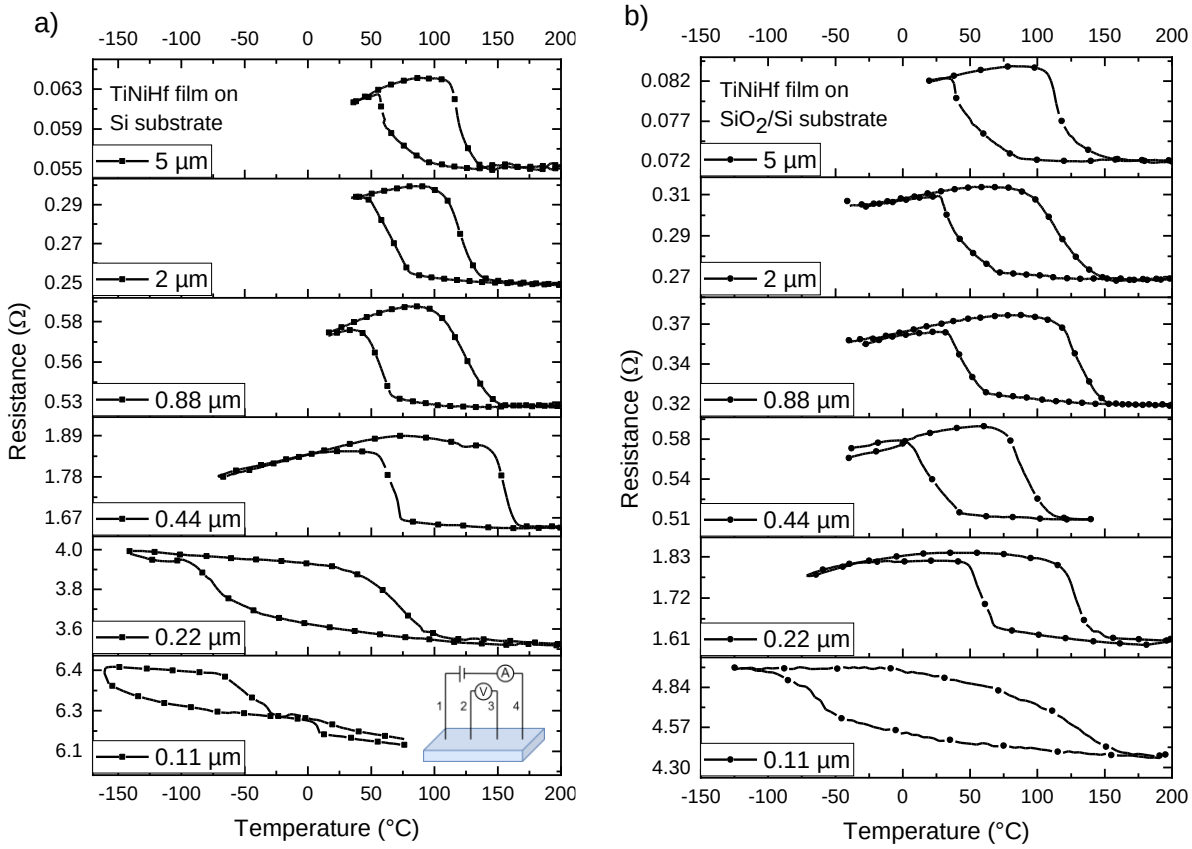

Figure 4.3: Comparison of resistance-temperature curves of TiNiHf films of different thicknesses on a) Si and b) SiO_2/Si substrates of 5 mm x 10 mm (see inset for the schematic), respectively. Hysteresis width gets significantly larger when films are below critical thickness, which are 0.44 µm for films on Si substrate and 0.22 µm for films on SiO_2/Si substrate.

The film thickness dependencies of the phase transformation properties of TiNiHf films on Si and SiO_2/Si substrates are investigated to understand their impact on bi-directional actuation performance. The transformation hysteresis curves are compared in **Figure 4.3** for all investigated thicknesses from 5 µm down to 0.11 µm on both substrates. Decreasing film thickness leads to a significant increase in resistance with a similar thermal hysteresis width until a critical film thickness is reached for very thin films.

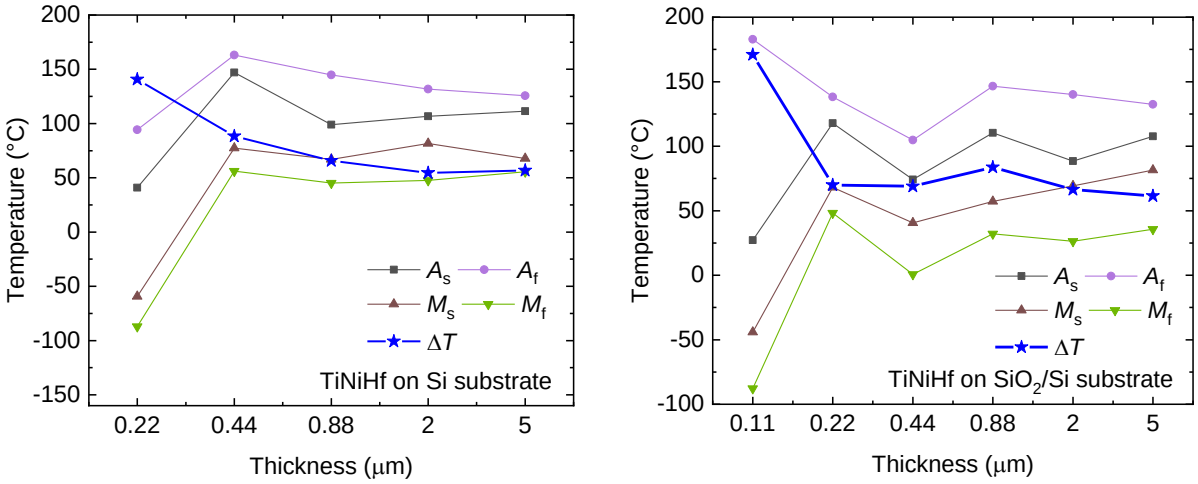

Figure 4.4: Transformation temperatures and calculated thermal hysteresis width ΔT of TiNiHf films with different thicknesses on a) Si substrate and b) SiO_2/Si substrate. Data is not shown for 0.1 μm-thin film on Si substrate, as transformation hysteresis is not fully seen in temperature range -160 °C to 200 °C. All films were annealed at the same condition 635°C – 5 min.

Figure 4.4 summarizes the corresponding thickness dependence of transformation temperatures and thermal hysteresis width ΔT of bimorph films. Data is not shown for the 0.11 μm film on Si substrate as electrical resistance measurements revealed only a partial phase transformation (M_s = -157.4 °C and A_f = -23.4 °C) when cooling the sample from room temperature to -160 °C. According to **Figure 4.4,** ΔT witnesses a dramatic increase when the film thickness is below 0.44 μm for films on Si substrate and below 0.22 μm for films on SiO_2/Si substrate, which appear to be critical thicknesses on the corresponding substrates. When the film thickness is below this critical value, the thermal hysteresis shifts to a lower temperature range and the hysteresis width nearly doubles. In contrast, when the film thickness is larger than the critical thickness, the thermal hysteresis width and transformation temperatures show only minor variations.

B. Structural Properties

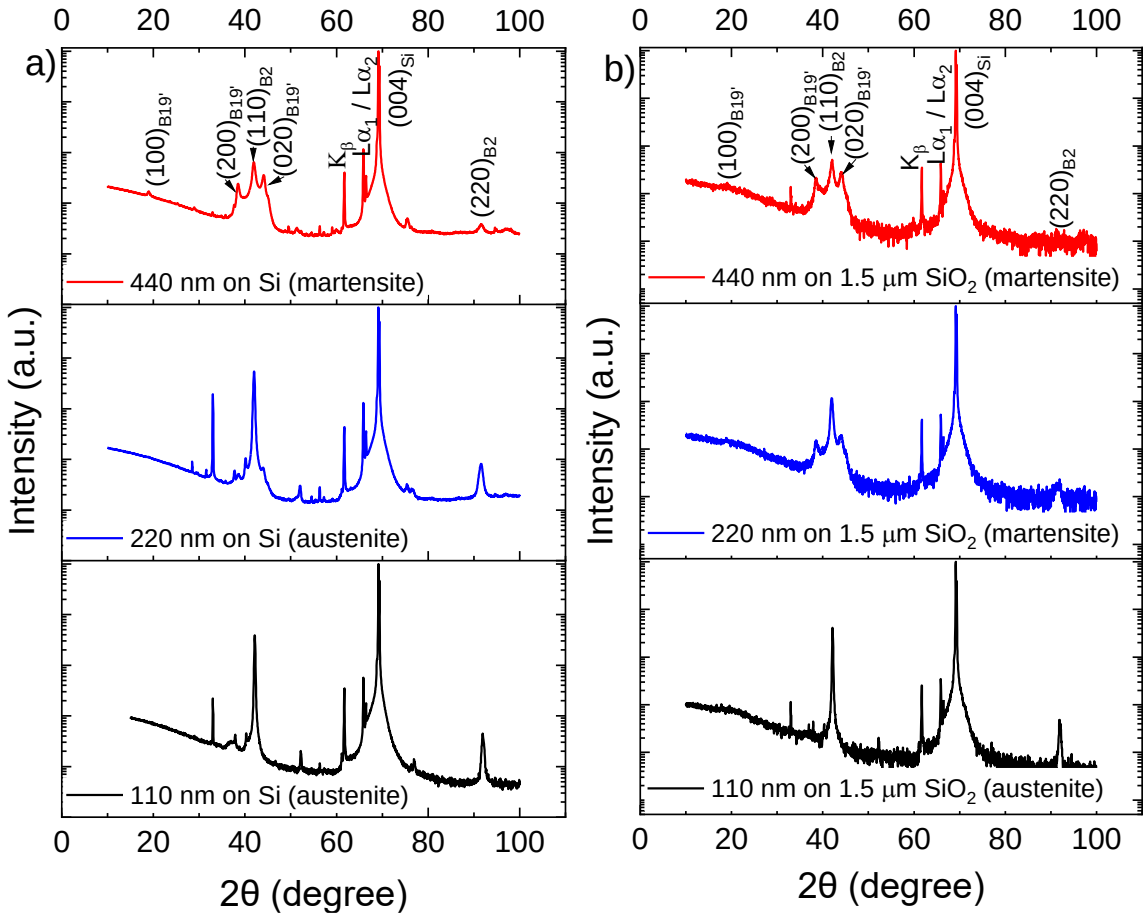

Figure 4.5: XRD results at 30 °C for 110 nm, 220 nm, and 440 nm TiNiHf films on a) Si substrates and b) on 1.5μm SiO_2/Si substrates. Samples were 20 mm x 20 mm in size.

TiNiHf is known to undergo a solid-to-solid phase transformation from a low-symmetry, low-temperature, martensite phase (monoclinic, B19') to a high-symmetry, high-temperature, austenite phase (cubic, B2). The crystal structures of all TiNiHf films (between 110 nm and 5 μm) on Si and SiO_2 substrates were evaluated at room temperature with X-ray diffraction (XRD). **Figure 4.5** shows XRD results at 30 °C for 110 nm, 220 nm, and 440 nm TiNiHf films on both Si and 1.5 μm SiO_2/Si substrates. The preferred orientations of martensite and (110) austenite peaks

are labeled. Two dominant peaks arise for the martensite phase at 40° for the (002) B19' phase, and 44° for the (020) B19' phase. The dominant peaks for the austenite phase are located at 42° for the (110) B2 phase and 91° for the (220) B2 phase. The absence (or a weak signal) of these two austenite peaks is an indication that the sample is in the martensite phase at room temperature. The large signal at 69° is the peak related to the (001) Si substrates. There were a handful of unidentifiable secondary phase peaks for TiNiHf films on Si substrates that were not observed for TiNiHf films on SiO_2/Si substrates. The additional peaks could be due to a $(Ti,Hf)_2Ni$ phase that occurs when using Ti-rich TiNi film compositions [47, 135]. For a more precise study on the precipitate phases, additional TEM measurements are necessary, which are out of the scope of the current study.

To realize many applications, the main criteria for selecting the film and film composite for martensitic phase transformation has to be above room temperature transformation. **Figure 4.5(a)** shows that 110 nm and 220 nm TiNiHf films on Si substrates are in the austenite phase at room temperature. However, **Figure 4.5(b)** for 220 nm films on SiO_2/Si buffer layers, XRD shows the SMA is composed of martensite B19' phase with some residual austenite at room temperature. XRD results indicate the minimum film thickness required to obtain a transformation above room temperature is ~220 nm on SiO_2/Si substrates and ~440 nm on Si substrates. This confirms both, the dramatic film thickness effect below critical film thicknesses as well as the substrate dependence of this film thickness effect observed in electrical resistance measurements. As shown in the Appendix (**FigureA4.1**, Chapter 4.7), all TiNiHf film thicknesses above the critical thickness value on SiO_2/Si substrates transform from the martensite phase at 30 °C, to the austenite phase upon heating to 110 °C. 220 nm and 440 nm films SiO_2/ Si substrates were fully transformed to the austenite phase by 110 °C. Films with a thickness greater than 880 nm on

SiO_2/Si substrates still showed weak (200) and (020) martensite peaks indicating that these samples are still partially martensite at 110 °C.

Temperature-dependent X-ray diffraction measurements were used to determine the transformation temperatures of TiNiHf films with thicknesses of 110 nm, 220 nm, 440 nm, 880 nm, and 5 μm on Si substrates and a 440 nm thick TiNiHf film on 1.5 μm SiO_2/Si substrates. The samples were heated and cooled in 5 °C increments between 30 °C and 130 °C at a heating rate of 10 °C/s. By monitoring the change in peak intensity of the B2 austenite peaks at 42° and 91° and using a Rietveld refinement on the (110) B2 cubic austenite phase, it was possible to determine the SMAs transition temperatures [164]. The results of the transformation temperatures for all tested films are given in **Table 4.2**. 110 nm films on SiO_2/Si substrates were in the cubic austenite phase, with no transformation taking place in the temperature range between 30–130 °C. 220 nm films on Si substrates were also found to be in the cubic austenite phase at 30 °C with no transformations taking place between 30 °C and 130 °C is given in the Appendix **(Figure A4.2,** Section 4.7). 440 nm TiNiHf films on Si substrates were found martensite at room temperature displayed an above room temperature phase transformation with A_s = 95.4 °C and A_f = 108.7 °C, shown in the Appendix (**FigureA4.3,** Section 4.7). There was not a significant change in transformation temperatures for 440 nm on Si versus 440 nm films on 1.5 μm SiO_2/Si substrates. Scanning electron microscopy cross-sectional images of different TiNiHf film thicknesses (5 μm, 2 μm, 880 nm, and 440 nm) on Si substrates are shown in the Appendix, (**FigureA4.4**, Section 4.7)**.**

Table 4.2: Transition temperatures of TiNiHf films on Si substrates and SiO_2/Si substrates for different thicknesses determined by XRD

Substrate	Thickness /µm	A_s /°C	A_f/°C	M_s/°C	M_f/°C	ΔT/°C
Si substrate	5	88.2	114.2	72.7	50.4	39.6
	0.88	95.3	110.1	69.3	56.9	39.6
	0.44	95.4	108.7	67.9	56.5	39.9
	0.22	No transformation between 30 °C and 130 °C				
	0.11	No transformation between -100 °C and 130 °C				
1.5 µm SiO_2/Si substrate	0.44	92.9	108.3	68.2	50.9	41.1
	0.11	No transformation between 30 °C and 130 °C				

Temperature-dependent XRD data was used to estimate the coefficient of thermal expansion (CTE) for the austenite phase of the $Ti_{40.4}Ni_{48}Hf_{11.6}$ alloy by monitoring the change in the cubic lattice parameter while cooling the SMA over a temperature range of 120 °C to 85 °C [165]. The CTE of the austenite phase (α_A) was calculated to be $30 \times 10^{-6}K^{-1} \pm 5 \times 10^{-6}K^{-1}$ from XRD measurements. This value falls between the austenite CTEs reported for binary NiTi ($\alpha_A = 13 \times 10^{-6}K^{-1}$) [166] and for a $Ti_{29.7}Ni_{50.3}Hf_{20}$ alloy ($\alpha_A = 49.6 \times 10^{-6}K^{-1} \pm 3.4 \times 10^{-6}K^{-1}$) [140]. For computational simulations the calculated value from XRD data is used ($\alpha_A = 30 \times 10^{-6}K^{-1}$), and for simplicity, the CTE value for martensite is estimated to be half the value of austenite ($\alpha_M = 15 \times 10^{-6}K^{-1}$).

4.4.3 Bi-directional Actuation Based on TiNiHf/SiO_2/Si Bimorph Film Composites Cantilever Deflection Measurements

Actuation in SMA/Si bimorph cantilevers arises from the combined shape memory effect and CTE difference between bimorph layers. The different stress states in the bimorph cantilever that lead to desirable deflection arise when heating the composite to temperatures above A_f and cooling the composite below M_f. The maximum actuation stroke is determined by the y-deflection obtained between the martensite and austenite phases using CDM.

Figure 4.6(a) shows 145 cycles of deflection for 0.88 μm TiNiHf/100 nm SiO_2/300 μm Si cantilever composite. The transition temperatures, thermal hysteresis, and maximum stroke upon thermal cycling are given in **Table 4.3**. A decrease in transformation temperatures and a slight decrease in the actuation stroke is observed with increasing cycles. **Figure 4.6(b)** shows the change in characteristic transformation temperatures as a function of thermal cycles for 0.88 μm TiNiHf/100 nm SiO_2/300 μm Si bi-directional actuator. The thermal-mechanical hysteresis stabilized after ~120 cycles, with a minor shift in transformation temperatures between cycles 120–145. After ~60 cycles, the M_f temperature dropped below the minimum test temperature of 30 °C, therefore, the material was not fully transformed. The M_f temperature is marked with a green open symbol in **Figure 4.6(c)** to indicate M_f < 30 °C. Very small reduction in maximum actuation stroke from 32 μm to 31.5 μm within the first 40 cycles (i.e., an indication of functional fatigue) is observed which then stabilized in the subsequent cycles.

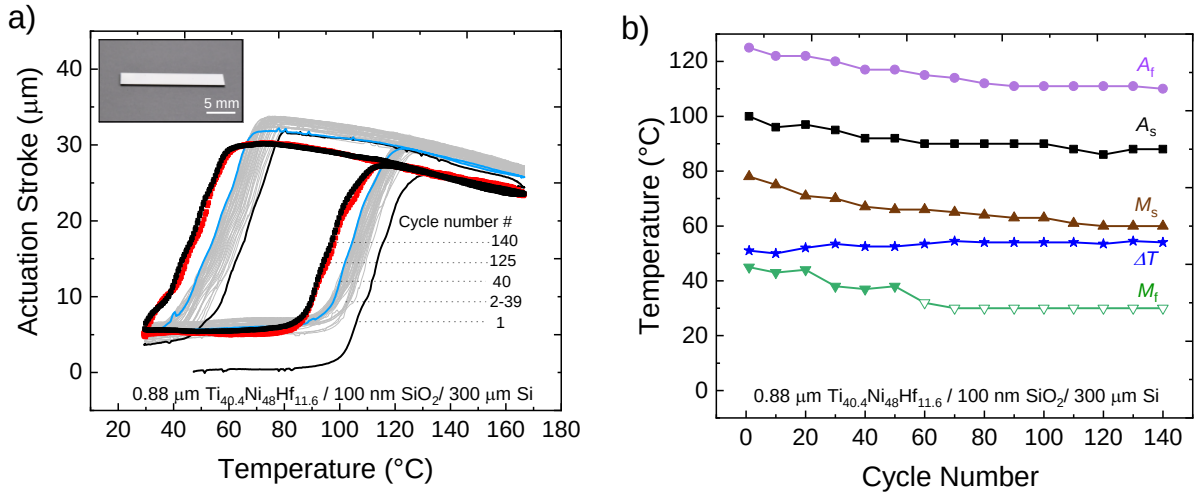

Figure 4.6: a) Deflection versus temperature measurements of bi-directional TiNiHf/SiO_2/Si actuators with TiNiHf film thicknesses of 0.88 µm on 100 nm buffer layer of SiO_2 on 300 µm Si substrates (see inset for the sample picture). b) Influence of functional fatigue on transition temperatures for the 0.88 µm TiNiHf/SiO_2/Si composite. Cantilevers were 3.5 mm x 20 mm in size, with a freestanding cantilever length of 14 mm during measurement.

Table 4.3: Influence of functional fatigue on bi-directional stroke and characteristic transformation temperatures of different TiNiHf thicknesses on 100 nm SiO_2/Si substrates

Cycle #	**Thickness /µm**	A_s /°C	A_f/°C	M_s/°C	M_f/°C	ΔT/°C	**Stroke /µm**
1	2	110	134	85	59	50	39
40	2	101	127	74	45	54.5	35
1	0.88	100	125	78	45	51	32
40	0.88	92	117	67	37	52.5	31.5
140	0.88	88	110	60	<30	54	31.5

4.4.4 Bistable Actuation Based on PMMA/TiNiHf /Si Trimorph Film Composites

A. Bistable Actuation Principle

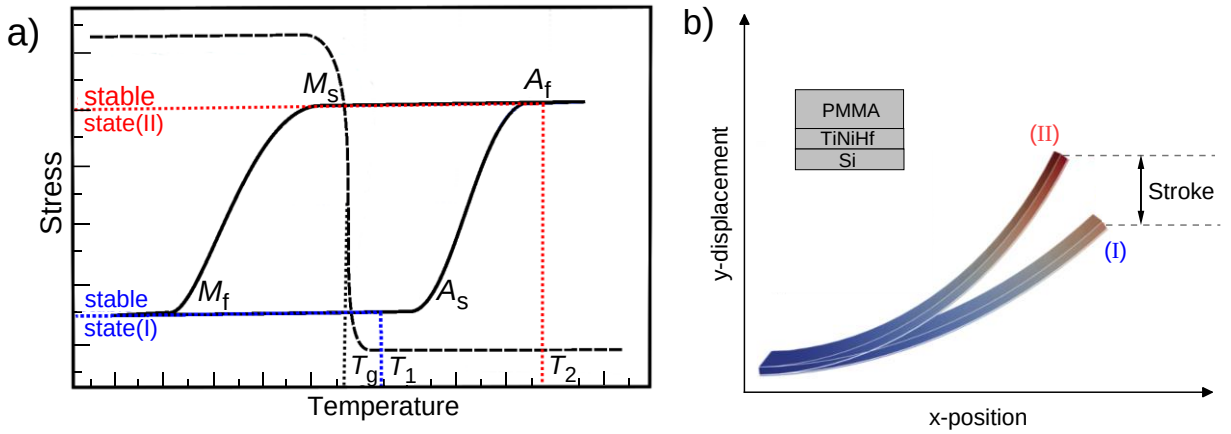

Figure 4.7: a) Schematic of interlaced polymer and shape memory alloy hysteresis, enabling bistability. b) Superimposed stable states (I) and (II) for comparison. The cross-section of the trimorph layers (PMMA/TiNiHf/Si) is sketched.

The unique properties of TiNiHf/Si bimorph films of large hysteresis and an A_f temperature larger than 105 °C opens the opportunity for the design of bistable actuation using a polymer layer on TiNiHf/Si composite. As depicted in the schematic in **Figure 4.7(a)**, SMA/Si bimorph structures can become bistable if combined with a polymer with matching glass transition temperature (T_g). That means, the glass transition temperature of the polymer is required to fall within the thermal hysteresis of the SMA ($M_s < T_g < A_s$) [22]. Assume the composite is in stable state I as shown in **Figure 4.7(b).** In order to switch to stable state II, the composite is heated above austenite finish temperature ($T_g < A_f < T_2$), allowing the polymer to soften and adapt to the deflected shape of the composite. Upon cooling below T_g, the polymer will become hard and, thereby, fixes the deflected shape that corresponds to stable state II. In order to recover stable state

I, the composite is heated to an intermediate temperature T_1 ($T_g < T_1 < A_s$), the polymer becomes soft again and adapts to the initial shape in the martensite phase which will be fixed upon cooling to room temperature. The fixation effect will be effective if the thickness of the polymer is large enough.

Here, we use PMMA as the polymer in a PMMA/TiNiHf/Si trimorph composite. PMMA is a standard resist material in various lithography methods such as X-ray lithography, deep UV-lithography, and E-beam lithography techniques [6, 167–169]. The glass transition temperature of PMMA is 105℃ which fulfills the criteria for bistability.

B. Polymer and Si Model

Since the PMMA polymer does not exhibit shape memory effects, the polymer is modeled as a passive material. This is done by using a thermally coupled viscoelastic Maxwell model for finite strains [170], where the viscosity is 10^7 MPa · s at low temperatures below $T_g = 105$ ℃ and 1 MPa · s at high temperatures. Thus, the polymer is soft above T_g, while still being stiff at colder temperatures. For simplicity, the CTE ($70 \times 10^{-6} K^{-1}$) [171], Young's modulus (500 MPa), and Poisson's ratio (0.4) of the PMMA polymer are held constant in simulations. The Si layer is modeled using a thermally coupled Neo-Hookean elastic model with Young's modulus of 130 GPa and Poisson's ratio being equal to 0.278 [172]. The CTE of Si is $2.6 \times 10^{-6} K^{-1}$ [138]. The SiO_2 buffer layer is neglected in simulations as it is not expected to influence the mechanical properties of the composite.

C. Actuator Geometry and Boundary Conditions

The modeled actuator has a length of 1 mm and a width of 100 µm. The Si and SMA films have a thickness of 2 µm and 1 µm, respectively. The geometry is discretized by 20 elements over its length and 6 over its width, whereas each layer of material is discretized by 4 elements over the thickness. On the left side, it is clamped, i.e., the displacements on the left side are constrained to be zero. Additionally, at the top and bottom of the thin film, a Robin boundary condition with a convective heat transfer coefficient of $(70\ W\ m^{-2}K^{-1})$ [173] is used to model heat convection with the surrounding air, which has a temperature of 20 °C. Furthermore, Joule heating is realized through a heat source term in the TiNiHf. The actuator model is shown in **Figure 4.7(b)**.

D. Optimization of Polymer Thickness

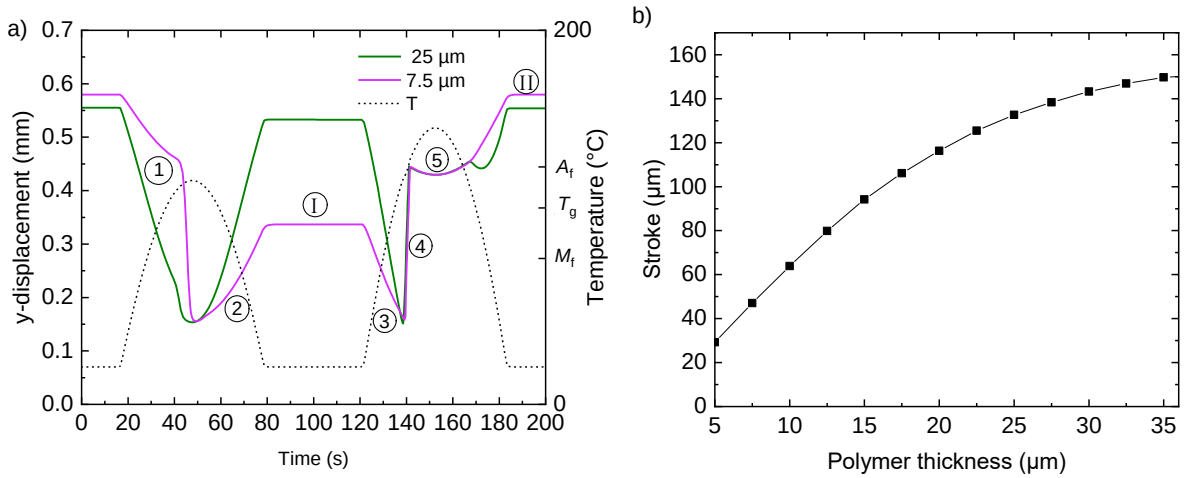

Figure 4.8: a) Demonstration of bistable actuation of PMMA/TiNiHf/Si through simulation assuming a T_g of 105 °C. b) FEM simulation of maximum bistable stroke versus polymer thickness for a cantilever consisting of a PMMA/TiNiHf/Si trimorph composite with TiNiHf and Si layer thicknesses of 1 and 2 µm, respectively. The cantilever length L and width w are 1 mm and 100 µm, respectively.

The actuator's maximum bistable stroke is strongly dependent on the polymer layer thickness. If the layer is too thin, it is not able to hold the austenite-related shape at room temperature. If the polymer layer is too thick, it hampers the stroke and limits the actuation speed as well as power consumption. Additionally, larger body forces and less freedom for the thermal hysteresis of the shape memory alloy limit the design space of the actuator. Therefore, we optimize the polymer geometry by simulating several thicknesses. For clarity, only two polymer thicknesses of this sweep are shown in **Figure 4.8(a)**, where the achieved vertical displacement and the temperature in the middle of the SMA at the end of the beam are plotted over time. In the beginning, we start with the actuator at room temperature, which is held by the polymer in stable state (I). Subsequently, the actuator undergoes a low heat cycle (1-2) in **Figure 4.8(a),** in which the polymer softens and releases the stress, which results in the flattened, stable state (I). After that, the actuator is heated above A_f (3-4). Next, it is cooled down to room temperature again (5), at which it returns to stable state (II) again.

When reaching M_f, depending on the polymer thickness, it can hold the shape (e.g., for 25 µm) or release most of the actuation (e.g., for 7.5 µm, shown in **Figure 4.8(a)**). Additionally, since the area moment of inertia depends in a cubic manner on the polymer layer thickness, any thinner layers result in a less achievable stroke. The influence of the polymer layer onto the achievable bistable stroke is depicted in **Figure 4.8(b)**, where the difference between the vertical displacement of stable states (I) and (II) are compared. Furthermore, favorable thickness combinations for smaller actuator geometries and stack sizes are listed in **Table 4.4**. The maximum relative bistable strokes (*Δy/L)* show a scaling-dependent decrease when reducing the lateral dimensions $L \times w$ from 1000×100 µm^2 down to 20×2 µm^2. Yet, even for the smallest bistable device, a considerable bistable stroke of 4% is expected, which is of special interest for actuator

applications at ultra-small scales. Because the model at hand does not inherit any size effects, further model refinement might be required considering additional effects such as grain size, oxidation, compositional or other influences affecting the actuation behavior. Furthermore, the T_g of PMMA is dependent on parameters such as film thickness and polymer molecular weight. Additionally, both the T_g and CTE are dependent on the interfacial energy between the polymer film and substrate and the exposure dose used during structuring [167–169]. These processing and scaling effects are not captured by the model and must be taken into account when designing bistable actuators with PMMA/TiNiHf/Si trimorph composites.

Table 4.4: Simulated stroke of downsized trimorph actuator geometries

Length *L*	**Width *w***	**Layer thicknesses *t***			**Bistable stroke *Δy***	**Relative bistable stroke *Δy/L***
		Si	SMA	Polymer		
1 mm	100 µm	2 µm	1 µm	20 µm	116 µm	12 %
100 µm	10 µm	2 µm	1 µm	20 µm	4.4 µm	4.4 %
20 µm	2 µm	0.4 µm	0.2 µm	4 µm	0.8 µm	4 %

4.5 Discussion:

The shape memory properties of TiNiHf/SiO_2/Si bimorph composites were characterized experimentally for use as micro and nano bi-directional actuators. Controlling functional fatigue characteristics upon thermal cycling in Ni-lean TiNiHf is pivotal in the development of bi-directional actuators. DSC and CDM results showed that the transition temperatures of fabricated TiNiHf freestanding films and TiNiHf/SiO_2/Si bimorph composites decrease with thermal cycling. The change in transition temperatures with cycling is reduced for TiNiHf films bound to a SiO_2/Si substrate compared to the functional fatigue DSC results reported for freestanding films from **Table 4.1**. An average reduction in transition temperatures of 12 °C – 18°C is obtained for 0.88 μm TiNiHf/SiO_2/Si composites after 140 cycles compared to an average reduction in transition temperatures of 29 °C – 38 °C for 5 μm freestanding TiNiHf films after 140 cycles. Additionally, XRD and CDM also show thermal hysteresis width is also reduced for TiNiHf films constrained by SiO_2 and Si substrates compared to freestanding films of similar thicknesses. This might imply an improvement in the compatibility of the austenite and martensite phases for films constrained by a substrate. The Si and SiO_2/Si substrates cause an inhomogeneous stress profile at the film-substrate interface, which may affect phase transformation temperatures as it poses an additional energy barrier for the formation of martensite upon cooling [7].

Based on the analysis of our experimental results, we can infer a pronounced substrate influence as well as a dramatic film thickness effect below a substrate-dependent critical film thickness on the phase transformation properties of TiNiHf films. Freestanding TiNiHf films show a thickness-dependent decrease of all characteristic transformation temperatures of ~10 °C when reducing thickness from 21 μm to 5 μm. Similarly, decreasing the SMA's thickness was found to

decrease the martensitic transformation temperatures for SMA wires (e.g. NiMnGa[174]), freestanding films (e.g. TiNiCu [150], NiTi [148, 149]), and sputtered bimorph systems (e.g. NiMnGa/Si [7], NiTi/Si [175], NiTi/Pt [10], Ti_2NiCu/Pt [176]). This thickness effect can also be seen for TiNiHf with decreasing film thickness from 5 µm down to 110 nm constrained on Si and SiO_2/Si substrates. There is a critical thickness of TiNiHf films on both Si and SiO_2/Si substrates, below which the thermal hysteresis width increases significantly. Temperature-dependent electrical resistance measurements and X-ray diffraction measurements are in agreement that these values are between 110 nm and 220 nm for films on SiO_2/Si substrates and between 220 nm and 440 nm for films on Si substrates.

This shows evidence that the interface between the substrate and TiNiHf film plays an important role in the phase transformation and is more pronounced below a critical thickness. The existence of the observed critical thickness values could also be ascribed to a change in the composition of the TiNiHf film due to diffusion at the surface and interface of the substrate during the annealing process. One explanation of the change is a TiO_x oxidation layer on the surface of the SMA film [149, 175], which is claimed to affect films with a thickness below 1 µm [149, 175]. The oxidation layer will create a Ti-lean zone beneath, which is much thicker than the oxidation layer, changing the composition of the film. The effect of the SiO_2 buffer layer on the change of the critical thickness to lower values might be attributed to the effect of diffusion as well. *Jarrige et al.* [175] propose that for binary NiTi systems, there is an additional TiO_x oxidation layer between the film and SiO_2/Si substrate and this layer can hinder the diffusion of Ni and Si atoms between the film and the substrate, as was observed for films annealed on Si substrates. Furthermore, the stress at the TiNiHf/Si interface might be reduced due to stress release by the intermediate SiOx layer, which affects phase transformation at small SMA layer thicknesses.

These considerations help to understand that the critical thickness of TiNiHf films on SiO_2/Si substrate could be smaller than that on Si substrate. However, further investigations on the layer sequence (addition of buffer layers and diffusion barriers like Si_3N_4 or Ta) of bimorph sample sections are needed for better understanding.

The transition temperatures deduced from different experimental methods of DSC, XRD, electrical resistance and bi-directional deflection reveal systematic deviations. The different length scales and different loading conditions may cause major differences. While XRD probes undergo phase transformation at the local scale, electrical resistance reveals average values of the whole test specimen. Bi-directional bending reflects the non-uniform stress profiles during beam bending, which is absent in DSC. Another difference is ascribed to the different time scales of temperature cycling in the phase transformation regime. In particular, electrical resistance measurements have been performed by providing sufficient waiting time between data points to enable quasi-stationary equilibrium conditions, while DSC experiments have been conducted using a fixed heating and cooling rate. However, these details are not the focus of this investigation. Conclusions are drawn based on the dependencies observed by each experimental method independently, while direct comparisons are avoided.

The experimental results shown in this work envisage a possible route for developing bistable actuators using an additional polymer layer to TiNiHf/Si bimorphs. The biggest challenge in experimentally realizing such bistable devices is tailoring transformation temperatures of TiNiHf to match the T_g of PMMA. Simulations incorporated the experimental results on TiNiHf phase transformation properties accounting for substrate influence and film thickness effects that arise when downscaling to nanofilms. Simulation results indicated that trimorph PMMA/TiNiHf/Si film composites exhibit large bistable actuation with scaling-dependent bistable

stroke per length ($\Delta y/L$). The simulation results should be considered as an outlook and guideline for future experimental work.

4.6 Conclusions:

For the investigated chemical composition of $Ti_{40.4}Ni_{48}Hf_{11.6}$ and optimized annealing conditions of 635 °C – 5 min, it is found that decreasing the layer thickness of TiNiHf in bimorph composites decreases the phase transformation temperatures. A large reduction of M_s/A_s by more than 100 °C is observed when TiNiHf film thickness drops below a critical thickness. The onset of the film thickness effect depends on the substrate. For Si substrates, critical thickness occurs between 440 and 220 nm, while for 1.5 μm SiO_2 buffer/Si substrate it occurs between 220 and 110 nm. Functional fatigue was improved for TiNiHf films in bi-directional TiNiHf/SiO_2/Si composites as compared to freestanding TiNiHf films. The fabricated bi-directional actuator demonstrated a stable actuation stroke after 40 thermal cycles, and thermal stability after 125 cycles. Freestanding films on the other hand achieved was not stabilized in the first 150 thermal cycles. Tailoring the substrate and film properties of TiNiHf films above room temperature leads to the possibility to use these films for advanced nano- or micro-actuation. To further investigate the utility of these films for the actuation, simulations were carried out by adding an additional PMMA layer to show that with this material system, bistable actuation can be achieved at nanoscales. Once functional fatigue is controlled in sputtered TiNiHf/SiO_2/Si film composites, these results show they are promising materials for nanoscale actuation to enable novel applications in nanomechanics and photonics.

Acknowledgments:

This research has received funding from the German Research Foundation (DFG) within the priority program “SPP2206–Cooperative Multistage Multistable Microactuator Systems”. S.M. Curtis gratefully acknowledges support from the National Science Foundation Graduate Research Fellowship under Grant No. DGE 1840340. We acknowledge Kaiju Lu at the Institute for Applied Materials (KIT-IAM) for access to temperature-dependent tensile test experiments. The authors would like to thank Afrin Shara for her assistance with fabrication and thermal characterization.

4.7 Appendix:

Table 4.5: Materials parameters used in constitutive modeling

λ_{A}	58028 MPa	Tensile Tests / $\nu = 0.39$ from [177]
λ_{M}	36385 MPa	Tensile Tests / $\nu = 0.39$ from [177]
μ_{A}	16366 MPa	Tensile Tests / $\nu = 0.39$ from [177]
μ_{M}	10262 MPa	Tensile Tests / $\nu = 0.39$ from [177]
θ_0	119 °C	Tensile tests/DSC
M_{s}	118 °C	Tensile tests/DSC
M_{f}	78°C	Tensile tests/DSC
A_{s}	120 °C	Tensile tests/DSC
A_{f}	127 °C	Tensile tests/DSC
σ^{reo}	210 MPa	Tensile tests
Δs_{AM}	0.74 MPa/K	Tensile tests/DSC
E^{int}	190 MPa	Tensile tests
k	0.25	Tensile tests
α_{M}	$15 \cdot 10^{-6}$ /K	Estimated as $\alpha_{\mathrm{A}}/2$
α_{A}	$30 \cdot 10^{-6}$ /K	XRD measurements
c	2.9 kJ mm^{-3} /K	[178]
κ	8.6 W/m	[178]
θ_{refM}	588.28 °C	Calculated from ΔV [179], see also [154]
θ_{refA}	500 °C	Ref. Temperature

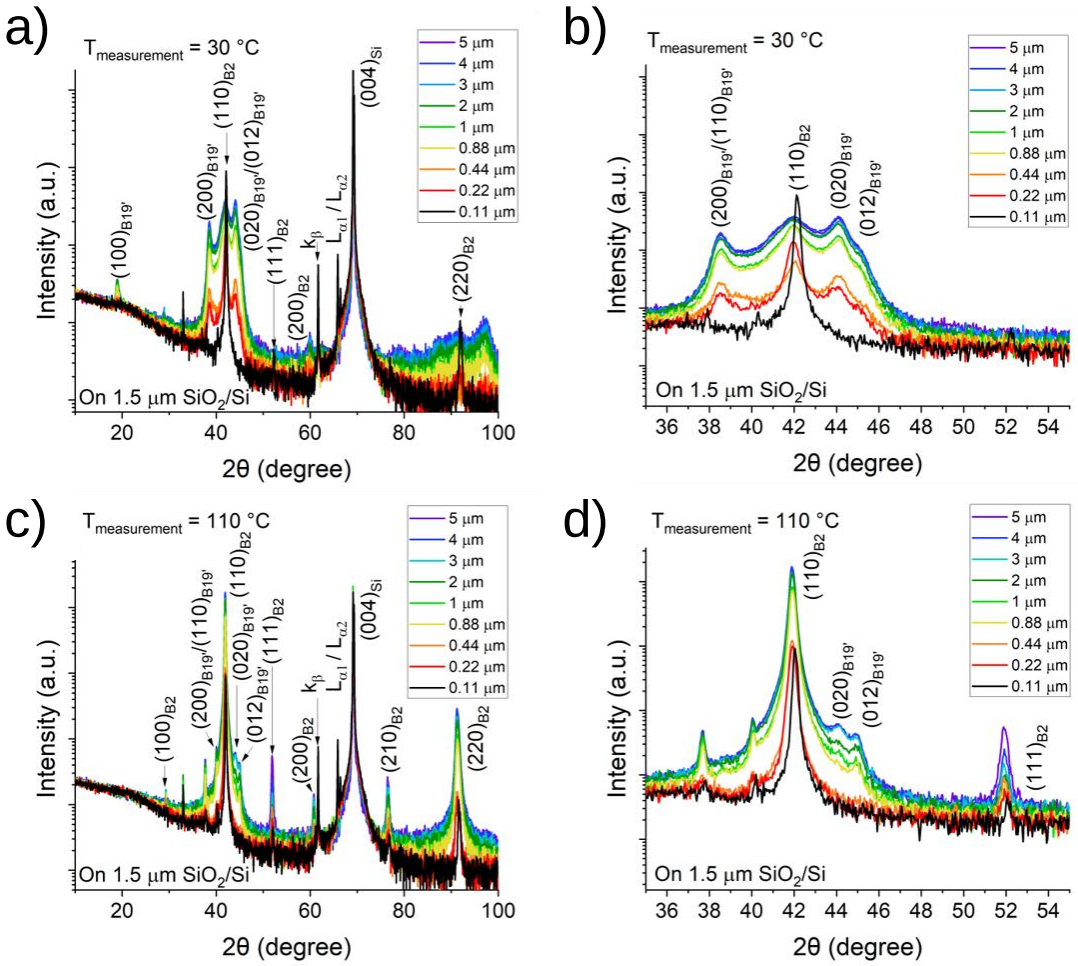

Figure A4.1: XRD scans demonstrating the phase transformation in $Ti_{40.4}Ni_{48}Hf_{11.6}$ films thicknesses between 5 μm – 0.11 μm deposited on 1.5 μm SiO_2/Si substrates and annealed at 635 °C – 5 min. a) θ-2θ scan from 10 ° - 100 °, demonstrating all films above the critical thickness value (0.22 μm) are in the martensite phase (B19') at room temperature ($T_{measurement}$ = 30 °C). b) Enlargement of θ-2θ range between 35 ° – 55 ° showing that the 0.11 μm film was in the austenite phase (B2) at room temperature. The 0.22 μm and 0.44 μm samples display strong residual austenite at room temperature. c) θ-2θ scan from 10° – 100° showing all films are in the austenite phase at $T_{measurement}$ = 110 °C. d) Enlargement of θ-2θ range between 35 ° – 55 ° showing that films with a thickness of 0.88 μm or greater show residual martensite phase at 110 °C. This implies that these samples are slightly below their A_f temperature at 110 °C.

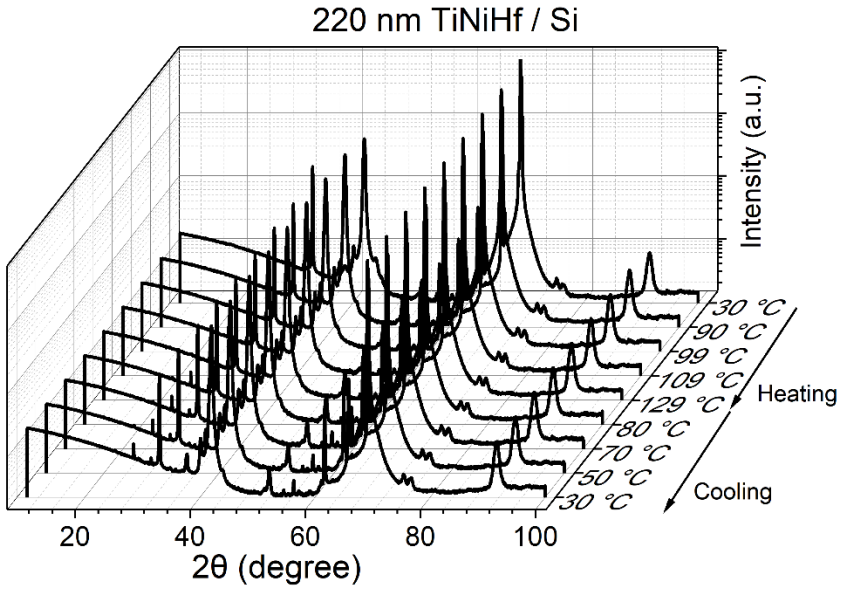

Figure A4.2: Selected temperature-dependent XRD scans showing no phase transformation occurs between B19' ↔ B2 for a 220 nm TiNiHf film on a Si substrate when heating and cooling in range between 30 °C and 130 °C.

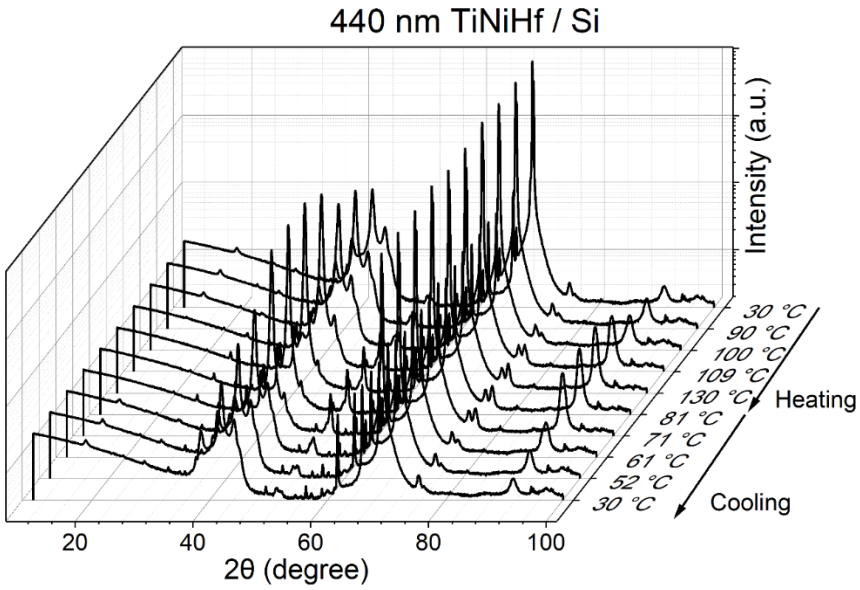

Figure A4.3: Selected temperature-dependent XRD scans displaying the phase transformation between B19' ↔ B2 when heating and cooling a 440 nm TiNiHf film on a Si substrate between 30 °C – 130 °C. The transformation temperatures for this sample were determined to be A_s = 95.4 °C, A_f = 108.7 °C, M_s = 67.9 °C, M_f = 56.5 °C, ΔT = 39.9 °C by this XRD measurement.

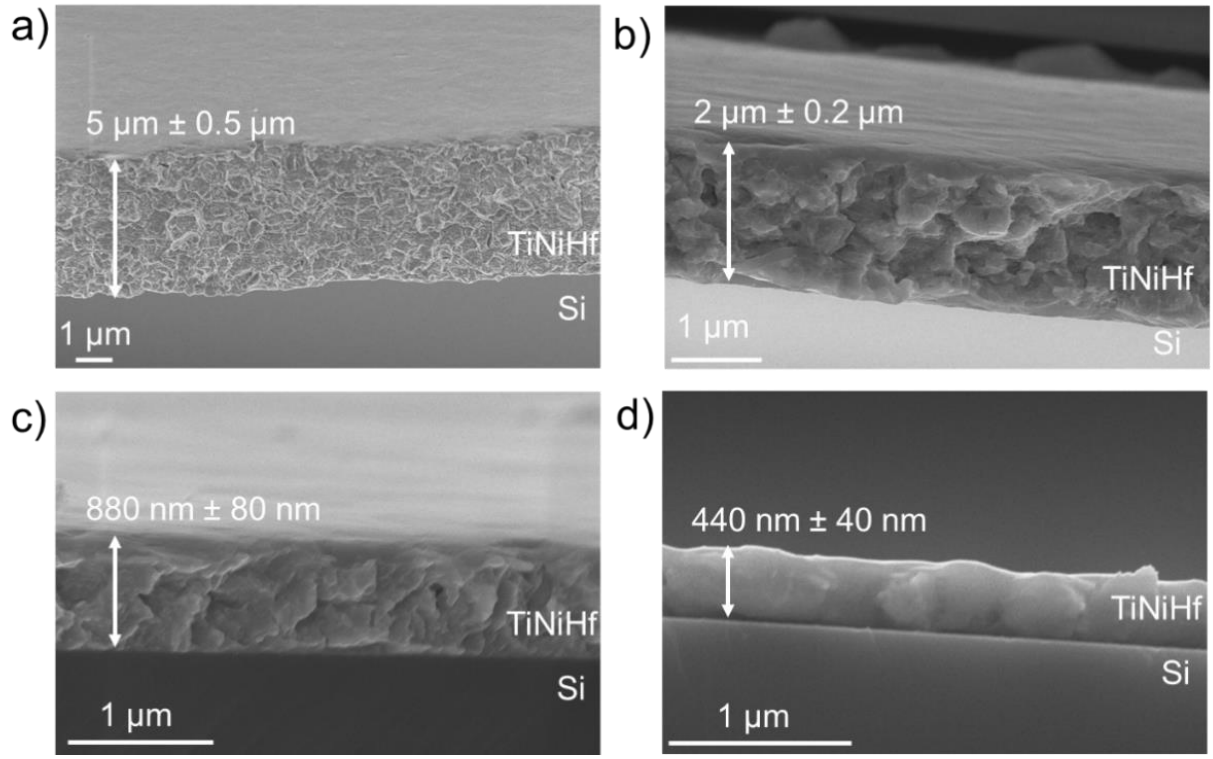

Figure A4.4: Scanning electron microscopy images showing the cross-section of TiNiHf films on Si substrates. TiNiHf film thickness on Si is a) 5 µm ± 0.5 µm, b) 2 µm ± 0.2 µm, c) 880 nm ± 80 nm, and d) 440 nm ± 40 nm.

Chapter 5. Publication: Thin-Film Superelastic Alloys for Stretchable Electronics

Own contributions to the following article[1].

- sample fabrication (large fraction)
- differential scanning calorimetry (large fraction)
- tensile testing (large fraction)
- electrical property characterization (large fraction)
- finite element analysis (minor fraction)
- infrared thermography (moderate fraction)
- interpretation of the results (large fraction)
- writing of the manuscript (large fraction)

Reproduced from

Curtis, S.M., Gugat, J.L., Bumke, L., Dengiz, D., Seigner, L., Schmadel, D., Lazarus, N.S., and Quandt, E., (2023) Thin-Film Superelastic Alloys for Stretchable Electronics. *Shape Memory and Superelasticity*, 1-15, *Invited Feature Paper*, https://doi.org/10.1007/s40830-023-00422-4

[1] this page is required by regulations

Motivation:

The mechanical properties of thin-film shape memory alloys are desirable for integration into MEMS devices that require large levels of deformation. The fields of flexible and stretchable electronics aim to reconfigure typical MEMS components into geometries that enable the component to undergo large levels of deformation (e.g., bending, stretching, twisting). The research for my master's thesis took place at the Army Research Lab in Adelphi, MD. I spent two years studying the mechanical properties of single-crystal silicon structured into stretchable serpentine geometrical shapes. With the serpentine geometry, single-crystal silicon was able to stretch to a macroscopic strain of 84% [69]. The intrinsic elastic strain limit of silicon ($\varepsilon < 1\%$) is much lower than that of SMAs ($\varepsilon = 1.8\% - 8\%$). To my surprise, at the start of my doctoral thesis, shape memory alloy thin-films had not been integrated into stretchable electronic applications.

While completing my master's thesis in 2018, I wrote a proposal to the National Science Foundation Graduate Research Fellowship (NSF GRFP) to use MEMS fabrication techniques to integrate shape memory alloy thin-films into stretchable electronics. The work below is the first theoretical and experimental study of freestanding thin-film TiNiCuCo superelastic alloys for stretchable interconnects. Since the martensitic transformation temperatures of TiNiCuCo are below room temperature, all fabricated TiNiCuCo films demonstrate superelasticity at room temperature. Superelasticity is advantageous for stretchable interconnects because the interconnect will recover its deformation after the removal of the applied force. The results reported in this article reveal the mechanical advantages of replacing thin-film serpentine interconnects made from traditional metals like Cu with shape memory alloys such as TiNiCuCo. Overall, these results show the advantages of using sputtered thin-film SMAs as both freestanding substrates and serpentine interconnects in the design of stretchable electronic devices.

5.1 Abstract:

Conductive serpentine interconnects comprise fundamental building blocks (e.g., electrodes, antennas, wires) of many stretchable electronic systems. Here we present the first numerical and experimental studies of freestanding thin-film TiNiCuCo superelastic alloys for stretchable interconnects. The electrical resistivity of the austenite phase of a $Ti_{53.3}Ni_{30.9}Cu_{12.9}Co_{2.9}$ thin-film at room temperature was measured to be 5.43×10^{-7} Ω m, which is larger than reported measurements for copper thin-films (1.87×10^{-8} Ω m). Structuring the superelastic conductor to limit localized strain using a serpentine geometry led to freestanding interconnects that could reach maximum serpentine elongations of up to 153%. Finite element analysis (FEA) simulations predicted that superelastic serpentine interconnects can achieve significantly larger (~5X-7X) elastic elongations than copper for the same serpentine geometry. FEA predictions for stress distribution along the TiNiCuCo serpentine interconnect were experimentally verified by infrared imaging and tensile testing experiments. The superior mechanical advantages of TiNiCuCo were paired with the high electronic conductivity of copper, to create Cu/TiNiCuCo/Cu serpentine composites that were demonstrated to serve as freestanding electrical interconnects between two LEDs. The results presented in this manuscript demonstrate that thin-film superelastic alloys are a promising material class to improve the performance of conductors in stretchable and flexible electronics.

5.2 Introduction

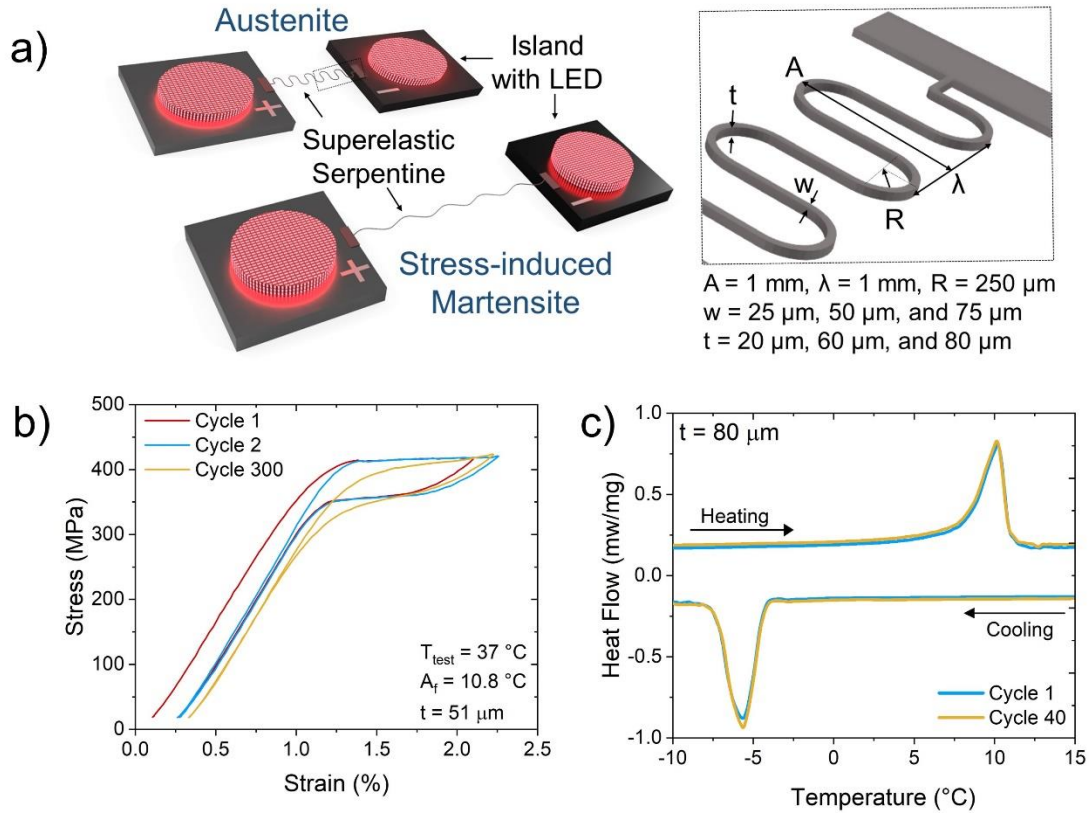

Figure 5.1: a) 3D schematic demonstrating "island plus serpentine" stretchable design with a superelastic serpentine interconnect at equilibrium in the austenite phase and stretched in the stress-induced martensite phase. (insert) Serpentine geometry dimensions investigated in this study. b) Tensile testing curves of a 51 μm thick TiNiCuCo dogbone specimen after superelastic cycling between ε = 0% - 2.1% for 300 cycles. c) Differential scanning calorimetry curves demonstrating thermal reversibility for an 80 μm thick TiNiCuCo sample for 40 cycles.

The next generation of biointegrated devices [180], epidermal electronics [52], and wearable energy harvesting and storage devices [181] must accommodate large levels of physical deformation (i.e., elastic strains as large as 75% - 100%) [182, 183] to ensure conformal contact to the human skin and tissue. Flexible and stretchable electronics use microelectromechanical systems (MEMS)-inspired techniques to reconfigure thin-film electronic components into new designs that can withstand high levels of flexing, bending, and twisting deformation [53, 54, 62].

As depicted in the schematic in **Figure 5.1a)**, the popular "island plus serpentine" design connects functional device "islands" by wavy serpentine interconnects. Under an applied force, the serpentine will elongate by changing shape to accommodate the deformation of the stretchable circuit. The serpentine structure non-uniformly distributes stress/strain throughout the geometry, enabling the serpentine to elastically elongate to large levels of applied strains [63, 184, 185]. At the same time, under deformation, the islands undergo low stresses, enabling them to house any stress-sensitive components (e.g., photovoltaics, batteries, LEDs, or embedded sensor elements) [62, 181, 186]. Essentially, the serpentine structure can enable any material to become stretchable including, for example, liquid metal [187], thin film metals such as copper (Cu) [64–66, 186, 188] and gold [181], and semiconductors such as silicon [69, 70, 189, 190] and gallium nitride [71–73].

Nickel-titanium (NiTi) is one of the most commercially prevalent shape memory alloys (SMAs) because of its large reversible transformation strain of up to $\varepsilon = 8\%$ [34, 37]. Sputtered thin-film NiTi alloys are employed in numerous high-bending applications such as self-expanding stents [191], micro-valves [8, 98], micro-actuators [3, 8, 15, 20], and other types of microdevices [1, 192]. Additionally, it has been shown that thin-film NiTi stents can be functionalized with other materials such as Pt or PtIr electrodes for bioelectronic sensing to produce next-generation smart medical devices [191]. The strain recovery of up to $\varepsilon = 8\%$ in NiTi-alloys is enabled by a reversible structural phase transformation between monoclinic (B19') or orthorhombic (B19) martensite and cubic (B2) austenite [28]. Through a twinning/detwinning process, martensite can be deformed to extremely large strains which can be entirely recovered by a thermally induced phase transformation, known as the *shape memory effect*. In the case of austenite, large superelastic strains are recovered through a stress-induced phase transformation from austenite to stress-induced martensite, known as, the *superelastic effect* [34]. With proper chemical composition,

fabrication (e.g., multilayer sputter deposition approach) [193], heat treatment, and surface finish, thin-film SMAs like $Ti_{54}Ni_{34}Cu_{12}$ and $Ti_{54.7}Ni_{30.7}Cu_{12.3}Co_{2.3}$ can repeatedly undergo this transformation with ultralow-fatigue [18]. These thin-film SMAs were shown to undergo the superelastic transformation to a strain of $\varepsilon = 2\%$ for 10+ million cycles [18, 193]. Despite other known advantageous properties of NiTi SMAs such as bio-compatibility, corrosion resistance [37], high strength, high actuation densities, and good electrical conductivity [34], these SMAs are seldom employed in stretchable electronic applications [74].

Recently, the superior mechanical properties offered by superelastic NiTi wires were shown to be advantageous compared to Cu wires for stretchable electronics. 100 μm thick serpentine structures of superelastic NiTi wires were shown to have a high elastic stretchability of 196% credited to the large intrinsic superelastic strains of $\varepsilon = 7.5\%$ achievable by NiTi, as well as the non-uniform strain distribution offered by the serpentine structure [74]. These NiTi serpentine wires were demonstrated to reversibly cycle stretching of 100% for 1,000 cycles, whereas Cu wire serpentine interconnects were plastically deformed after stretching to 100% for 1 cycle [74]. Cu is currently the most widely used stretchable conductor due to its very low electrical resistivity $1.87 \times 10^{-8}\ \Omega$ m [194]. The electrical resistivity of liquid metal EGaIn, another popular conductor used in stretchable electronics, is $1.77 \times 10^{-6}\ \Omega$ m [195]. In comparison, NiTi is reported to have an electrical resistivity of $7.6 \times 10^{-7}\ \Omega$ m in the martensite phase, and $1.0 \times 10^{-6}\ \Omega$ m in the austenite phase [34]. While Cu thin-films have superior electrical properties compared to SMAs, the challenge with stretchable Cu interconnects is their low intrinsic elastic strain ($\varepsilon = 0.26\%$ [196]) which leads to the accumulation of plastic deformation in the interconnect at low applied serpentine elongations.

The experimental and numerical studies presented here compare the mechanical and electrical properties of thin-film superelastic TiNiCuCo serpentine interconnects with thin-film Cu serpentine interconnects for use in stretchable electronic applications. Following a MEMS-compatible fabrication process developed by *Lima de Miranda* [11, 12], one can fabricate freestanding SMA thin-films into any custom stretchable geometry (e.g. auxetic geometries [21]) with feature sizes as small as 10 microns. The stress-induced phase transformation from austenite to stress-induced martensite can be used to develop stretchable circuits that can reversibly stretch to large levels of applied external strain, as depicted in **Figure 5.1a)**. Thermal-mechanical behavior of the TiNiCuCo serpentines are evaluated by comparing direct experimental results with finite element analysis simulations.

Additionally, the results presented in this work demonstrate that Cu/SMA composites can combine the excellent electrical conductivity of Cu thin-films with the superior mechanical properties of superelastic thin-films to develop freestanding stretchable interconnects that are both conductive and reversibly stretchable. While we demonstrate only one composition of a TiNiCuCo alloy, our results show the promise of integrating various other thin-film NiTi-based SMAs into stretchable electronics.

5.3 Methods and Materials

5.3.1 Sample preparation:

Free-standing SMA films were fabricated through a combination of UV-lithography, DC magnetron sputtering, and a wet chemical etching process as described in detail by *Lima de Miranda et. al* [29]. The films included single-period and five-period serpentine mechanical test

structures with three different thicknesses (t = 20 μm, 60 μm, and 80 μm) and serpentine widths (w = 25 μm, 50 μm, and 75 μm). As shown in **Figure 5.1a)**, all fabricated serpentines had an arc radius (R) = 250 μm, a wavelength (λ) = 1 mm, and a peak-to-peak amplitude (A) = 1 mm. A cluster magnetron sputtering device with a base pressure < 3 x 10^{-7} mbar (model CS730S by Von Aardenne GmbH, Germany) was used to sputter amorphous TiNiCuCo onto a pre-structured 100 mm silicon substrate. Sputtering took place with a 200 mm TiNiCuCo target (FHR Anlagenbau GmbH, Germany) at a pressure of 2 × 10^{-3} mbar, an argon flow of 20 sccm, and a DC power of 300W, resulting in a deposition rate of ~2 μm / hour. Rapid thermal annealing (RTA) using an RTA-6 SY09 (Createc Fischer, Germany, base pressure < 1 x 10^{-7} mbar) was performed at 700 °C for 15 minutes with a heating rate of 50 °C/s to crystallize the amorphous films. Due to slight variations in the fabrication process, the cross-section of the serpentine's area varies by up to 10% and exhibits a trapezoidal cross-sectional shape rather than the desired rectangle cross-section. Additionally, thickness variations of up to 10% were found from the center to the edge of the wafer. These compositional and geometrical variations are expected sources of error in the following measurements and experiments.

5.3.2 Energy Dispersive X-ray Spectroscopy (EDX):

The actual film composition of a 5 μm thick amorphous TiNiCuCo layer on a 100 mm Si substrate was determined using a Helios NanoLab 600 scanning electron microscopy (FEI, Germany) equipped with energy-dispersive X-ray spectroscopy (EDX) silicon drift detector (Oxford Instruments, UK). Quantitative analysis used a $Ti_{49.60}Ni_{50.40}$ binary standard. EDX measurements were taken in a line scan across the sputtered amorphous TiNiCuCo film on a 100 mm silicon substrate. The composition was found to vary from $Ti_{53.3}Ni_{30.9}Cu_{12.9}Co_{2.9}$ at the

center and $Ti_{53.0}Ni_{31.5}Cu_{12.7}Co_{2.8}$ at the edge of the wafer, with an error around ± 0.5 at.%. This characterization wafer is in addition to the freestanding wafers with serpentine specimens.

5.3.3 Differential Scanning Calorimetry (DSC):

Thermal analysis included thermal cycling of all fabricated TiNiCuCo films and was conducted on a differential scanning calorimeter (DSC 204 F1 Phoenix by Netzsch, Germany). The heating and cooling rate was 10°C min^{-1}. The transformation temperatures and latent heat of the SMA were determined using the internal software, Proteus 7.1.0, and the tangent method. Thermal hysteresis was calculated according to $\Delta T = \frac{1}{2}(A_s + A_f - M_s - M_f)$, where A_s and A_f correspond to the austenite start and finish temperatures, and M_s and M_f correspond to the martensite start and finish temperature.

5.3.4 Tensile Testing:

Functional stability of the phase transformation during superelastic mechanical cycling of a TiNiCuCo dogbone specimen and single-period serpentines was evaluated using a tensile tester (Zwick Roell Z.05) at a temperature of 37 °C using a strain rate frequency of 0.02 Hz to maintain isothermal loading conditions. The dogbone specimen was preloaded to a force of 0.5 N prior to measurement, whereas serpentine specimens were preloaded by a much smaller force of 0.001 N. **Figure 5.1b)** demonstrates the superelastic hysteresis loop of a TiNiCuCo dogbone specimen (parallel length of 13 mm, 500 μm wide, 51 μm thick). After 300 cycles between ε = 0% - 2.1% there was unrecoverable plastic strain ($\varepsilon_{plastic}$ = 0.28%), due to the buildup of remnant martensite.

Due to the non-uniform cross-section across the serpentine mechanical test structures, the data is reported as 'force vs serpentine elongation' instead of 'stress vs strain'. Serpentine elongation is defined as $\frac{\Delta l}{l}$*100% where l is the initial end-to-end length of the serpentine in the equilibrium position when the sample is in the austenite phase under no applied external force. Tensile testing took place on single-period serpentine mechanical test structures, with an initial end-to-end length, i.e., the end-to-end distance, l = 1 mm.

5.3.5 Electrical resistivity of TiNiCuCo:

The electrical resistivity of an 18.6 μm thick TiNiCuCo film was determined by using four-point resistance measurements carried out inside a cryostat. Quasi-stationary conditions help guarantee that the temperature is constant so that thermally induced changes in resistance are negligible during measurement. The electrical resistivity of the austenite phases at room temperature of TiNiCuCo was determined to be 5.43×10^{-7} Ω m, slightly lower than the resistivity reported for binary NiTi [34].

5.3.6 Stress-Induced Electrical Properties:

The stress-dependent electrical properties were determined for 20 μm thick five-period serpentine mechanical test structures having 5 mm unstretched length using a custom-built translation stage to allow four-point resistance measurements while stretching the serpentine. Serpentines were loaded and unloaded at room temperature at a rate of 0.5 mm/s for serpentine elongations of 0% - 30% for 1,000 cycles. A power supply provided a constant current of 0.05 A

± 0.005 A along the serpentine trace, while an ohmmeter monitored the change in electrical resistance.

5.3.7 Stretchable LED demonstration:

Here we consider metallic thin-film superelastic serpentines as freestanding substrates for other conductors for use in stretchable electronics. Cu/TiNiCuCo/Cu serpentine composites were used as freestanding electrical interconnects between two LEDs. The wettability of solder on SMA surfaces is known to be poor because the surface of NiTi-based SMAs forms a stable native oxide layer (TiO_2). However, the thin layer of sputtered copper or gold on top of the native TiO_2 layer on TiNiCuCo films was found to make a stable connection for lead-based solder. TiNiCuCo five-period serpentines with t/w = 20/75 and 80/75 were sputter deposited with 5 μm thick Cu on one side, and 500 nm Cu on the other side. Each Cu/TiNiCuCo/Cu serpentine composite was then soldered between two red LEDs (Lumitronix LED-Technik GmbH, Germany). A copper wire (diameter = 0.5 mm) was soldered between the external LED contact pads and connected to a power supply. A constant voltage (V) of 3.5 V was applied to the circuit. The current (I) and corresponding resistance (R) was monitored as a function of serpentine elongation. The resistance of the circuit is calculated according to ohms law (R = I/V). Potential mechanical inconsistencies in the experimental set-up such as solder joint integrity, wire lengths, and power supply fluctuations are sources of error in this experiment. Another source of error that is not considered is local temperature fluctuations that arise from the latent heat of transformation upon stretching superelastic materials [197].

5.3.8 Infrared (IR) thermography:

Single-period and five-period serpentine mechanical test structures (t = 60 μm, w = 50 μm) were spray-coated with a ~10 μm carbon coating (Graphit33, CRC Industries). Single-period serpentines were loaded and unloaded at room temperature at a strain rate of 20 mm/s between serpentine elongations of 0% - 33%. Five-period serpentines were tested with a strain rate of 15 mm/s. A FLIR A655sc camera with a minimum pixel size of 11 μm was used to detect changes in the temperature at regions of maximum strain concentration in the serpentine.

5.4 Results and Discussions

5.4.1 Thermal Induced Martensitic Transformation

Table 5.1: Martensitic transformation temperatures and enthalpy of transformation obtained from the center of the wafer for cycle 1 and cycle 40 on fabricated 20 μm, 60 μm, and 80 μm thick films, determined by DSC

TiNiCuCo Film Thickness	Cycle No	A_s [°C]	A_f [°C]	A_p [°C]	$\Delta H_{M\rightarrow A}$ [J/g]	M_s [°C]	M_f [°C]	M_p [°C]	$\Delta H_{A\rightarrow M}$ [J/g]	ΔT [°C]
20 μm	Cycle 1	8.62	9.96	9.36	7.22	-4.63	-5.59	-5.10	9.95	14.40
20 μm	Cycle 40	8.62	9.91	9.36	7.14	-4.63	-5.57	-5.09	10.04	14.37
60 μm	Cycle 1	9.29	11.01	10.39	7.10	-3.84	-5.18	-4.62	10.18	14.66
60 μm	Cycle 40	9.31	11.01	10.39	7.08	-3.84	-5.23	-4.63	10.24	14.70
80 μm	Cycle 1	8.46	11.00	10.26	6.98	-4.34	-7.30	-5.66	9.48	15.55
80 μm	Cycle 40	8.34	10.93	10.14	7.09	-4.33	-7.20	-5.63	9.37	15.40

The most practical SMAs for stretchable systems will be those that have austenite finish temperatures (A_f) below room temperature, to ensure all applied deformation to the stretchable

SMA can be recovered through the superelastic effect. Differential scanning calorimetry (DSC) was used to evaluate the martensitic transformation temperatures and enthalpies from TiNiCuCo samples with different thicknesses (t = 20 μm, 60 μm, 80 μm) and prepared in different wafer batches. As shown in **Table 5.1** all samples have austenite finish (A_f) temperatures between 10 °C – 11 °C, therefore they are superelastic at room temperature. Similar transition temperatures and latent heat values were obtained for all samples which indicates that all samples have similar atomic compositions and microstructure characteristics. DSC was also used to evaluate thermal fatigue in all samples. **Figure 5.1c)** demonstrates good thermal reversibility for an 80 μm thick TiNiCuCo film. After 40 cycles, there was a change of less than 0.1K and 0.1 J/g in the martensitic/ austenitic transformation temperatures and transformation enthalpies, respectively, implying that all fabricated samples have low functional fatigue [33]. Additionally, all fabricated samples have a narrow thermal hysteresis (ΔT = 14 °C – 15.5 °C), which indicates that the middle eigenvalue of transformation strain is close to zero which is a prerequisite for cycling stability [35, 198].

In some cases, upon cooling, a double peak was observed on the martensite peak for the 20 μm and 60 μm thick samples which might be an indication that an intermediate phase transition occurs during the phase transformation. Alternatively, the double peaks could arise due to the inhomogeneity of the microstructure throughout the sample [199, 200]. To precisely determine the origin of the multi-step transformation and one must confirm the size and homogeneity of the Ti_2Cu precipitates using temperature-dependent X-ray diffraction, transmission electron microscopy, and scanning electron microscopy studies. Such experiments are beyond the scope of this work. The reader is guided to the following studies on the influence of microstructure, and crystallographic phase compatibility on the functional and structural fatigue of thin-film SMAs [33, 35, 193, 198].

5.4.2 Superelastic Serpentine Mechanics:

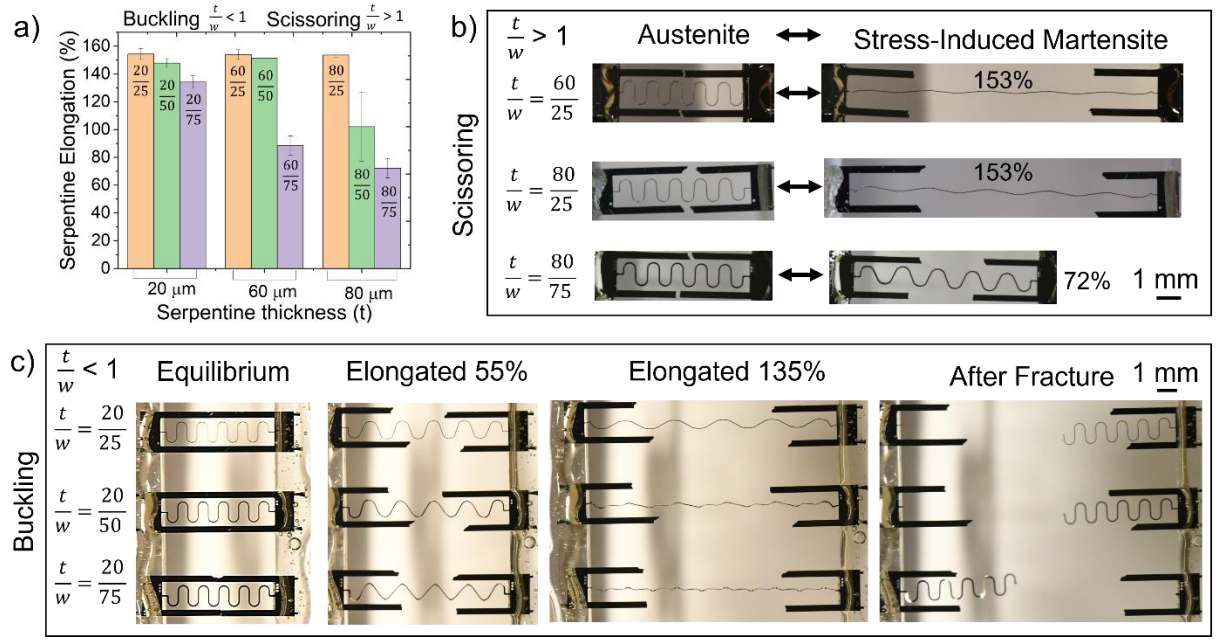

Figure 5.2: Buckling and scissoring deformation dependence for superelastic serpentines. a) Maximum serpentine elongation at fracture for all tested serpentine specimens. b) Demonstration of scissoring deformation (t/w > 1) for serpentines with t/w = 60/25, 80/25 and 80/75. c) Demonstration of buckling deformation (t/w < 1) for serpentines with t/w = 20/25, 20/50, and 20/75. The fracture images show superelastic recovery after applying the maximum serpentine elongation to the specimens.

The maximum elongation achieved by a serpentine is dependent on the material's mechanical properties, as well as the dimensions of the serpentine's thickness/width (t/w) aspect ratio. *Su et al.* showed the scissoring or buckling mechanical deformation mode of a serpentine trace is dependent on the t/w aspect ratio of the serpentine geometry [196]. Buckling deformation occurs when the t/w < 1 because rotational and torsional forces cause the serpentine to bend and twist out-of-plane [186]. Scissoring occurs when the t/w > 1 because rotation is no longer feasible, and therefore only in-plane (non-buckling) deformation is possible [196].

The maximum serpentine elongation at fracture along with the geometrical buckling/scissoring dependence was determined through strain-to-rupture tests on five-period serpentine mechanical test structures. All samples were mounted in a custom-built 3D-printed holder which could precisely apply a uniaxial displacement to the fabricated serpentine structures while taking optical images. Serpentine elongation ($\frac{\Delta l}{l}$*100%, where l = 5 mm) was calculated through image processing with the program *Image J*. **Figure 5.2a)** shows the average maximum applied serpentine elongation before fracture as a function of the t/w aspect ratio. Where provided, the error bars represent the standard deviation from the average value of each measurement for at least three tested serpentine samples. Serpentines of all t/w ratios were found to reach large maximum serpentine elongations between 72% - 153%. As the serpentine width or thickness increases, the effective stiffness of the cross-section becomes greater, thus smaller uniaxial displacements result.

Freestanding SMA serpentines are found to follow similar buckling and scissoring deformation dependencies reported for thin-film Cu serpentines [196]. When the serpentine thickness was increased to 80 μm, only in-plane bending, i.e., scissoring, deformation is obtained. **Figure 5.2b)** shows scissoring deformation behavior for superelastic serpentines with t/w = 60/25, 80/25, and 80/75. The serpentine samples are unstretched in the austenite phase at equilibrium. The phase transformation to stress-induced martensite occurs by stretching the serpentine. Samples with a serpentine width of 25 μm (t/w = 20/25, 60/25, and 80/25) exhibited average maximum serpentine elongations of 153% ± 4%, approaching the shape of a straight line, with kinks. As shown in **Figure 5.2c)**, all 20 μm thick serpentines have a t/w < 1, and in these cases, the serpentines deflect out-of-plane under elongation, resulting in buckling deformation. All 20 μm thick samples (t/w = 20/25, 20/50, and 20/75) were found to reach maximum applied elongations

between 134% - 153%. After sample fracture, all tested serpentine segments, regardless of serpentine thickness or width, mostly returned to their equilibrium form with only minimal observable plastic strain, as shown in **Figure 5.2c)**. Only slight plastic deformation was observed at the regions of maximum stress, which includes the anchor connection points of the mechanical frame, as well as in the curved regions of the serpentine structure (i.e., arc). Plastic strain accumulation in the superelastic interconnect could be mitigated by using a stretchable geometry that distributes stress more uniformly throughout the structure (e.g., fractal serpentine interconnects [189], archimedean spirals [201], stretchable auxetic geometries [21]).

5.4.3 Finite Element Analysis and Experimental Comparison

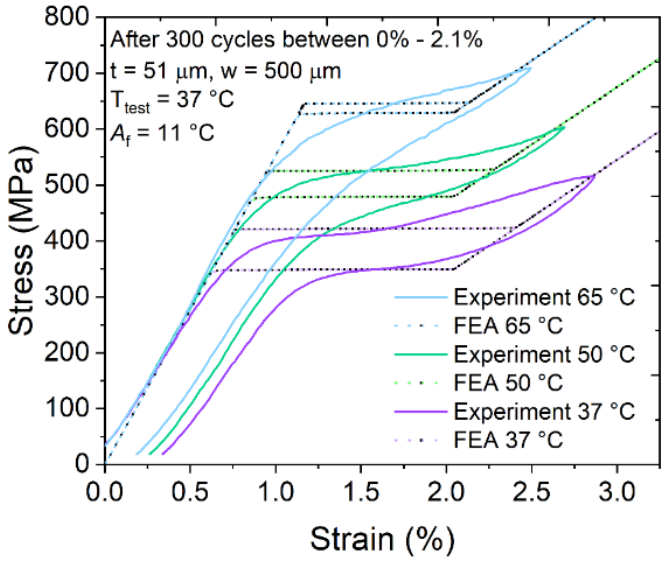

Figure 5.3: Temperature-dependent tensile test performed on traditional TiNiCuCo dogbone. Experimental tensile testing results were empirically fit to extract several of the FEA parameters (e.g., Clasius Claperyon Coefficient). Dotted curves show FEA results while solid curves show the experiment.

The performance of superelastic TiNiCuCo serpentine and Cu serpentine interconnects under strain loading conditions are numerically compared utilizing finite element analysis (FEA). *Gugat et al.* [32] previously developed a custom 2D FEA model using COMSOL Multiphysics 5.3a to evaluate the thermal-mechanical behavior of structured NiTi thin-films under strain loading. This model was adapted to analyze and compare the stretchable behavior of TiNiCuCo and Cu serpentines. The model includes SMA dynamic mechanical analysis and kinetic energy transfer simulations to allow the simultaneous analysis of the von Mises stress distribution, maximum principal strains, and the volume fraction of material that transformed from austenite to stress-induced martensite.

The SMA material properties (critical stress, critical strain, transformation temperatures, and Clasius-Claperyon coefficients ($C_{AM,}$ C_{MA})) of TiNiCuCo for the FEA model were estimated based on the results of temperature-dependent tensile testing and differential calorimetry experiments. **Figure 5.3** demonstrates temperature-dependent tensile tests at 37 °C, 55 °C, and 65 °C on a fabricated freestanding TiNiCuCo dog bone specimen (parallel length of 13 mm, 500 μm wide, 51 μm thick). Experimental tensile testing results were empirically fit to extract several of the material properties used in the model, see **Table 5.2.** The comparison of the experiment and FEA results determined the recoverable strain from the superelastic transformation for TiNiCuCo to be $\varepsilon = 1.8\%$. There was a total of $\varepsilon_{plastic} = 0.28\%$ in the sample because the dogbone had previously been cycled between $\varepsilon = 0\% - 2.1\%$ for 300 cycles, as was shown in **Figure 5.1a)**. The influence of fatigue and plastic deformation is not implemented into the SMA model. For simulations, the yield stress and elastic strain limit for Cu were determined to be 200 MPa, and 0.26%, respectively. The Cu material properties are similar to the properties reported in theoretical and experimental studies of buckling and scissoring thin-film Cu serpentine

interconnects on polymer substrates [196]. A summary of the most important material properties considered in the simulation is given in **Table 5.2,** however, the full list of all parameters used in the model is given by *Gugat et al.* [32].

Table 5.2: Material parameters of copper and TiNiCuCo thin-films used in FEA simulations.

	Density [kg/m^3]	Poisson's Ratio	Young's Modulus [GPa]	Elastic strain limit (ε):	Transformation Temperature [°C]	Clasius Claperyon Coefficient [MPa/K]
Copper	8940	0.34	119	0.26%	NA	NA
TiNiCuCo (martensite)	6450	0.33	20	1.8%	M_s = -10°C M_f = -53.09 °C	C_{AM} = 8.0
TiNiCuCo (austenite)	6450	0.33	55	1.8%	A_s = 0 °C A_f = 5° C	C_{MA} =10.0

Structural mechanical FEA simulations were implemented for 2D problems with plane stress assumptions, neglecting possible out-of-plane movement. Therefore, the simulations are more accurate for thicker serpentines (e.g., t = 60 μm and 80 μm) that were shown to deform in-plane through scissoring deformation. The stretching performance of single-period Cu and TiNiCuCo serpentines are numerically compared by FEA for 80 μm thick serpentines with varying widths (t/w = 80/10 – 80/80). The maximum quasi-elastic serpentine elongation for a superelastic material is determined by the recoverable strain of the superelastic phase transformation. Simulations are performed by holding one end of the serpentine fixed and applying a uniaxial displacement until the maximum principal strain (or von Mises stress) in the serpentine exceeds the elastic stress or strain limit of materials. **Figure 5.4a)** shows the FEA prediction of the maximum elastic serpentine deformation as a function of serpentine width for 80 μm thick

TiNiCuCo and Cu. These simulation results predict that the maximum quasi-elastic serpentine elongation for TiNiCuCo is at least ~5X-7X larger than Cu, depending on the t/w ratio of the geometry. Through FEA, it was determined that the fracture stress for Cu thin-films was between 607 MPa – 715 MPa at intrinsic strains of ε = 0.54 % – 0.64 %. As shown in **Figure 5.4b)** FEA predicts that a Cu serpentine with a t/w = 80/25 would be fractured at serpentine elongations of 13% whereas a TiNiCuCo of the same dimensions could elastically elongate to 32%. TiNiCuCo serpentines with t/w = 80/25 were found to experimentally fracture at serpentine elongations of 153%. Simulation results predict that the serpentine structure will accumulate strain in localized regions (e.g. inner arcs) when deforming in-plane through scissoring deformation. The greater ductility offered by superelastic materials also allows superelastic interconnects to reach much larger levels of applied external strain before fracture compared to Cu interconnects.

The model was also able to closely predict the superelastic hysteresis loop shape and maximum critical forces for serpentines of all t/w aspect ratios. For example, **Figure 5.4c)** shows the superelastic hysteresis loop between the experiment and FEA model for a TiNiCuCo serpentine (t/w = 60/75) when elongated between 0% - 50%. FEA results of Cu in the same constitute geometry are also plotted in **Figure 5.4c)** to demonstrate that a Cu serpentine undergoes much larger forces at lower applied serpentine strains compared to TiNiCuCo. Additionally, the 60 μm TiNiCuCo sample experimentally did not superelastically complete the phase transformation, reflected by the 4.8% plastic serpentine elongation caused by remnant martensite after one cycle. The formation of plastic strain implies that the maximum principal strain in the TiNiCuCo likely exceeded ε = 1.8%. **Figure 5.4d)** shows that when a serpentine with t/w = 20/75 is elongated to 50%, its phase transformation was entirely recovered through the superelastic phase transformation, implying the maximum principal strain in the material was below ε = 1.8%.

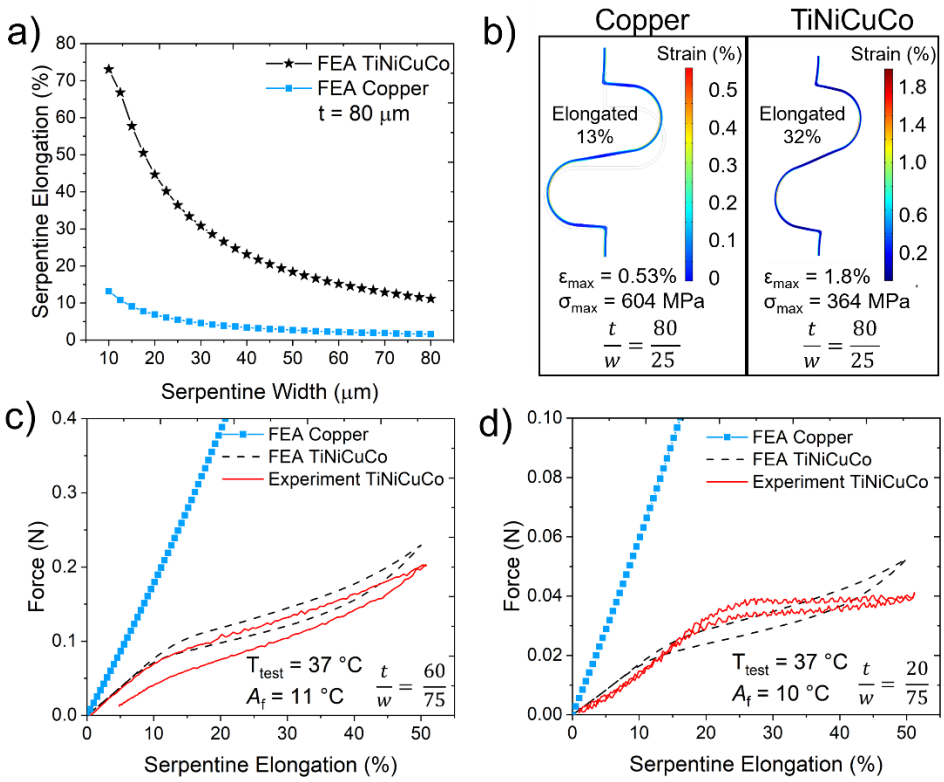

Figure 5.4: a) FEA comparison of maximum elastic serpentine elongation achieved for 80 μm thick Cu and superelastic TiNiCuCo serpentines with varying widths. **b)** Non-uniform strain distribution of a Cu and TiNiCuCo serpentine (t/w = 80/25) after serpentine elongations of 13% and 32%, respectively. Experiment and FEA comparison of force vs serpentine elongation for a TiNiCuCo serpentine with **c)** t/w = 60/75 and **d)** t/w = 20/75.

FEA simulations were implemented to study the change in superelastic behavior for serpentines of different widths and thicknesses. **Figure 5.5a)** shows simulation results of all t/w ratios for the maximum force from which the superelastic TiNiCuCo serpentines can superelastically recover elongation with no plastic deformation. As the cross-sectional area of the serpentine interconnects increases, there is more SMA material available to actively transform from austenite to stress-induced martensite, thus larger forces can be superelastically recovered. **Figure 5.5b)** shows the overlay of FEA results and tensile testing experiments until sample fracture for 20 μm thick TiNiCuCo serpentines. Even though the model neglects out-of-plane

movement, these experiments verify that the FEA model was able to accurately predict the critical force value for serpentines that were experimentally shown to undergo out-of-plane buckling deformation, as shown in **Figure 5.2c)**.

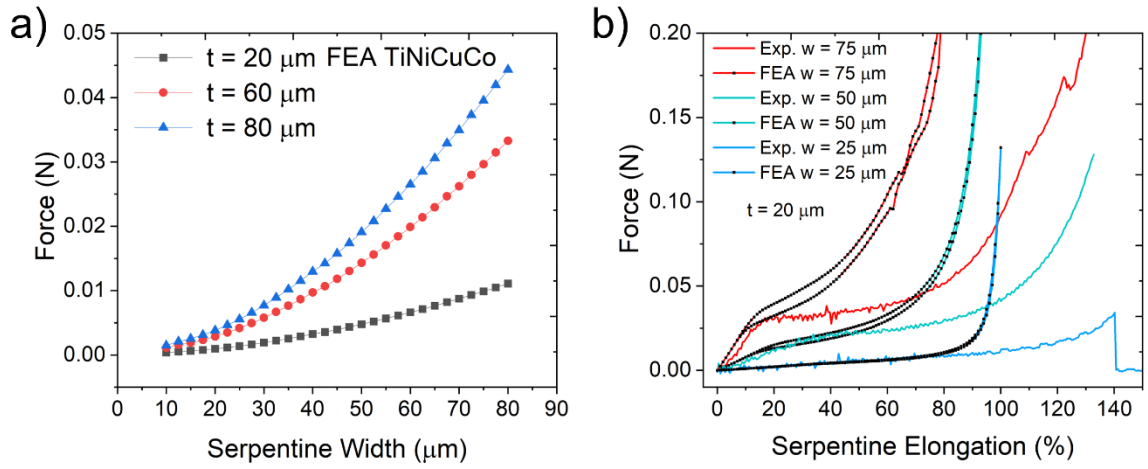

Figure 5.5: a) FEA prediction of maximum critical force that results in superelastic deformation for all t/w aspect ratios. **b)** FEA and experiment comparison of maximum serpentine elongation before fracture for serpentines with t/w = 20/25, 20/50, and 20/75.

Figure 5.6a) shows FEA results for the von Mises stress distribution, first principal strain, and martensitic volume fraction distributions along a TiNiCuCo serpentine (t/w = 80/50) after applying a serpentine elongation of 50%. The non-uniform strain distribution along the serpentine causes the maximum stress/ strain to concentrate along the serpentine's inner arc which is the location of the maximum radius of curvature. After a serpentine elongation of 50%, FEA results predict a maximum principal strain of $\varepsilon = 6\%$ in the inner arc of the serpentine which are the corresponding regions where the superelastic material is transforming from austenite to stress-induced martensite. The inner arcs are the location of built-up remnant martensite that led to minor plastic deformation in the superelastic serpentine.

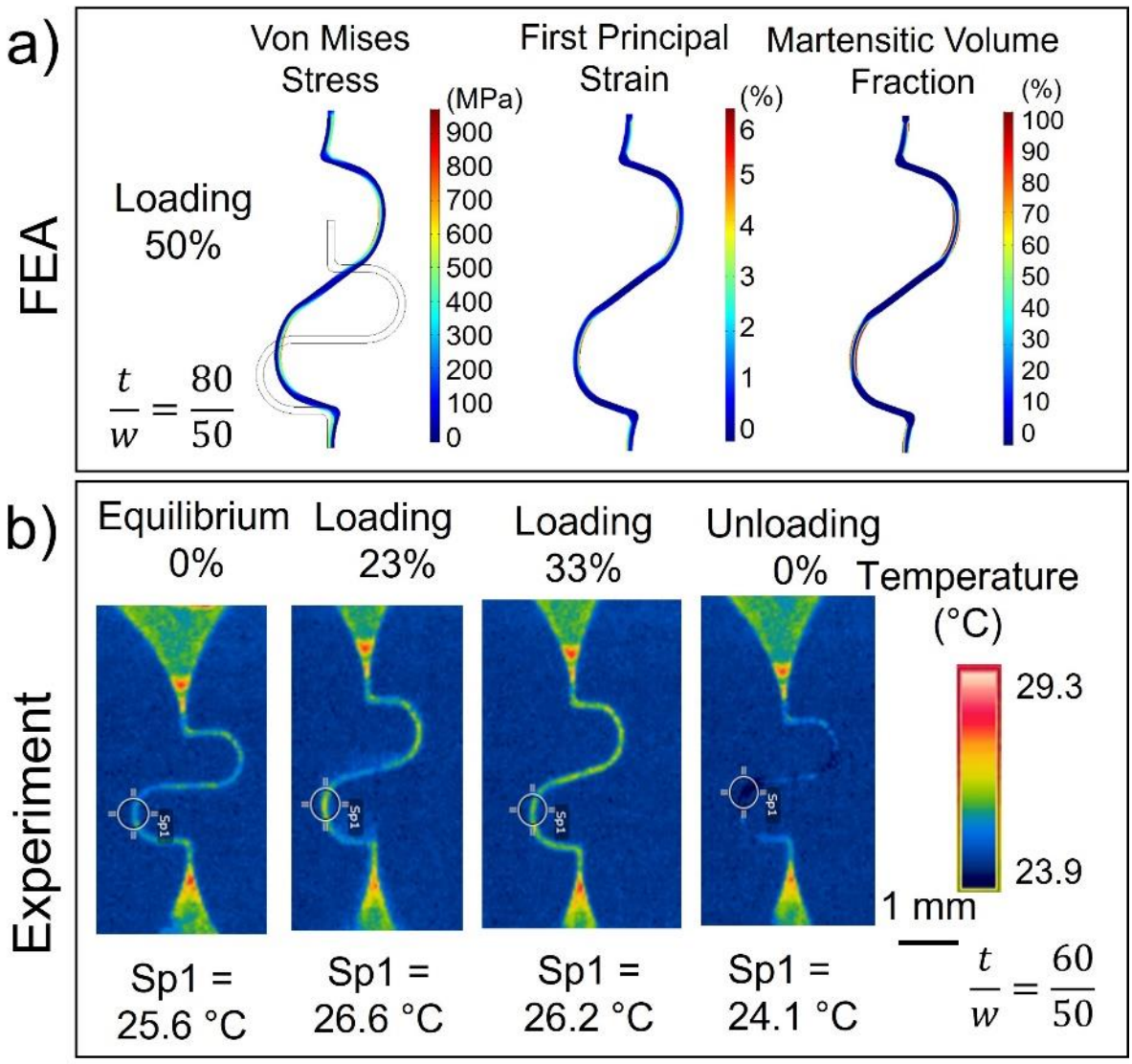

Figure 5.6: a) FEA simulations of the von Mises stress, first principal strain, and martensitic volume fraction distribution of a TiNiCuCo serpentine (t/w = 80/50) after a serpentine elongation of 50%. **b)** IR imaging demonstrating the elastocaloric effect in a superelastic TiNiCuCo serpentine (t/w = 60/50) during loading and unloading between 0% - 33% serpentine elongation.

Another advantage of using the alloy TiNiCuCo for stretchable electronics is that previously it was identified to be an excellent elastocaloric material [36, 197, 199, 202–204]. The elastocaloric effect results in the heating/ cooling of SMA materials during superelastic strain

loading/ unloading. When the SMA undergoes the phase transformation from austenite to stress-induced martensite, the release of latent heat results in an increase in temperature locally on the sample [199]. An infrared (IR) camera can be used to verify regions of maximum strain concentration by determining the localized regions along the serpentine that undergo maximum temperature change. This principle was used to confirm the FEA results, by experimentally strain testing a serpentine with t/w = 60/50 under an IR camera. These results can be compared to the FEA stress/ strain distribution results for the serpentines with t/w = 80/50, since both samples were shown to undergo in-plane scissoring stretching behavior. As shown in **Figure 5.6b)**, during strain loading between serpentine elongations of 0% and 23%, the temperature of the arc of the serpentine increased from a starting temperature of 25.6 °C to 26.6 °C. Upon further strain loading to elongations of 33%, the latent heat was distributed throughout the entire serpentine structure. Thus, the temperature in the serpentine arc slightly decreased from 26.6 °C to 26.2 °C. During unloading, the temperature of the arc of the serpentine decreased from 26.2 °C to below 24.1 °C, confirming the reverse transformation from stress-induced martensite to austenite. **Figure 5.9 (appendix),** shows similar IR imaging results on a five-period serpentine (t/w = 60/50) after a 33% serpentine elongation, confirming localized temperature change at the arcs of adjacent serpentines. These results validate the FEA results of localized strain concentration in the inner arc of the serpentine which is in alignment with previous serpentine mechanics studies [65, 69, 205, 206].

5.4.4 Stretchable Electrical Resistance Testing:

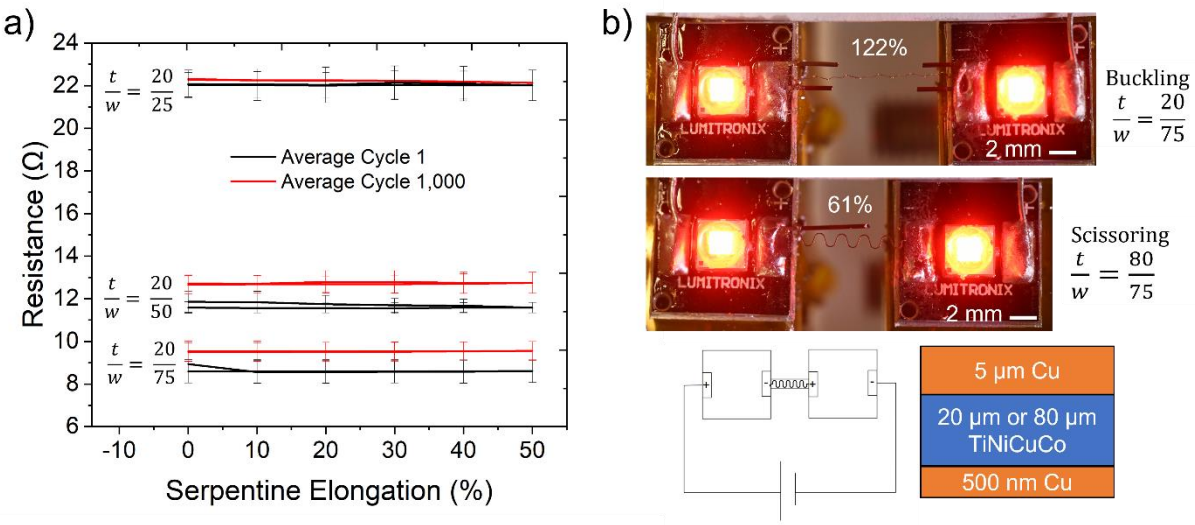

Figure 5.7: a) Strain-dependent electrical resistance measurements at cycle 1 and cycle 1,000 for TiNiCuCo serpentines with t/w = 20/25, 20/50, and 20/75. **b)** Demonstration of Cu/TiNiCuCo/Cu serpentine composites (TiNiCuCo t/w = 20/75 and 80/75) serving as a stretchable freestanding electrical interconnection between two LEDs.

The stress-induced phase transformation was detected by monitoring the electrical resistance of TiNiCuCo serpentines with a four-point probe measurement setup while loading and unloading serpentine elongations between 0% - 50% for one cycle. The average change in resistance as a function of serpentine elongation for cycles 1 and 1,000 are plotted for serpentines with t/w = 20/50, 20/50, and 20/75 in **Figure 5.7a)**. Where provided, the error bars represent the standard deviation from the average value for three tested serpentines for each t/w aspect ratio. In the first stretching cycle between 0% - 50%, there was a small change in the average electrical resistance of 0.53% - 0.8% for all tested samples. In comparison, 45 μm thick Cu serpentines were reported to have a resistance of 0.4 Ω, which changed by a few percent during stretching [196]. The influence of functional fatigue on the electrical properties of the serpentines was tested by

loading and unloading the samples to serpentine elongations between 0% - 30% for 1,000 cycles at a strain rate of 0.5 mm/s. After 1,000 cycles, there was an overall increase in electrical resistance of only 1% for a sample with t/w = 20/25, implying that this serpentine was stretched within its elastic limit ($\varepsilon = 1.8\%$), experiencing very little functional fatigue. However, after stretching 1,000 cycles, serpentines with t/w = 20/50 and 20/75 displayed an average increase in electrical resistance of 5% and 19%, respectively. The change in resistance is likely due to the formation of remnant martensite during cycling due to exceeding the reversible transformation strain of the superelastic material.

Here we consider metallic thin-film superelastic serpentines as freestanding wires for circuits and as substrates for other thin-films for stretchable electronics. Five-period TiNiCuCo serpentine mechanical test structures of two different thicknesses (t/w = 20/75, and 80/75) were coated with a 500 nm Cu on one side of the sample and 5 μm Cu on the other side. We show in a proof-of-concept demonstration that these freestanding Cu/TiNiCuCo/Cu serpentine composites can serve as stretchable electrical interconnects by using them in a circuit powering two light-emitting diodes (LEDs). The electrical resistance was monitored for a circuit consisting of a power supply, wires, and a Cu/TiNiCuCo/Cu specimen soldered between the two LEDs, as described in detail in the experimental methods. The circuit diagram of the experiment is shown in **Figure 5.7b).**

The electrical resistance of the circuit was monitored while stretching a Cu/TiNiCuCo/Cu freestanding electrical interconnect at serpentine elongations between 0% and 45% ± 5% for 40 cycles. There was no noticeable change in the electrical resistance and performance of the circuit with stretching. This independence of the conductivity under stretching was demonstrated by all tested Cu/TiNiCuCo/Cu serpentine composites, regardless of the SMA substrate thickness. The

electrical resistivity of the austenite phase of TiNiCuCo was determined to be 5.43 x 10^{-7} Ω m, which is higher than that reported for Cu thin-films (1.87 x 10^{-8} Ω m [194]). Because NiTi-based SMA thin-films have a relatively high resistivity and form a natural, insulative TiO_2 layer, it is likely that the lower resistance in the Cu thin-film coating provide substantially all the electrical conductivity across the specimen.

There was no appreciable change in the circuit when the experiment was repeated for 40 cycles for both the t/w = 20/75 and t/w = 80/75 samples. After the 40th cycle, the Cu/TiNiCuCo/Cu composite's maximum applied serpentine strain was determined. **Figure 5.7b)** shows the Cu/TiNiCuCo/Cu serpentine composite with a t/w = 20/75 under a strain resulting in a 122% elongation and the serpentine composite with t/w = 80/75 under a strain resulting in a 61% elongation. There was no appreciable change in the circuit resistance when stretching the serpentine to the maximum elongation up to fracture. Overall, the maximum serpentine elongation of the Cu/TiNiCuCo/Cu composite is lower than that of pure TiNiCuCo serpentines shown in **Figure 5.2a).** Freestanding interconnects based on Cu/TiNiCuCo/Cu serpentine composites combine the mechanical advantages of superelastic films with the electrical advantages of Cu thin-films.

5.4.5 Functional Fatigue Characterization

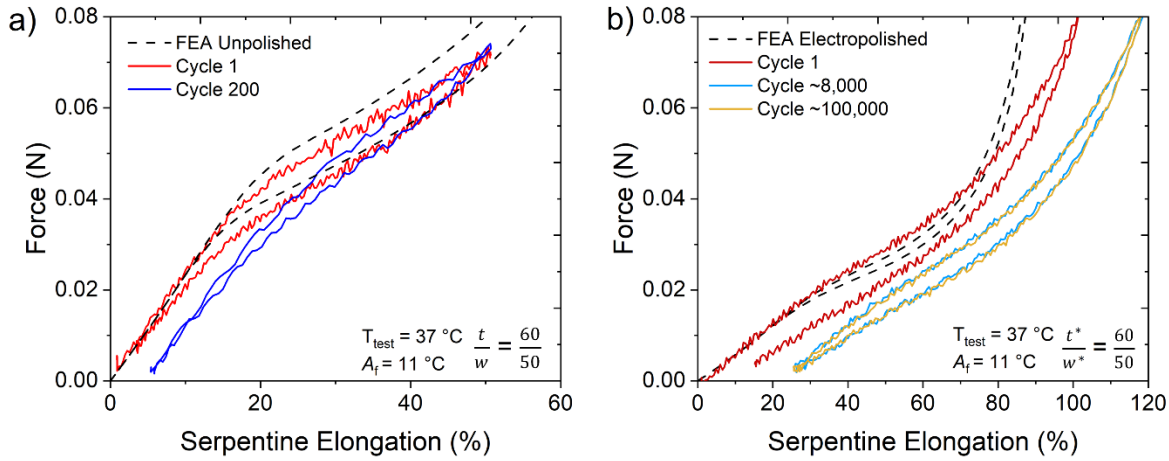

Figure 5.8: a) Degradation in hysteresis loop with superelastic cycling for an unpolished serpentine (t/w = 60/50) after serpentine elongations between 0% - 50% for 200 cycles. b) Fatigue tensile testing results of an electropolished serpentine (t^*/w^* = 60/50 before electropolishing) after cycling serpentine elongations of 20% - 50% at 20 Hz for 100,000 cycles.

Slight functional fatigue was observed when cycling all single serpentine mechanical test structures for 200 cycles. Functional fatigue arises due to the accumulation of transformation-induced defects into the microstructure and is reflected by a decrease in the critical stress (and thus critical force) with an increase in cycle number [207]. A representative 'force vs serpentine elongation' curve displaying functional fatigue in a fabricated TiNiCuCo serpentine sample with t/w = 60/50 is shown in **Figure 5.8a)**. A serpentine elongation to 50% was superelastically recovered for the first cycle and correlates well with the FEA result. However, after 200 cycles, there was an accumulation of 5.4% unrecovered serpentine elongation.

Ti-rich TiNiCuCo alloys have been reported to have high functional stability but poor structural fatigue life because of the brittleness of the film [204]. Structural fatigue in SMA thin-

films can be improved by electropolishing the film's surface because it creates a more homogeneous stress distribution at the edges, and allows for longer cycling lifetimes of up to 10^7 cycles with only negligible functional fatigue [207]. Electropolishing is used to improve the structural fatigue of SMA films by removing small surface defects like scratches, pores, and notches that can cause microcracks in the SMA films [207]. A serpentine with t/w = 60/50 was electropolished, resulting in a reduction of the serpentine's width and thickness by a few microns. The reduction in material width and thickness is reflected in the corresponding FEA model. The reduction of the material allows the serpentine to become more flexible, and able to reach larger serpentine elongations at lower critical forces.

Figure 5.8b) shows fatigue testing results for an electropolished serpentine t/w= 60/50. Force vs serpentine elongation curves were assembled for the sample at elongations between 0% - 100% using the tensile testing methods described in the experimental methods section**.** After 200 cycles, there was only 1.89% of unrecoverable elongation in the serpentine. Fatigue testing then took place in room temperature air at a strain rate of 20 Hz using a custom-built fatigue setup, as described in ref [32]. Serpentines were cycled at serpentine elongations between 20% - 50% at a rate of 20 Hz for 100,000 cycles. Force vs serpentine elongation was again measured displaying a stable hysteresis between cycle numbers ~8,000 and ~100,000. The superelastic recovery of extremely large deformations and the stability in the mechanical hysteresis between cycles 8,000 and 100,000 show the promise of integrating SMAs into high-life-cycle stretchable electronic applications.

5.5 Discussion:

The advantageous material properties of sputtered thin-film TiNiCuCo superelastic alloys for stretchable electronics were highlighted in this manuscript. The superelastic effect paired with the serpentine geometries resulted in highly stretchable interconnects. During stretching experiments, all TiNiCuCo samples with a small cross-sectional width (t/w = 20/25, 60/25, and 80/25) reached elongations of 153% ± 4%, approaching the shape of a straight wire. After the sample reached its maximum serpentine elongation and fractured, the serpentines returned to their original shape with minimal plastic deformation, showing the superelastic effect is reversible. In-plane and out-of-plane serpentine deformation was found to be determined by the serpentine's thickness/width aspect ratio, following a similar dependency as reported in prior studies on serpentine mechanics [196].

Experiments and FEA numerical studies on a $Ti_{53.3}Ni_{30.9}Cu_{12.9}Co_{2.9}$ alloy demonstrate the superelastic effect allows recovery of intrinsic elastic strains of $\varepsilon = 1.8\%$, which is much larger than Cu thin-films $\varepsilon = 0.26\%$. FEA analysis demonstrates the maximum quasi-elastic elongation of thin-film TiNiCuCo serpentines is ~5X-7X larger than that of thin-film Cu serpentines. This significant result suggests it would be advantageous to replace Cu serpentine interconnects with superelastic serpentine interconnects in applications where the stretchable circuit is subjected to large applied deformations because smaller serpentine wavelengths and amplitudes are required to achieve a desired elastic serpentine elongation. FEA analysis also revealed that only a small volume fraction of the TiNiCuCo material transforms from austenite to stress-induced martensite because localized regions (e.g., at the arcs) of the structure undergo significant strain during stretching. The regions predicted by FEA to experience maximum strain concentration were experimentally verified by detecting the elastocaloric effect through IR imaging experiments. The

arcs of the serpentine were shown to increase in temperature by 1 °C during strain loading and decrease by 2.1 °C during unloading.

Stretchable bioelectronics ideally requires direct and conformal contact interface with the skin and, should maintain a constant electrical resistance while stretching. All tested freestanding TiNiCuCo samples were shown to have low electrical resistances (9 Ω - 22 Ω) which increased by less than 1% when elongating the serpentines between 0% and 50%. Fatigue in the superelastic interconnect was also observed by monitoring the change in electrical resistance with applied cycles. Fatigue in the serpentine can be improved by electropolishing the SMA [207], or by selecting a composition of an SMA that is known to be ultra-low fatigue [18] (i.e., $Ti_{54.7}Ni_{30.7}Cu_{12.3}Co_{2.3,}$ $Ti_{54}Ni_{34}Cu_{12}$) and optimizing the microstructure [33] to ensure compatibility between the crystal lattices of the austenite and martensite phases [35]. While the functional fatigue properties of TiNiCuCo are better than that of binary NiTi, TiNiCuCo was found to have intrinsic elastic strains of $\varepsilon = 1.8\%$, which is considerably lower than the elastic strains of $\varepsilon = 7.5\%$ achieved by NiTi [74].

Typical metallic serpentine conductors like Au and Cu cannot be supported in freestanding form, and therefore must be integrated onto a polymeric substrate. SMAs, however, are strong and self-supporting, thus no elastomer is required to provide support or restore force to SMA serpentine structures. Freestanding TiNiCuCo serpentines were demonstrated to serve as substrates for sputter-deposited Cu thin-films. Cu/TiNiCuCo/Cu serpentine composites were demonstrated as freestanding stretchable electrical interconnects between two LEDs. These results support the use of structured freestanding SMAs as substrates to integrate other sputtered materials systems into stretchable electronics. If used as a substrate for stretchable devices in an "island plus serpentine" design, the greater ductility offered by SMA substrates would allow the islands, on which the

sensitive components are housed, to remain largely strain-free for longer. Additionally, since SMAs need to be crystallized at temperatures above 400 °C, they could serve as the substrate to enable stretchability within MEMS materials that require high-temperature processing (e.g. semiconductors, piezoelectric devices) [19]. The excellent mechanical and electric properties of thin-film NiTi-based SMAs make them promising materials to use as interconnects and functional substrates for future wearable and implantable electronics.

5.6 Summary and Conclusions:

Wearable electronics and implantable medical devices require stretchable circuits which could be based on conductive serpentine structures. The results reported here demonstrate the mechanical advantages of replacing thin-film serpentine interconnects made from traditional metals like Cu with shape memory alloys such as TiNiCuCo. Since the martensitic transformation temperatures are below room temperature, all fabricated TiNiCuCo films demonstrate superelasticity at room temperature. Superelasticity is advantageous for stretchable interconnects because the interconnect will recover from the deformation after the removal of the applied force. FEA simulations reveal elastic serpentine elongations are significantly larger for TiNiCuCo thin-films as compared to Cu thin-films, which is attributed to the increase in intrinsic elastic strain characterized by the superelasic phase transformation in the SMAs. FEA simulations were experimentally verified by tensile testing as well as by detecting temperature changes within the regions of maximum strain concentration for a TiNiCuCo serpentine using infrared imaging.

Cu/TiNiCuCo/Cu serpentine composites were demonstrated to have a stable electrical resistance when stretching between serpentine elongations 0% - 45% which allowed them to serve

as freestanding electrical interconnects between two LEDs. All 20 μm thick TiNiCuCo serpentine interconnects were shown to have low electrical resistances (9 Ω - 22 Ω) which increased by less than 1% when elongated between 0% and 50%. The change in resistance was also used to monitor functional fatigue in the serpentine interconnects. Our results show electropolishing as a technique that can be used to improve the mechanical performance of thin-film SMA serpentines, as demonstrated by a stable hysteresis loop between cycle numbers ~8,000 and ~100,000 for an electropolished TiNiCuCo serpentine. Since TiNiCuCo is an ultralow-fatigue material, the SMA can theoretically undergo this transformation reversibly for up to 20 million cycles with proper control over the composition and microstructure. These results show the advantage of using sputtered thin-film SMAs as both freestanding substrates and serpentine interconnects in the design of future stretchable electronics.

Acknowledgments:

This work was supported by the German Research Foundation (Deutsche Forschungsgemeinschaft, DFG) through the special priority program KOMMMA (SPP 2206 - Cooperative Multistage Multistable Microactuator Systems). This material is based upon work supported by the National Science Foundation Graduate Research Fellowship Program under Grant No. DGE 1840340. Any opinions, findings, conclusions, or recommendations expressed in this material are those of the author(s) and do not necessarily reflect the views of the National Science Foundation. The authors thank Dr.-Ing. Prasanth Velvaluri (Kiel University) for assistance with sample fabrication, and Prof. Ichiro Takeuchi (University of Maryland) for discussions regarding the IR imaging experiments.

5.7 Appendix:

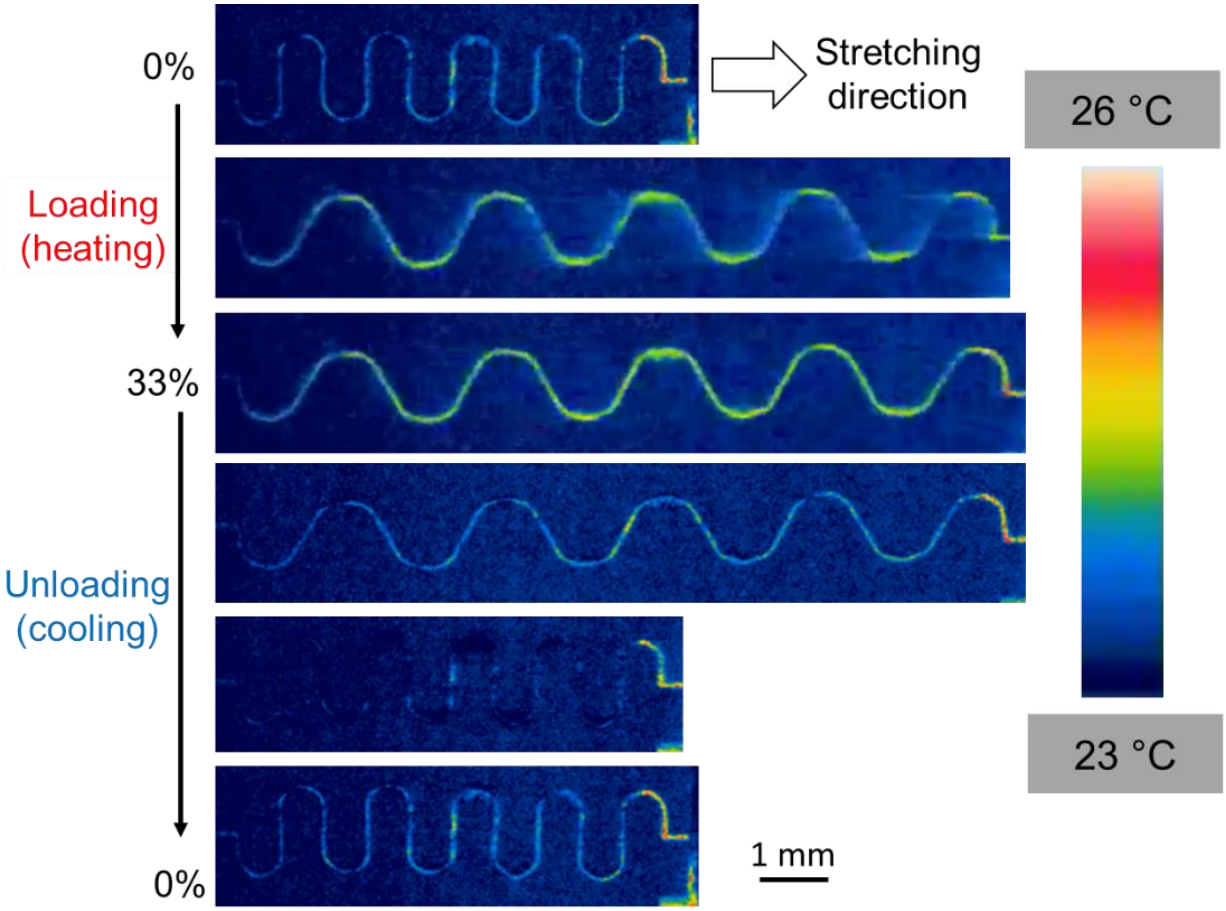

Figure 5.9: IR imaging results visualizing regions of maximum strain concentration via the regions of maximum temperature change during strain loading and unloading.

Chapter 6. Conference Proceedings: Auxetic Superelastic TiNiCuCo Sputtered Thin-Films for Stretchable Electronics

Own contributions to the following article[1].

- project idea conception- “thin-film SMA auxetics” (entire fraction)
- project idea conception – “stretchable auxetic geometries” (entire fraction)
- design and simulations of novel geometries (large fraction)
- sample fabrication (large fraction)
- differential scanning calorimetry (large fraction)
- tensile testing (large fraction)
- mechanical testing of novel geometries (large fraction)
- interpretation of the results (large fraction)
- writing of the conference proceedings paper (large fraction)

Chapter content expanded from:

S.M. Curtis, D. Dengiz, L. Bumke, and E. Quandt, (2022, May). “Auxetic Superelastic TiNiCuCo Sputtered Thin-Films For Stretchable Electronics.” *In SMST2022* (pp. 11-13). ASM International. https://doi.org/10.31399/asm.cp.smst2022p0011

[1] this page is required by regulations

Motivation:

The next generation of wearable and implantable medical devices requires the co-integration of several electronic components (i.e wires, sensors, antennas, and power devices) into a stretchable platform that allows the devices to survive extreme levels of flexing, stretching, twisting, and folding types of movement without fracture. In Chapter 5 of this doctoral thesis, I experimentally and numerically demonstrated the mechanical advantages of superelastic freestanding thin-film SMA films for stretchable interconnects compared to state-of-the-art Cu. Also in Chapter 5, I demonstrated that sputtered composite devices can be built by coating TiNiCuCo freestanding superelastic thin-films with other sputtered deposited materials (i.e. Cu). Cu/TiNiCuCo composites were demonstrated to combine the advantageous mechanical properties of the superelastic TiNiCuCo films with the excellent electronic properties of Cu thin-films.

The motivation for Chapter 6 is focused on the development of stretchable electronics for wearable and implantable medical devices using freestanding shape memory alloy substrates, structured into novel geometries. I call the novel structures “stretchable auxetic” geometries because they combine the properties of stretchable interconnects (e.g., serpentines and archimedean spirals) with the properties of traditional auxetic meta-mechanical materials (e.g., negative Poisson’s ratio). I show an example of the amorphous 2D stretchable auxetic SMA film shape set into 3D shapes (e.g. cylinders, semi-spheres) during crystallization with RTA. At the end of the chapter, I explain how the mechanical advantages of superelastic materials paired with the novel stretchable auxetic structures are advantageous for implantable medical device applications. This chapter expands on the results from a SMST 2022 conference presentation and conference proceedings paper (Carlsbad, CA, May 2022). These results also won 2nd place and People Choice Award at SMST 2023- SMArt Tank Competition (Fort Worth, TX, March 2023).

6.1 Introduction:

Auxetic shape memory alloy (SMA) materials offer many opportunities for ballistics [83], deployable antennas [84], actuators, stretchable electronics [208–210], and biomedical devices [211, 212]. Auxetic materials are periodic structures characterized by a negative Poisson's ratio, meaning they expand laterally (transverse strain) when stretched longitudinally (axial strain). Structures that have a negative Poisson's ratio are known to exhibit many seminal material properties including synclastic bending, high stiffness-to-weight ratio, high impact strength, reduced fatigue crack propagation, and vibration damping [75]. These properties make auxetic structures attractive for stretchable electronics applications that are intended to interface with 3D biological surfaces. Such wearable and implantable electronic systems are desired to have a large area density (e.g. regions for functional device integration) and must withstand large levels of physical deformation (i.e., elastic strains as large as 75% - 100%) [182, 183] without compromising the functional components of the device [211].

The major drawback of traditional auxetic structures is that the expandability and compressibility of the entire structure are limited by 1) the stiffness of the connecting hinges of the structures and 2) the mechanical properties of the material. The stiffness of traditional auxetic structures may limit their practical use as implantable medical devices, or for other wearable bioelectronic applications, as the stretchable requirements cannot be met with traditional designs. **Figure 6.1** shows scanning electron microscopy images of NiTi shape memory alloy thin-films structured into four traditional auxetic geometry designs (i.e. Design 1-rotating triangles, Design 2-S-shape auxetics, Design 3- rotating squares, Design 4-circular auxetics). All SMA traditional auxetic structures demonstrated a negative Poisson's ratio under applied uniaxial strain, with a maximum reversible uniaxial strain of up to 57.4% obtained [82]. The high stretchability and

negative Poisson's ratio paired with the additional stretchability of the SMA is one of the reasons why they can function well in applications requiring compacting the device into a small volume during the deployment (e.g., implants inserted with catheters) or stretchable electronic devices that require large area coverage (e.g., wearable biosensors) [82].

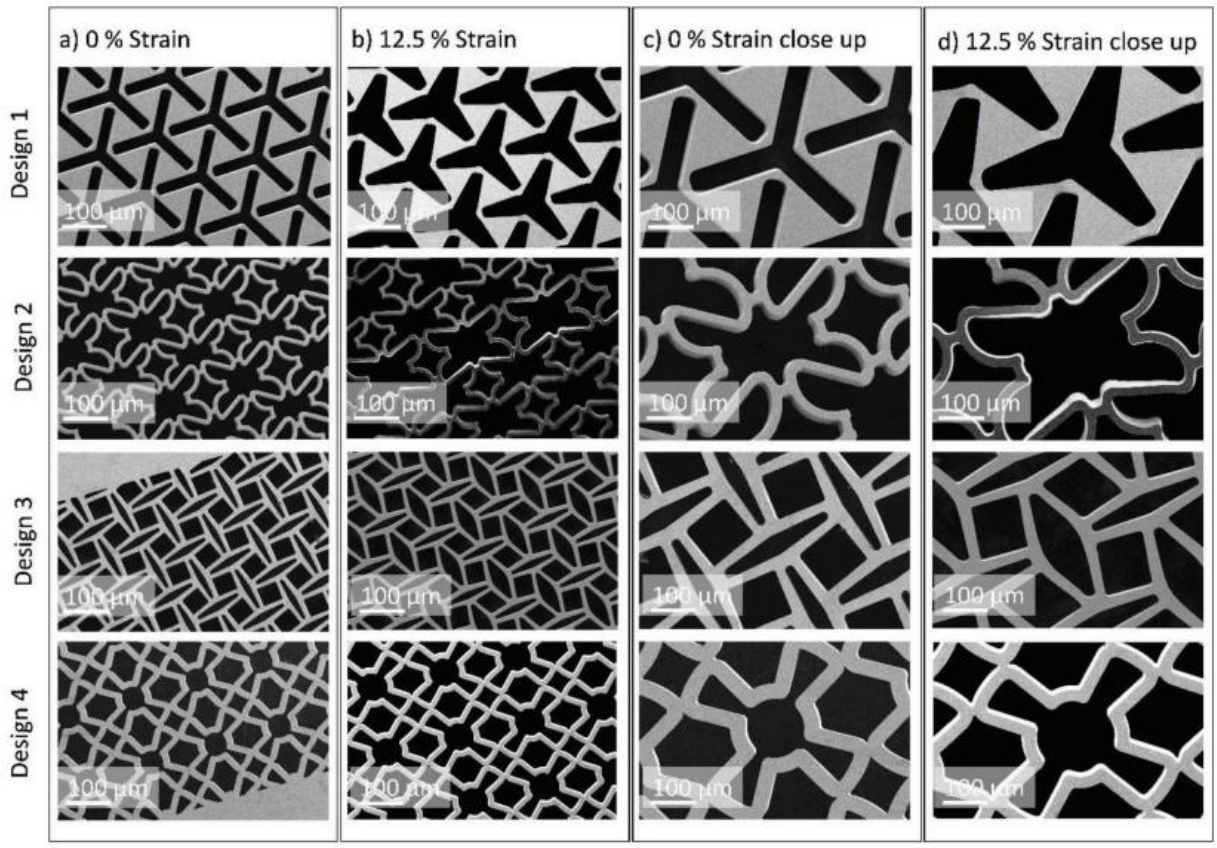

Figure 6.1: SEM images of four different designs for the NiTi auxetic arrayed structures. Design 1-rotating triangles, Design 2- s-shape auxetics, Design 3- rotating squares, Design 4- circular auxetics. Structures are shown at a) equilibrium (0% strain) and b) applied 12.5% uniaxial strain. Magnification of a single unit cell from the array at c) equilibrium (0% strain) and d) after 12.5% uniaxial strain. (*image reproduced from* [82]).

Traditional stretchable electronics can successfully co-integrate several electronic device components (e.g., wires, antennas, batteries, solar cells) into one stretchable device that can reach large levels of strain using "island-interconnect" structures [56, 57]. This method typically involves structuring the electronic components onto a series of periodic islands that are connected

at the center of the islands by thin-film stretchable interconnects (e.g., Cr, Au, or Cu.) Examples of stretchable interconnect geometries include serpentines [74, 209], fractal patterns, and archimedean spiral structures [60]. The stresses on the islands remain low even when the entire device is under applied flexing and stretching deformation because the stresses and strains are concentrated in the region of maximum curvature in the stretchable interconnections [60]. There are also some mechanical limitations to stretchable designs using the traditional "island-interconnect" due to the structure's positive (or zero) Poisson's ratio, which means under axial strain, the structure will undergo necking behavior. Structures with a positive or zero Poisson's ratio do not take advantage of the properties mentioned for auxetic structures. Additionally, traditional "island-interconnect" designs typically use materials that undergo plastic deformation (or fracture) at low intrinsic strains (< 1%) including metals like Cr or Cu for the stretchable interconnect and Si for the island to support MEMS devices. Typically the entire stretchable device must be integrated on an elastomer substrate to promote elastic recovery serpentine as well as provide protection to the electronic components [213].

Chapter 6 presents extremely deformation freestanding structures that take advantage of the mechanical properties of auxetic meta-mechanical materials, stretchable electronics, and sputtered superelastic SMA materials. The novel geometries presented in this work are based on the combination of the auxetic rotating rectangle structure (i,e. Design 3- **Figure 6.1**) [75] where the rotating hinges are replaced by two common stretchable interconnects (e.g. serpentines and archimedean spirals). These novel stretchable auxetic structures investigated in this chapter are called "rotating serpentine rectangle" and "rotating archimedean rectangle". The mechanical performance of TiNiCuCo was evaluated for 2D freestanding films structured into two-novel stretchable auxetic structures. Since the novel stretchable auxetic structures are fabricated from an

SMA, I also demonstrate that the 2D freestanding films can be shape-set into complicated 3D geometries. Since these structures are fabricated via layer-by-layer deposition and photolithography, other components, such as microelectronics, can be seamlessly integrated into the fabrication process, which is discussed further in Chapter 7.1 [82].

6.2 Experimental Methods, Results, and Discussion:

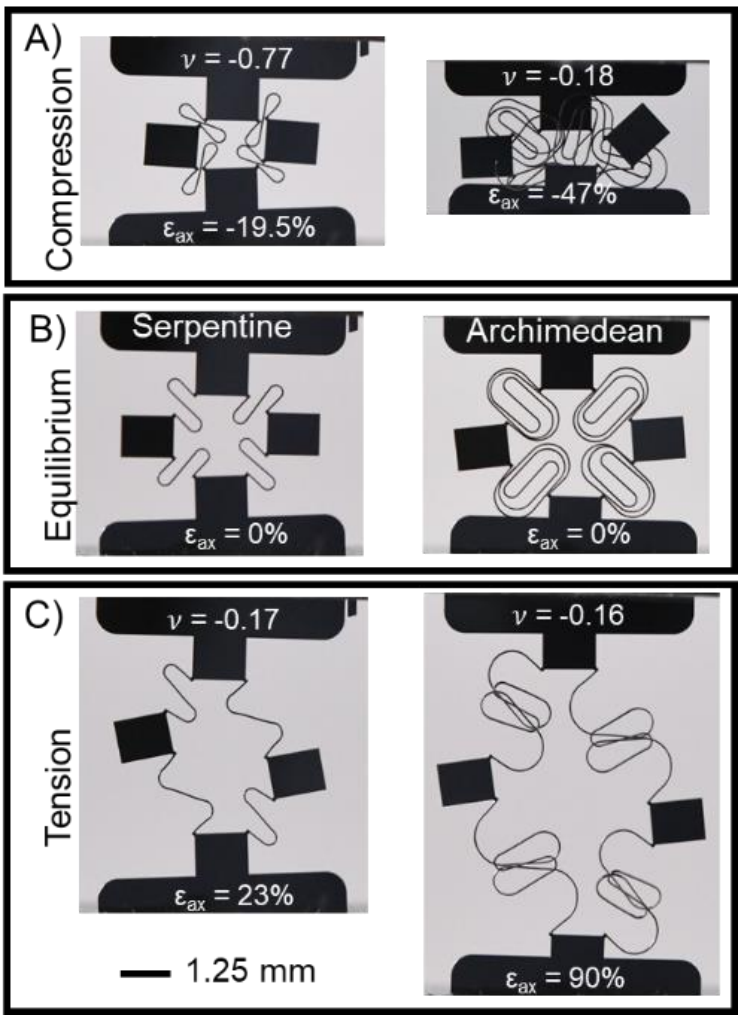

Figure 6.2: Superelastic and auxetic behavior of TiNiCuCo patterned into the novel "rotating serpentine rectangle" and "rotating archimedean rectangle" auxetic geometries. A) Demonstration of auxetic and superelastic behavior of the structures under compressive axial strain. B) SMA material in the austenite phase when structures are at equilibrium. C) Demonstration of auxetic and superelastic behavior while structures are stretched to large tensile axial strains, transforming the SMA material from austenite to the stress-induced martensite phase.

Superelastic recovery of large intrinsic strains in sputtered freestanding SMAs makes them attractive for use as stretchable interconnects [214] and as auxetic structures [82]. Previously TiNiCuCo was demonstrated to be an ultra-low fatigue SMA, able to transform reversibly to a superelastic strain of 2.5% for up to 2 x 10^7 cycles [18, 193]. *Lima de Miranda et al.* [11] developed a freestanding SMA fabrication process in 2013 that allows for the development of freestanding SMA films with film thicknesses between 10 μm – 80 μm, and allows the patterning of complex microstructures with feature sizes as small as 10 μm. This process was used to fabricate novel stretchable auxetic structures with amorphous TiNiCuCo freestanding films. These auxetic structures are called "rotating serpentine rectangle" and "rotating archimedean rectangle", referred to as the "serpentine" auxetic structure and "archimedean" auxetic structure in **Figure 6** and the text. The "unit cell" of the stretchable auxetic structures are shown at equilibrium in the austenite phase in **Figure 6.2B)**. The dimensions of the free islands in both geometries are 1.0 mm x 1.25 mm, and both structures had a TiNiCuCo film thickness of 53 μm. The archimedean spirals had a wavelength (λ) of 1.25 mm, peak-to-peak amplitude (A) = 2.2 mm, and width (w) = 50 μm. The serpentine interconnects had similar dimensions (λ = 1 mm, A = 1 mm, and w = 50 μm).

Axial strain is defined as $\frac{\Delta \boldsymbol{l}}{\boldsymbol{l}}$*100% where $\boldsymbol{l}$ is the initial end-to-end length of the stretchable auxetic device in the equilibrium length when the sample is in the austenite phase under no applied external force. $\Delta \boldsymbol{l}$ is the change in length of the stretchable auxetic device in the direction of the applied uniaxial force. Transverse strain is calculated similarly by measuring the change in the lateral width of the device (perpendicular to the direction of applied force). Poisson's ratio is the negative of the ratio of transverse strain to axial strain in the structure.

Figure 6.2A) shows the maximum negative Poisson's ratio obtained was -0.77 and -0.18 after applying axial compressive strains of -19.5 % and -47% to the serpentine and archimedean

structures, respectively. **Figure 6.2C)** shows the serpentine and archimedean structures still retain auxetic behavior under tension, with a Poisson's ratio of -0.17 and -0.16, when stretched to tensile axial strains of 23 % and 90 %, respectively. Since the structures are fabricated with a superelastic material, almost all deformation is recovered upon the removal of the compressive or tensile force, returning the structure to its equilibrium position.

2D mechanical testing of the unit cells demonstrated that they have enhanced expandability and compressibility compared to traditional auxetic structures. In 2019, *Meena et. al* introduced numerical and experimental results on an "S-shaped" auxetic structure that was shown to have reduced stress concentrations compared to "re-entrant" auxetic structures. The tested re-entrant auxetic structure was reported to lose its auxetic behavior after a 5% axial strain, while the S-shape auxetic could maintain an auxetic response with external axial strains of 15% [215]. The novel stretchable auxetic geometries I proposed in this chapter fabricated with TiNiCuCo SMAs were demonstrated to maintain auxetic behavior at axial strains as large as 23% for the serpentine structure and 90% for the archimedean structure, which is considerably larger tensile strains than reported in by *Meena et al.* Like the "S-shaped" auxetic structures, both the serpentine and archimedean structures demonstrated a change from negative Poisson's ratio to a positive (or zero) Poisson's ratio when stretched to larger tensile axial strains than the critical axial strain values given in **Figure 6.2C).** This behavior was also observed in thin-film SMA traditional auxetic structures tested in **Figure 6.1** [82].

The superelastic response of TiNiCuCo fabricated into a unit cell structure of the "rotating archimedean rectangle" auxetic geometry is shown via tensile testing results in **Figure 6.3A).** Tensile tests reveal that TiNiCuCo could reach extremely large external superelastic axial strains between -50% to 200 % macroscopic axial strain for 100 cycles with only minor functional fatigue.

The serpentine structure was also able to superelastically stretch between axial strains of -30 % to 50 % for 100 tested cycles with minor functional fatigue (unpublished research, not shown).

Numerical simulations with COMSOL Multiphysics 5.3 demonstrated that under applied deformation, all of the stress and strain concentrates in the stretchable interconnects, with little to no force on the islands. Simulation results revealed extremely low forces and thus low von Mises stresses were obtained along the archimedean spiral auxetic geometry compared to the serpentine auxetic geometry. As described in Chapter 5, the serpentine structure concentrates stress/ strain in the regions of maximum curvature change in the structure and thus is the corresponding region where the SMA material is transforming from austenite to stress-induced martensite. The archimedean spiral designs offer a considerable stress-reduction compared to the serpentine structures by offering more areas of curvature. The reduced stress concentration offered by the archimedean spiral geometry is attractive for stretchable applications requiring large stretchability levels [60].

While the archimedean spiral can deform significantly more than the serpentine, it comes at the cost of out-of-plane deformation. **Figure 6.3B)** shows the obvious out-of-plane deformation of the archimedean structure at a maximum tested axial strain of 265%. At this axial strain, the maximum macroscopic elongation achieved in the archimedean spirals is massive at over 450%. At an axial strain of 265%, the structure has a positive Poisson's ratio of 0.018. After the removal of the applied force that resulted in an axial strain of 265%, **Figure 6.3C)** shows the superelastic recovery of the structure with a relatively low amount of plastic strain (e.g. plastic axial strain of 3.75 %). According to FEA simulation results, Cu thin-films with the same dimensions as the novel archimedean auxetic structures can only elastically stretch by an axial strain of 15%, while

TiNiCuCo was experimentally shown to superelastically recover at least 200 % external axial strain[6].

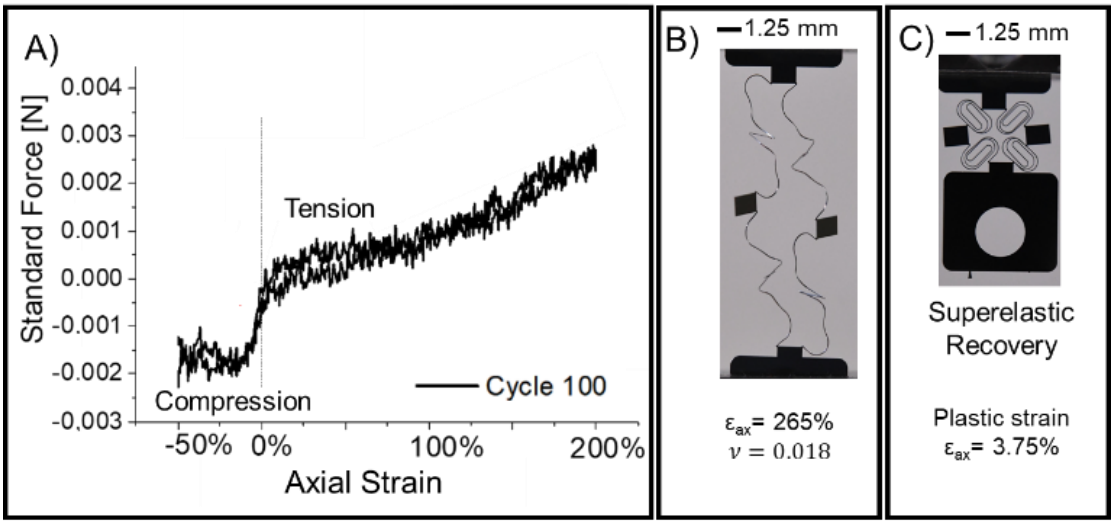

Figure 6.3: TiNiCuCo freestanding film patterned into a novel rotating archimedean rectangle auxetic unit cell geometry showing superelastic recovery of extremely large axial strains. A) Tensile testing showing superelastic recovery of extremely large compressive and tensile axial strains of -50 % to 200 %. Little functional fatigue was observed after repeating this experiment for 100 cycles. B) Structure under 265 % tensile axial strain with a slightly positive Poisson's ratio of 0.018. C) Demonstration of superelastic recovery of the structure to the equilibrium position after removal of 265% axial strain, demonstrating only 3.75 % plastic axial strain due to the build-up of remnant stress-induced martensite.

The geometrical parameters of the "rotating serpentine rectangle" and "rotating archimedean rectangle" unit cell structures were downscaled by a factor of 2 and arrayed (2x3) as shown at equilibrium in **Figure 6.4** (left-Equilibrium). The archimedean spirals had a wavelength (λ) of 0.625 mm, peak-to-peak amplitude (A) = 1.1 mm, and width (w) = 25 μm. The serpentine interconnects dimensions were (λ = 0.5 mm, A = 0.5 mm, and w = 25 μm). The arrayed structures in **Figure 6.4** (middle-Compressed and right-Expanded) demonstrate enhanced compressibility and expansion in arrayed serpentine and archimedean stretchable auxetic geometries. These stretchable auxetic structures can reach large levels of compressive axial strain, which makes them

attractive for crimpable medical devices intended to be deployed through endovascular treatment methods. Crimpability is an important design parameter for self-expanding SMA stent devices because mechanical deformation needs to be applied to the device to reduce its diameter so it's small enough to fit into a microcatheter [82]. Furthermore, FEA simulation results demonstrated that the islands in the arrayed structure undergo little stress under applied deformation. This means that the islands can serve as low-stress areas for sensor integration, similar to what is already done in traditional "island-interconnect" designs in stretchable electronics.

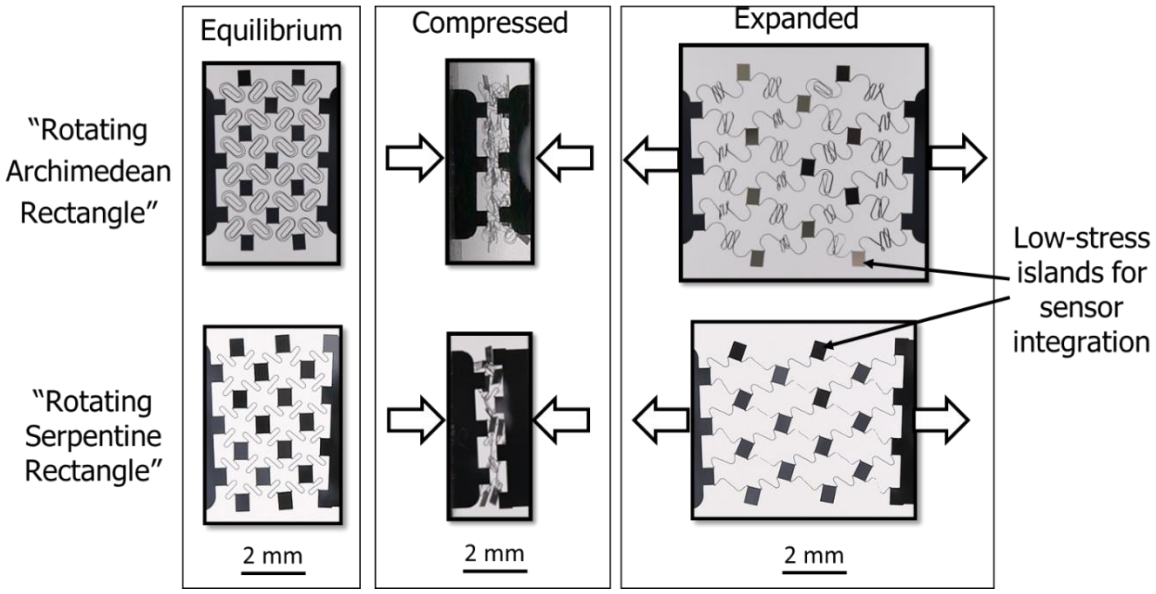

Figure 6.4: Demonstration of enhanced compressibility and expansion behavior in arrayed novel stretchable auxetic geometries. "rotating archimedean rectangle" and "rotating serpentine rectangle". (Left) Structures are shown at equilibrium in the austenite phase. (Middle) Structures are nearly fully compressed. (Right) Structures displaying auxetic behavior upon expansion to large tensile strains. During compression and expansion, the islands remain in the austenite phase while the stretchable interconnects are in the stress-induced martensite phase.

6.3 Stretchable Auxetic Films for Medical Applications

Binary NiTi is biocompatible, corrosion-resistant, and can be designed to self-expand at body temperature (37 °C) which leads it to be widely used in implantable medical devices like stents. The fabrication process developed by *Lima de Miranda* [29] allows the fabrication of 2D amorphous freestanding SMA film in the shape of a stent backbone. The 2D films can "remember" a 3D shape when heated to the austenite phase when the SMA film is annealed around a 3D object like a cylinder or a sphere made from Ti-metal. Researchers at Acquandas and Kiel University have used this additional fabrication step to develop implantable medical devices like flow diverter stents [216, 217]. This annealing method allows the SMA film to "remember" the necessary 3D shape of implantable medical devices such as stents. In 2015, *Bechtold et al.* shows that radiopaque materials (e.g., Au, Ta, Pt-Ir) can be deposited and structured onto the freestanding NiTi medical device using either a 2D or 2.5D process. They also proposed that this fabrication process could be used to deposit and isolate circuit paths onto freestanding NiTi structures so that certain areas of the device can be used as electrodes for stimulation, sensing, or mapping [13].

The superelastic effect allows recovery of strains up to 8% within biocompatible NiTi. When this material is microstructured and shape set into a 3D deformable geometry, the geometry paired with the superelastic effect allows the structured NiTi device to survive large amounts of crimping and expansion forces. Medical stent devices based on NiTi thin-films already take advantage of this combined principle by crimping down diameters as small as 2 mm to fit inside catheters to be deployed in the body through non-invasive endovascular treatment methods. Once the medical device has reached the intended location in the body, the catheter is removed, leaving behind the SMA stent device. The device can be designed to self-expand to the desired shape at

body temperature (37 °C) using the shape memory effect, or it can automatically expand upon removal of the catheter with the superelastic effect. Typical 3D shapes of SMA medical devices deployed through endovascular treatments include cylinders (e.g., stents) and semi-spheres (e.g., intrasacuular devices) [218].

The novel stretchable auxetic geometries I introduced in **Figure 6.2** can also be used to develop smart implantable medical devices. **Figure 6.5a)** shows an example of a 2D freestanding thin-film amorphous SMA structured into a "rotating serpentine rectangle" auxetic geometry. **Figures 6.5b) and 6.5c)** show an example of two complex 3D austenite shapes in the expanded state that can be developed by annealing the SMA thin film around 3D objects (semi-sphere and cylinder). Since the geometry also displays auxetic properties, the thin film can easily conform around any 3D curvature. The novel stretchable auxetic geometries I invented are advantageous for the development of smart implantable electronic medical devices like "Smart Stents", as shown in **Figure 6.5d)** [211]. The "rotating archimedean rectangle" structure shown is also able to adapt to complex 3D curvatures as well, as shown in **Figure 6.6** [211].

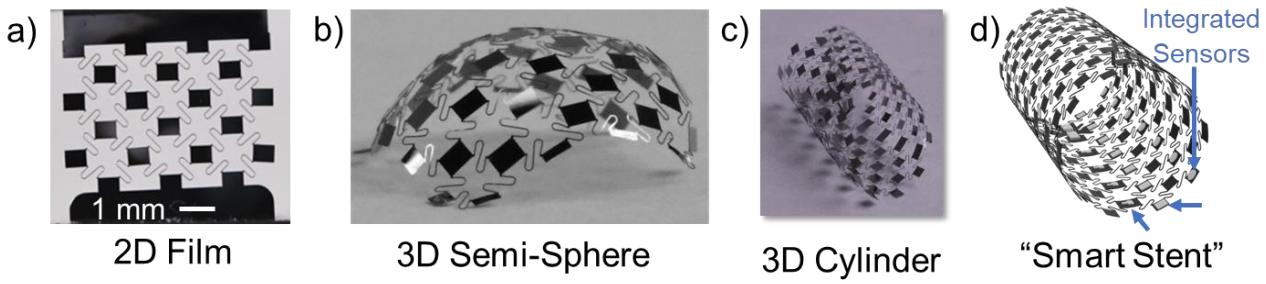

Figure 6.5: Demonstration of shape-setting 2D amorphous superelastic "rotating serpentine rectangle" auxetic arrayed structure into 3D semi-spherical and cylindrical shapes. a) As-fabricated 2D amorphous TiNiCuCo SMA thin-film. SMA thin film crystallized into two complex 3D shapes that could be used as implantable medical devices: b) semi-sphere and c) cylinder. d) Illustration of a "smart stent" with integrated sensors on the islands of the stent backbone. Dimensions of the rectangle islands are 0.625 mm x 0.5 mm.

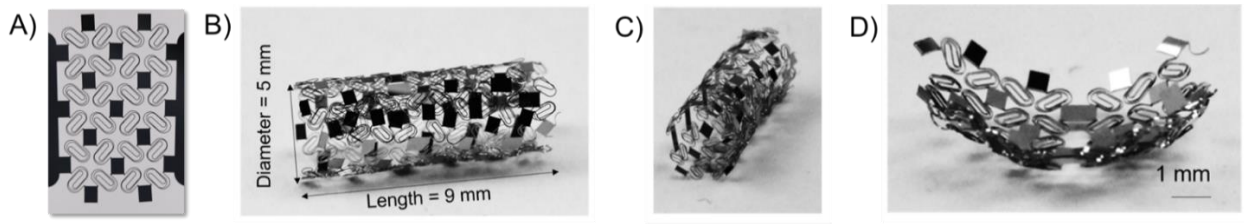

Figure 6.6: Demonstration of shape-setting 2D amorphous superelastic "rotating archimedean rectangle" auxetic arrayed structure into 3D semi-spherical and cylindrical shapes. a) As-fabricated 2D amorphous TiNiCuCo SMA thin-film. SMA thin film crystallized into two complex 3D shapes: b) and c) cylindrical stent shape with a radius of 5 mm and d) semi-spherical shape for intrasaccular devices. Dimensions of the rectangle islands are 0.625 mm x 0.5 mm.

The geometries I propose display enhanced expandability and compressibility in classical auxetic structures because all rigid connection points were replaced with stretchable serpentine and archimedean interconnects. The largest advantages offered by these structures under uniaxial stretching conditions are that the structures display a negative Poisson's ratio, they are ultra-stretchable, and they offer sizeable low-stress islands that are suitable to house any type of microelectromechanical systems (MEMS) component. The low-stress islands are a key feature that can allow the future co-integration of various electronic components (i.e battery, antenna, sensors, actuators, solar cells) through the structured substrate.

6.4 Conclusions:

The novel stretchable auxetic geometries "rotating archimedean rectangle" and "rotating serpentine rectangle" structures fabricated from superelastic TiNiCuCo can be used as substrates for stretchable electronics. Both structures are proven to be highly stretchable and retain auxetic behavior under large levels of external tensile and compressive strains. Under deformation, stress concentrates in the stretchable interconnect, while the islands undergo relatively low stresses. This

means the islands are available to further device integration. The MEMS-compatible fabrication process developed by *Lima de Miranda et al.* could allow future monolithic integration of functional MEMS components onto the islands of the superelastic stretchable auxetic substrates. The use of superelastic SMA materials as the substrate might eliminate the need to integrate stretchable MEMS devices onto elastomer substrates in the future.

6.5 Acknowledgements

S.M. Curtis gratefully acknowledges support from the National Science Foundation Graduate Research Fellowship under Grant No. DGE 1840340. This research has received funding from the German Research Foundation (DFG) within the priority program "SPP2206–Cooperative Multistage Multistable Microactuator Systems". S.M. Curtis gratefully acknowledges the support on this project from colleagues at Kiel University including M.Sc. Lars Bumke and Dr.-Ing. Prasanth Velvaluri. S.M. Curtis also would like to thank Bobby Cozzette for his preliminary experiments on the "rotating serpentine rectangle" auxetic structure using 3D printed polymers.

To the best of my knowledge, I was the first researcher to investigate auxetic thin-film SMAs. The foundation of this work was included in my 2018 NSF GRFP Grant (No. DGE 1840340). I mentored M.Sc. Duygu Dengiz on this topic for 4 years in Kiel. Additional information regarding auxetic shape memory alloy thin-films can be found in the co-authored journal paper below.

Dengiz, D., Goldbeck, H., **Curtis, S.M.,** Bumke, L., Jetter, J. and Quandt, E. (2023) Shape Memory Alloy Thin Film Auxetic Structures. *Advanced Materials Technology* 2201991: 1-9. *Invited Paper*, https://doi.org/10.1002/admt.202201991

Chapter 7. Summary and Outlook

This doctoral thesis discussed the results of three peer reviewed, co-authored papers focused on the integration of three different sputtered thin-film SMAs into three novel MEMS applications: TiNiCu for magnetoelectric sensors, TiNiHf for bistable actuators, and TiNiCuCo for stretchable electronics. In Chapters 3 and 4 of this thesis, I explained how the *shape memory effect* enables bimorph SMA/Si film composites to be used in MEMS and NEMS devices like sensors and actuators. In Chapter 5 of this thesis, I showed the first results of the *superelastic effect* in freestanding, micropatterned, thin-film SMAs for use as stretchable interconnects. In Chapter 6, I expanded on results presented in a co-authored, conference proceedings paper that introduced novel stretchable auxetic geometries as new structures for stretchable electronics. I show that freestanding TiNiCuCo films patterned into these novel geometries could be used as substrates for functional wearable and implantable medical devices.

This doctoral thesis primarily investigated the material properties of micro and nano structured SMA thin-films. In each publication, I characterized the functional material properties of each SMA thin-film in the context of their intended MEMS application (i.e., sensors, actuators, and stretchable electronics). All amorphous TiNiCu, TiNiHf, and TiNiCuCo SMA thin-films investigated in these works were deposited using DC magnetron sputtering at low-temperatures. Depending on the fabrication sequence used, amorphous freestanding SMAs with thicknesses between 5 μm – 80 μm were fabricated into custom-geometries with lateral feature sizes as small as 10 μm. Amorphous 2D thin-film SMAs with thicknesses between 10 nm – 10 μm were also deposited and micro-structured onto silicon substrates. To induce the *shape memory* or *superelastic effect*, all samples fabricated in this thesis were subsequently crystallized with rapid thermal annealing (RTA) to set the “remembered” 2D or 3D macroscopic shape of the film.

Optimization of the annealing parameters to control the SMAs microstructure (e.g., precipitate homogeneity, grain size) was essential as the microstructure is known to be directly related to its structural and functional fatigue performance.

I demonstrated in my doctoral thesis several fabrication schemes that could be used to develop MEMS devices with sputtered SMA thin-film materials. The fabrication schemes I presented for sensor, actuator, and stretchable interconnect development with SMAs could be combined in the future to create novel MEMS devices based on SMA thin-films. **Chapter 7.1** discusses the outlook for auxetic SMA substrates including piezoelectric/shape memory composites for applications like wearable energy harvesters. **Chapter 7.2** discusses the development of bistable and bi-directional actuators on the microscale and nanoscale using high-temperature TiNiHf SMA thin-films.

7.1 Outlook for Auxetic SMA Thin-Films

Röbisch et al. demonstrated that a high sensitivity and low limit of detection were obtained when the magnetostrictive and piezoelectric layers of the magnetoelectric sensor were directly deposited onto a freestanding shape memory alloy cantilever. Inspired by this work, Chapter 3 presented the first work of my doctoral thesis which studied SMA/piezoelectric (TiNiCu/AlN) composites on silicon substrates for magnetoelectric sensor applications. Through analytical calculations, I demonstrated that the change in Young's modulus between the austenite and martensite phases in a NiTi film can be used to tune the mechanical resonance frequency of a magnetoelectric sensor composite. I also developed a microfabrication process that allows the integration of TiNiCu thin-films into a magnetoelectric sensor composite (i.e AlN/TiNiCu/Si/FeCoSiB). Characterization results demonstrate that aluminum nitride (AlN) has excellent piezoelectric characteristics when deposited on top TiNiCu film on a Si substrate.

Figure 7.1 presents my prediction of future research directions of thin-film SMA stretchable auxetic films. The structured SMA itself could serve as a stretchable electrode. There are several examples in the literature of SMA/ piezoelectric composite systems for low and medium-frequency thermal energy harvesting [219–221], reversible actuation of bistable composites [222], and improving the multifunctionality of magnetoelectric sensors [19, 97, 223]. All of these types of devices could be downscaled to micro and nano dimensions using sputtered SMA/ piezoelectric composites. Using the methods developed by *Lima de Miranda*, one can microstructure and crystallize a freestanding SMA substrate into any custom geometry (e.g., traditional/stretchable/flexible) to meet the application's need, prior to piezoelectric deposition.

Figure 7.1a) demonstrates a 20 μm thick TiNiCuCo film structured into another novel stretchable auxetic geometry, called a "rotating serpentine triangle". This structure is based on a rotating triangle auxetic structure, connected by serpentine stretchable interconnects, and has a larger area coverage compared to the stretchable auxetic geometries introduced in Chapter 6. The substrate is in the austenite phase at equilibrium. **Figure 7.1b)** displays the simultaneous stretchable and auxetic properties of pure TiNiCuCo substrate by bending the 2D substrate around a 3D ball with a radius of curvature of 2 mm. The substrate shows synclastic (conformal) double bending around the ball, confirming the auxetic properties of the geometry. This feature of the substrate is attractive for wearable electronic devices that are intended to adapt to the various curvature changes of the human body. Since the SMA film is superelastic at room temperature, all deformation was recovered to the substrate after deforming the 2D film around the 3D ball.

The crystallized 20 μm TiNiCuCo film shown in **Figure 7.1a)** was sputtered deposited with 2 μm piezoelectric AlN. **Figure 7.1c)** displays an optical micrograph of an AlN/TiNiCuCo composite. The large difference in linear coefficient of thermal expansion (CTE, α) between the piezoelectric layer AlN (α = 4.15 x 10^{-6}/°K – 5.27 x 10^{-6}/°K [224]) and the NiTi thin-film ($\alpha_{martensite}$ = 6.5 x 10^{-6}/°K , $\alpha_{austensite}$ = 11 x 10^{-6}/°K [48]) creates a large reversible bending stress in sputtered bimorph composites which can be exploited for actuators or energy harvesting applications. Structuring piezoelectric materials into stretchable geometries (i.e, serpentine ribbon) was stated to be attractive for adding sensing and energy harvesting capability to wearable and implantable soft electronics [225]. Therefore, I believe freestanding SMA/piezoelectric composites structured into the novel stretchable auxetic geometries I proposed in this thesis might be a method to create wearable and implantable energy harvesting systems and sensor systems. These types of technologies might also be useful for structural health monitoring.

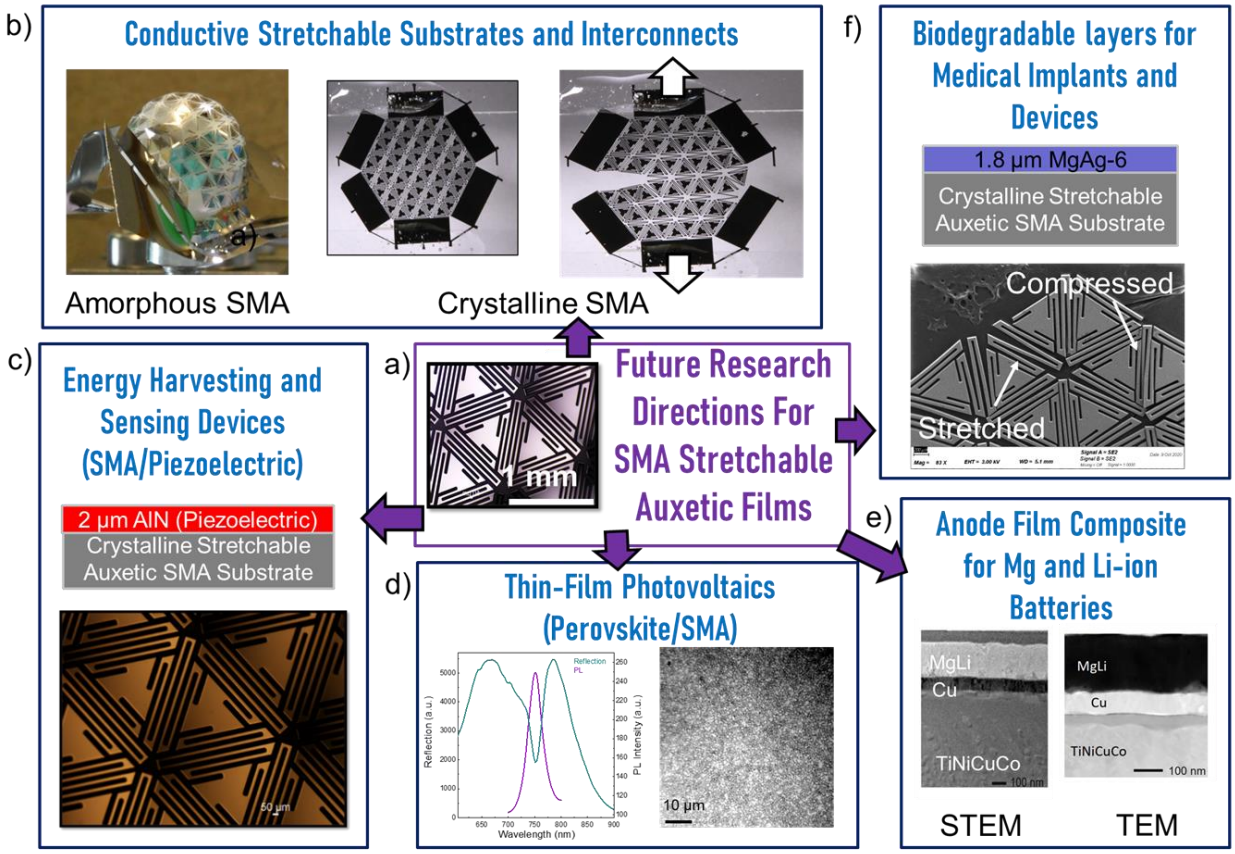

Figure 7.1: a) Prediction of future research directions of thin-film SMA stretchable auxetic films. b) Conductive stretchable interconnects and substrates for stretchable electronics that require high fatigue life or high applied strain values. c) Piezoelectric/ SMA bimorph composites can be used in energy harvesting and sensing devices. d) Structured crystalline SMA coated into 500 nm of perovskite photovoltaic material. f) Biocompatible SMAs can be coated in biodegradable thin-films (e.g. Mg, MgAg) for drug delivery. SEM image showing MgAg/TiNiCuCo locally stretching and compressing under applied deformation with no observable cracking. e) Sputtered thin-films used for development of power and storage devices can be coated conformally onto structured SMA substrate. Examples shown is TEM and SEM images of Cu current collector and MgLi thin-film deposited onto the SMA substrate. This composite configuration could be used as the current collector and anode for solid-state batteries.

Acknowledgements for Figure 7.1: M.Sc. Hanna Lewitz for piezoelectric depositions, Dr. Beth Tennyson for perovskite deposition and characterization, M.Sc. Lisa Hanke for MgLi and MgAg depositions as well as SEM imaging, Dr. Niklas Wulff for TEM imaging, and Dr. Haotian Wang for the solid-state battery collaboration.

Since the bimorph composite were fabricated by sputtering the functional piezoelectric material on top of the structured SMA substrate, this same concept can be used to develop other types of stretchable and flexible microelectronic systems. For example, active photovoltaic materials (e.g., perovskite solar cells) can be evaporated on top of the substrate (**Figure 7.1d**). Mg-based thin-films (e.g., MgLi and MgAg) could serve as functional coatings on the SMA for medical applications like drug-delivery (**Figure 7.1e**). All-solid-state batteries that are fabricated by sputter deposition could also become stretchable if sputtered onto a structured freestanding SMA substrate (**Figure 7.1f**).

7.2 TiNiHf for Nanoscale Bi-Directional and Bistable Actuators:

The second project of my Ph.D. was focused on the development of TiNiHf/Si bimorph composites for use in nanoscale bidirectional and bistable actuators. Chapter 4 described the combined shape memory effect and bimorph effect in TiNiHf/Si composites enabled their use as bidirectional thermal actuators on the micro and nanoscale. In this publication, we also described how to develop bistable actuators using trimorph PMMA/TiNiHf/Si composites. The most important condition that enables bistability within this trimorph composite is that the glass transition temperature (T_g) of PMMA falls within the thermal hysteresis of the TiNiHf SMA ($M_s < T_g < A_s$, see **Figure 4.7**).

In order to reliably fulfill the condition for bistability the austenitic transformation temperatures of TiNiHf films of nanoscale thicknesses should be shifted to temperatures much larger than the T_g of PMMA ($T_g = 105$ °C). Experiments conducted during my doctoral thesis showed that depositing and crystallizing TiNiHf layers onto buffer layers (e.g. SiO_2, Si_3N_4, Ta, Pt, and Cr) on Si substrates is a promising method to preserve the high-temperature transformation

temperatures of TiNiHf films. Experimental results demonstrated that downscaling TiNiHf film thickness from the micro to nanoscale reduced their characteristic transformation temperatures. The thickness at which TiNiHf no longer displayed appropriate transformation temperatures suitable for bistability was dependent on the buffer layer. For pure Si substrates, the critical thickness lies for TiNiHf films between 440 nm and 220 nm, while for Si substrates with 1.5 μm SiO_2 buffer layer, the critical thickness lies between 220 nm and 110 nm. The high transformation temperatures (A_f > 100 °C) and wide thermal hysteresis (ΔT > 50 °C) of 220 nm TiNiHf films on SiO_2/Si substrates and 440 nm TiNiHf films on Si substrates present opportunities in the development of nanoscale bi-directional and bistable actuators.

Controlling functional fatigue characteristics upon thermal cycling TiNiHf thin films remains one of the largest challenges in their reliable use as micro and nanoscale actuators with TiNiHf/Si bimorph composites. The functional and structural fatigue properties in TiNiHf can be controlled by composition and microstructure (grain size, precipitate size, precipitate homogeneity) which is dependent on annealing conditions [39, 135]. As described in our most recent publication [20], sputtered TiNiHf/SiO_2/Si bimorph composites suffered from functional fatigue with thermal cycling. Bi-directional and bistable SMA-based micro and nano actuators ideally should last for thousands of actuation cycles with little functional fatigue. The wide thermal hysteresis of > ΔT = 50 °C indicates poor crystallographic compatibility between the martensite and austenite phase for the fabricated TiNiHf alloy [47]. Temperature-dependent x-ray diffraction and cantilever deflection measurements also demonstrated the thermal hysteresis width was reduced for TiNiHf films constrained by SiO_2 and Si substrates compared to freestanding films of similar thicknesses. This might imply an improvement in the crystallographic compatibility between the austenite and martensite phases [47, 142] when the TiNiHf nanoscale film is

constrained by a substrate, compared to freestanding films. As described in Chapter 2.4 and Chapter 4, TiNiHf freestanding films and TiNiHf/Si bimorph composites using TiNiHf thicknesses larger than 1 μm could be annealed with essentially any RTA parameters. However, when TiNiHf is downscaled to nanoscale thicknesses, the only annealing condition that was reliable for nanoscale bimorph composites was 635 °C – 5 min, thus the ability to tune the microstructure is limited in TiNiHf/Si bimorph composites. Heat treatments at higher temperatures for longer amounts of time resulted in film delamination of ultra-thin TiNiHf films (thicknesses lower than 440 nm) off Si, SiO_2/Si, and silicon-on-insulator substrates.

This research project was a part of Phase 1 in the Deutsche Forschungsgemeinschaft (DFG) Special Priority Program (SPP 2206 - Cooperative Multistage Multistable Microactuator Systems). The methods and materials developed during my doctoral thesis research will be used Phase 2 of SPP 2206, scheduled to take place between 2022-2025. **Figure 7.2** demonstrates a scanning electron microscopy image of a fabricated 440 nm TiNiHf/ 2 μm Si microactuator using a silicon-on-insulator wafer using the TiNiHf materials parameters I developed during Phase 1 of this project. This device was fabricated and imaged by Ph.D. candidate, M.Sc. Gowtham Arivanandhan, in the group of Prof. Manfred Kohl at Karlsruhe Institute of Technology (KIT). The characterization results of this microactuator are included in the manuscript "G. Arivanandhan, Z. Li, **SM. Curtis** et. al, Power Optimization of TiNiHf/Si Shape Memory Microactuators, *Actuators* (2023), 12(2), 82; https://doi.org/10.3390/act12020082." The goal of Phase 2 of SPP 2206 is to develop nanoscale bi-directional actuators with TiNiHf/Si bimorph composites and nanoscale bistable actuators using PMMA/TiNiHf/Si trimorph composites using the methods developed in Phase 1 of this project.

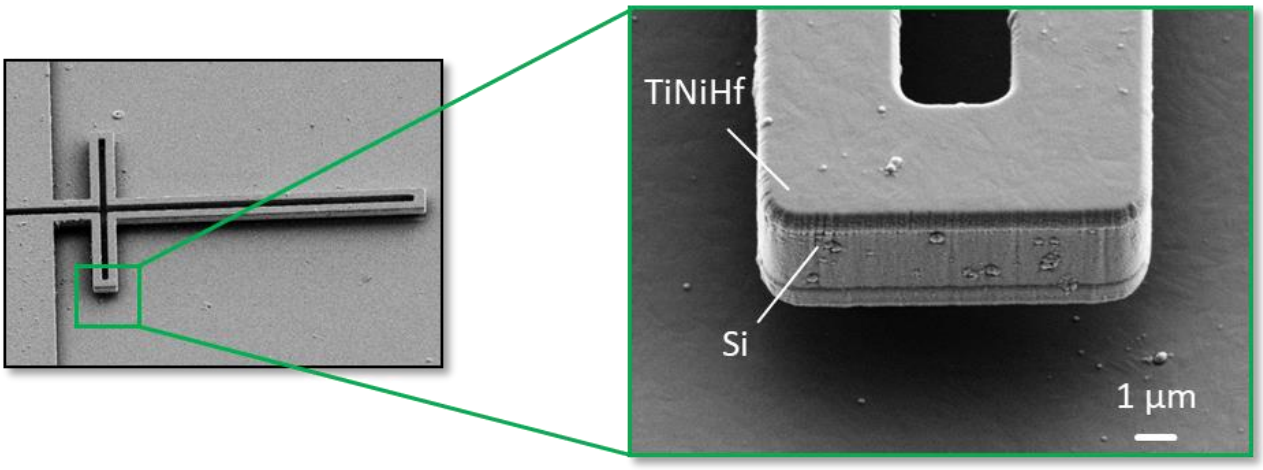

Figure 7.2: Scanning electron micrographs of a released TiNiHf /Si microactuator with folded beam structure for temperature homogenization. The thicknesses of the TiNiHf film and Si layer are 440 nm and 2 µm, respectively. Dimensions of cantilever beams: 75 µm length (*l*), 3 µm width (w) and 30 µm length of folded beam structure (l_{wing}). *Image from G. Arivanandhan at KIT and ref* [226]*)*

Chapter 8. Products of This Doctoral Research

8.1 Full List of Publications Accomplished During Doctorate

- **Curtis, S.M.,** Gugat, J.L., Bumke, L., Dengiz, D., Seigner, L., Schmadel, D., Lazarus, N.S., and Quandt, E., (2023) Thin-Film Superelastic Alloys for Stretchable Electronics. *Shape Memory and Superelasticity, pp. 1-15 Invited Feature Paper,* https://doi.org/10.1007/s40830-023-00422-4

- Arivanandhan, G., Li, Z., **Curtis, S.M.,** Hanke, L., Quandt, E., and Kohl M., (2023) Power Optimization of TiNiHf/Si Shape Memory Microactuators. *Actuators.* Vol. 12. No. 2. MDPI, https://doi.org/10.3390/act12020082

- Dengiz, D., Goldbeck, H., **Curtis, S.M.**, Bumke, L., Jetter, J. and Quandt, E. (2023) Shape Memory Alloy Thin Film Auxetic Structures. *Advanced Materials Technology* 2201991. *Invited Paper,* https://doi.org/10.1002/admt.202201991

- **Curtis, S.M.,** Sielenkämper, M., Arivanandhan, G., Dengiz, D., Li, Z., Jetter, J., Hanke, L., Bumke, L., Quandt, E., Wulfinghoff, S. and Kohl, M., (2022) TiNiHf/SiO_2/Si shape memory film composites for bi-directional micro actuation. *International Journal of Smart and Nano Materials*, *13*(2), pp.293-314. https://doi.org/10.1080/19475411.2022.2071352

- **Curtis, S.M.,** Dengiz, D., Velvaluri, P., Bumke, L., Quandt, E., Sielenkämper, M., Wulfinghoff, S., Arivanandhan, G., Li, Z. and Kohl, M., (2022, May) Bistable Actuators Based on Shape Memory Alloy/Polymer Composites. *In SMST2022* (pp. 1-3). ASM International. https://doi.org/10.1080/19475411.2022.2071352

- **Curtis, S.M.,** Dengiz, D., Bumke, L. and Quandt, E., (2022, May). Auxetic Superelastic TiNiCuCo Sputtered Thin-Films For Stretchable Electronics. In *SMST2022* (pp. 11-13). ASM International, https://doi.org/10.31399/asm.cp.smst2022p0011

- Arivanandhan, G., Li, Z., **Curtis, S.,** Velvaluri, P., Quandt, E. and Kohl, M., (2020) Temperature Homogenization of Co-Integrated Shape Memory—Silicon Bimorph Actuators. *Multidisciplinary Digital Publishing Institute Proceedings*, *64*(1), p.8. https://doi.org/10.3390/IeCAT2020-08501

- **Curtis, S.M.,** Wolff, N., Dengiz, D., Lewitz, H., Jetter, J., Bumke, L., Hayes, P., Yarar, E., Thormählen, L., Kienle, L. and Meyners, D., (2020) Integration of AlN piezoelectric thin films on ultralow fatigue TiNiCu shape memory alloys. *Journal of Materials Research*, *35*(10), pp.1298-1306. *Invited Feature Paper,* https://doi.org/10.1557/jmr.2020.106

- **Curtis, S.M.,** Tompkins, R.P., Nichols, B.M., Graziano, M.B., Kierzewski, I., Smith, G., Leite, M.S. and Lazarus, N., (2019) Structural Anisotropy in Stretchable Silicon. *Advanced Electronic Materials*, *5*(7), p.1900003. https://doi.org/10.1002/aelm.201900003

- **Curtis, S.M.,** Dengiz, D., and Quandt, E. "AUXETISCHE STEG- ODER FELDSTRUKTUR SOWIE VERWENDUNG" Patent Application No. PCT/DE2022/100001 (2022)

8.2 Conference Presentations and Posters

- **S.M. Curtis**, et al, "SMArt Stents" Oral Presentation at Shape Memory and Superelastic Technology (SMST) Entrepreneurial Workshop SMArt Tank Pitch Competition (Fort Worth, TX) (03/2023). *Second Place and People's Choice Award*

- **S.M. Curtis**, et al., **"**Auxetic Superelastic TiNiCuCo Sputtered Thin-Films For Stretchable Electronics" Oral Presentation at SMST 2022 (Carlsbad, CA) (05/2022)

- **S.M. Curtis**, et al., **"**Bistable Actuators Based on Shape Memory Alloy/ Polymer Composites" Oral Presentation at SMST 2022 (Carlsbad, CA) (05/2022)

- **S.M. Curtis**, et al., **"**Stretchable Shape Memory Alloy Thin-Films For Bioelectronics" Poster Presentation at Spring Materials Research Society 2022 (Honolulu, HI) (05/2022)

- **S.M. Curtis**, et al., "TiNiCu Thin-Film Shape Memory Alloy Substrates for Tunable Resonant Frequency Magnetoelectric Sensors" Oral Presentation Materials Research Society (MRS) Fall 2019 (Boston, MA) (12/2019)

- **S.M. Curtis**, et al., "Superelastic Sputtered TiNiCuCo Thin Film Serpentine Interconnects for Wearable Electronics" Oral Presentation at Fall MRS 2019 (Boston, MA) (12/2019)

- **S.M. Curtis**, et al., "Frequency Tunable Magnetoelectric Sensors on Shape Memory Alloy Substrates" Oral Presentation at 4th Euro Intelligent Materials 2019 (Kiel, Germany) (06/2019)

- **S.M. Curtis**, et al., "Multifunctional Sputtered NiTi Thin Film Stretchable Electrodes for Wearable Electronics" Oral Presentation at SMST (Konstanz, Germany) (05/2019)

Bibliography

1. Choudhary N, Kaur D (2016) Shape memory alloy thin films and heterostructures for MEMS applications: A review. Sensors and Actuators A: Physical 242:162–181
2. DesRoches R, McCormick J, Delemont M (2004) Cyclic properties of superelastic shape memory alloy wires and bars. Journal of Structural Engineering 130:38–46
3. Kohl M (2004) Shape memory microactuators. Springer Science & Business Media
4. Wang T-M, Shi Z-Y, Liu D, et al (2012) An accurately controlled antagonistic shape memory alloy actuator with self-sensing. Sensors 12:7682–7700
5. Hou H, Qian S, Takeuchi I (2022) Materials, physics and systems for multicaloric cooling. Nature Reviews Materials 1–20
6. Arivanandhan G, Li Z, Curtis S, et al (2020) Temperature Homogenization of Co-Integrated Shape Memory—Silicon Bimorph Actuators. In: Multidisciplinary Digital Publishing Institute Proceedings. p 8
7. Lambrecht F, Lay C, Aseguinolaza IR, et al (2016) NiMnGa/Si shape memory bimorph nanoactuation. Shape Memory and Superelasticity 2:347–359
8. Miyazaki S, Fu YQ, Huang WM (2009) Thin film shape memory alloys: fundamentals and device applications. Cambridge University Press
9. Li Z, Arivanandhan G, Rastjoo S, et al (2021) Development of Co-Integrated Shape Memory Actuators for Silicon Micro-and Nanomechanics. In: ACTUATOR; International Conference and Exhibition on New Actuator Systems and Applications 2021. pp 1–2
10. Knick CR, Smith GL, Morris CJ, Bruck HA (2019) Rapid and low power laser actuation of sputter-deposited NiTi shape memory alloy (SMA) MEMS thermal bimorph actuators. Sensors and Actuators A: Physical 291:48–57
11. de Miranda R, Zamponi C, Quandt E (2013) Micropatterned freestanding superelastic TiNi films. Advanced Engineering Materials 15:66–69
12. Bechtold C, de Miranda R, Quandt E (2015) Capability of sputtered micro-patterned NiTi thick films. Shape Memory and Superelasticity 1:286–293
13. Kumar A, Sharma SK, Bysakh S, et al (2010) Effect of substrate and annealing temperatures on mechanical properties of Ti-rich NiTi films. Journal of materials science & Technology 26:961–966
14. Morgan NB, Friend CM (2001) A review of shape memory stability in NiTi alloys. Le Journal de Physique IV 11:Pr8--325
15. Bechtold C, Chluba C, Zamponi C, et al (2019) Fabrication and Characterization of Freestanding NiTi Based Thin Film Materials for Shape Memory Micro-actuator Applications. Shape Memory and Superelasticity 5:327–335

16. Velvaluri P, Pravdivtseva MS, de Miranda RL, et al (2019) Design characterization of thin film flow diverter stents (FDS) based on SMA's: FEA, CFD and MRI study. Shape Memory and Superelasticity 5:195–205

17. Chluba C, Siemsen K, Bechtold C, et al (2020) Microfabricated bioelectrodes on self-expandable NiTi thin film devices for implants and diagnostic instruments. Biosensors and Bioelectronics 153:112034

18. Chluba C, Ge W, de Miranda RL, et al (2015) Ultralow-fatigue shape memory alloy films. Science 348:1004–1007

19. Curtis SM, Wolff N, Dengiz D, et al (2020) Integration of AlN piezoelectric thin films on ultralow fatigue TiNiCu shape memory alloys. Journal of Materials Research 35:1298–1306

20. Curtis SM, Sielenkämper M, Arivanandhan G, et al (2022) TiNiHf/SiO2/Si Shape Memory Film Composites for Bi-Directional Micro Actuation. International Journal of Smart and Nano Materials 13:293–314

21. Curtis SM, Dengiz D, Bumke L, Quandt E (2022) Auxetic Superelastic TiNiCuCo Sputtered Thin-Films For Stretchable Electronics. In: SMST2022. pp 11–13

22. Winzek B, Sterzl T, Rumpf H, et al (2002) Thin film shape memory composites. In: Nato Conference on Martensitic Phase Transformation, Metz, Frankreich

23. Winzek B, Sterzl T, Quandt E (2001) Bistable thin film composites with TiHfNi-shape memory alloys. Transducers 01 Eurosensors XV. Springer, pp 706–709

24. Taya M, Liang Y, Namli OC, et al (2013) Design of two-way reversible bending actuator based on a shape memory alloy/shape memory polymer composite. Smart materials and structures 22:105003

25. Sterzl T, Winzek B, Rumpf H, Quandt E (2002) Bistable shape memory composites for switches, grippers and adjustable capacitors. In: Proceedings of the 8th International Conference on New Actuators, Actuator. pp 91–94

26. Winzek B, Sterzl T, Rumpf H, Quandt E (2002) Smart motion control by phase-coupled shape memory composites. In: IEEE/RSJ International Conference on Intelligent Robots and Systems. pp 2004–2009

27. Grima J, Andrew A, Evans KE (2004) Negative Poisson's ratios from rotating rectangles. Cmst 10:137–145

28. Otsuka K, Ren X (2005) Physical metallurgy of Ti--Ni-based shape memory alloys. Progress in materials science 50:511–678

29. Lima De Miranda R, Zamponi C, Quandt E (2013) Micropatterned freestanding superelastic TiNi films. Advanced Engineering Materials 15:66–69. https://doi.org/10.1002/adem.201200197

30. Kumar SS, Arohi AC, Sen I (2022) A Review on Micro-mechanical Testing of NiTi-Based Shape Memory Alloys. Journal of the Indian Institute of Science 1–25

31. Ring TA, Feeney P, Boldridge D, et al (2007) Brittle and ductile fracture mechanics analysis of surface damage caused during CMP. Journal of The Electrochemical Society 154:H239

32. Gugat JL, Bechtold C, Chluba C, et al (2020) High-Cycle Mechanical Fatigue Performance of Sputtered Nitinol. Journal of Materials Engineering and Performance 1–9

33. Chluba C, Ge W, Dankwort T, et al (2016) Effect of crystallographic compatibility and grain size on the functional fatigue of sputtered TiNiCuCo thin films. Philosophical Transactions of the Royal Society A: Mathematical, Physical and Engineering Sciences 374:20150311

34. Jani JM, Leary M, Subic A, Gibson MA (2014) A review of shape memory alloy research, applications and opportunities. Materials & Design (1980-2015) 56:1078–1113

35. Gu H, Bumke L, Chluba C, et al (2018) Phase engineering and supercompatibility of shape memory alloys. Materials Today 21:265–277

36. Chluba C, Ossmer H, Zamponi C, et al (2016) Ultra-low fatigue quaternary TiNi-based films for elastocaloric cooling. Shape Memory and Superelasticity 2:95–103

37. Sharma N, Raj T, Jangra K (2015) Applications of nickel-titanium alloy. Journal of Engineering and Technology 5:1

38. Xue D, Yuan R, Zhou Y, et al (2016) Design of high temperature Ti-Pd-Cr shape memory alloys with small thermal hysteresis. Scientific reports 6:1–7

39. Karaca HE, Acar E, Tobe H, Saghaian SM (2014) NiTiHf-based shape memory alloys. Materials Science and Technology 30:1530–1544

40. Meng XL, Cai W, Chen F, Zhao LC (2006) Effect of aging on martensitic transformation and microstructure in Ni-rich TiNiHf shape memory alloy. Scripta materialia 54:1599–1604

41. Karakoc O, Hayrettin C, Bass M, et al (2017) Effects of upper cycle temperature on the actuation fatigue response of NiTiHf high temperature shape memory alloys. Acta Materialia 138:185–197

42. Karakoc O, Hayrettin C, Evirgen A, et al (2019) Role of microstructure on the actuation fatigue performance of Ni-Rich NiTiHf high temperature shape memory alloys. Acta Materialia 175:107–120

43. Meng XL, Cai W, Fu YD, et al (2010) Martensite structure in Ti--Ni--Hf--Cu quaternary alloy ribbons containing (Ti, Hf) 2Ni precipitates. Acta Materialia 58:3751–3763

44. Meng XL, Cai W, Wang LM, et al (2001) Microstructure of stress-induced martensite in a Ti--Ni--Hf high temperature shape memory alloy. Scripta materialia 45:1177–1182

45. Meng XL, Cai W, Zheng YF, et al (2002) Stress-induced martensitic transformation behavior of a Ti--Ni--Hf high temperature shape memory alloy. Materials Letters 55:111–115

46. Yi X, Meng X, Cai W, Zhao L (2019) Multi-stage martensitic transformation behaviors

and microstructural characteristics of Ti-Ni-Hf high temperature shape memory alloy powders. Journal of Alloys and Compounds 781:644–656

47. Tong Y, Shuitcev A, Zheng Y (2020) Recent development of TiNi-based shape memory alloys with high cycle stability and high transformation temperature. Advanced Engineering Materials 22:1900496

48. Fu YQ, Zhang S, Wu MJ, et al (2006) On the lower thickness boundary of sputtered TiNi films for shape memory application. Thin Solid Films 515:80–86

49. Kirchhof C, Krantz M, Teliban I, et al (2013) Giant magnetoelectric effect in vacuum. Applied Physics Letters 102:232905

50. Tong B, Yang X, Guo Z, et al (2013) Preparation and characterization of AlN/FeCoSiB magnetoelectric thin film composites. Ceramics International 39:6853–6859

51. Hayes P, Schell V, Salzer S, et al (2018) Electrically modulated magnetoelectric AlN/FeCoSiB film composites for DC magnetic field sensing. Journal of Physics D: Applied Physics 51:354002

52. Kim D-H, Lu N, Ma R, et al (2011) Epidermal Electronics. Science 333:838–843. https://doi.org/10.1126/science.1206157

53. Rogers JA, Someya T, Huang Y (2010) Materials and Mechanics for Stretchable Electronics. Science 327:1603–1607

54. Rogers JA, Huang Y (2009) A curvy, stretchy future for electronics. Proceedings of the National Academy of Sciences. https://doi.org/10.1073/pnas.0905723106

55. Choi S, Lee H, Ghaffari R, et al (2016) Recent advances in flexible and stretchable bio-electronic devices integrated with nanomaterials. Advanced materials 28:4203–4218

56. Xu S, Zhang Y, Cho J, et al (2013) Stretchable batteries with self-similar serpentine interconnects and integrated wireless recharging systems. Nature Communications. https://doi.org/10.1038/ncomms2553

57. Lee J, Wu J, Shi M, et al (2011) Stretchable GaAs photovoltaics with designs that enable high areal coverage. Advanced Materials 23:986–991. https://doi.org/10.1002/adma.201003961

58. Zhang Y, Fu H, Su Y, et al (2013) Mechanics of ultra-stretchable self-similar serpentine interconnects. Acta Materialia 61:7816–7827. https://doi.org/10.1016/j.actamat.2013.09.020

59. Lu N, Yang S (2015) Mechanics for stretchable sensors. Current Opinion in Solid State and Materials Science. https://doi.org/10.1016/j.cossms.2014.12.007

60. Alcheikh N, Shaikh SF, Hussain MM (2018) Ultra-stretchable Archimedean interconnects for stretchable electronics. Extreme Mechanics Letters 24:6–13

61. Lv C, Yu H, Jiang H (2014) Archimedean spiral design for extremely stretchable interconnects. Extreme Mechanics Letters 1:29–34

62. Lu N, Yang S (2015) Mechanics for stretchable sensors. Current Opinion in Solid State and Materials Science 19:149–159. https://doi.org/10.1016/j.cossms.2014.12.007

63. Widlund T, Yang S, Hsu Y-Y, Lu N (2014) Stretchability and compliance of freestanding serpentine-shaped ribbons. International Journal of Solids and Structures 51:4026–4037. https://doi.org/10.1016/J.IJSOLSTR.2014.07.025

64. Gray DS, Tien J, Chen CS (2004) High-Conductivity Elastomeric Electronics. Advanced Materials 16:393–397. https://doi.org/10.1002/adma.200306107

65. Pan T, Pharr M, Ma Y, et al (2017) Experimental and Theoretical Studies of Serpentine Interconnects on Ultrathin Elastomers for Stretchable Electronics. Advanced Functional Materials. https://doi.org/10.1002/adfm.201702589

66. Lazarus N, Meyer CD, Bedair SS (2015) Stretchable Inductor Design. IEEE Transactions on Electron Devices 62:1–1. https://doi.org/10.1109/TED.2015.2431221

67. Dong W, Cheng X, Xiong T, Wang X (2019) Stretchable bio-potential electrode with self-similar serpentine structure for continuous, long-term, stable ECG recordings. Biomedical Microdevices 21:6

68. Tompkins RP, Mahaboob I, Shahedipour-Sandvik F, Lazarus N (2016) Mechanical Analysis of Stretchable AlGaN/GaN High Electron Mobility Transistors. ECS Transactions 72.5:89–95. https://doi.org/10.1149/07205.0089ecst

69. Curtis SM, Tompkins RP, Nichols BM, et al (2019) Structural Anisotropy in Stretchable Silicon. Advanced Electronic Materials 5:1900003

70. Xue Z, Dong T, Zhu Z, et al (2018) Engineering in-plane silicon nanowire springs for highly stretchable electronics. Journal of Semiconductors 39:011001. https://doi.org/10.1088/1674-4926/39/1/011001

71. Mahaboob I, Marini J, Hogan K, et al (2018) Selective Area Epitaxial Growth of Stretchable Geometry AlGaN-GaN Heterostructures. Journal of Electronic Materials 47:6625–6634

72. Tompkins RP, Mahaboob I, Shahedipour-Sandvik F, Lazarus N (2017) Electrical properties of AlGaN/GaN HEMTs in stretchable geometries. Solid-State Electronics 136:36–42

73. Tompkins RP, Mahaboob I, Shahedipour-Sandvik F, Lazarus N (2017) Electrical properties of AlGaN/GaN HEMTs in stretchable geometries. Solid-State Electronics 136:36–42. https://doi.org/10.1016/j.sse.2017.06.014

74. Zhao Y, Zhou W, Shi Y, et al (2022) Superelastic alloy based electrical interconnects for highly stretchable electronics. npj Flexible Electronics 6:1–8

75. Ren X, Das R, Tran P, et al (2018) Auxetic metamaterials and structures: a review. Smart materials and structures 27:23001

76. Saxena KK, Das R, Calius EP (2016) Three decades of auxetics research- materials with negative Poisson's ratio: a review. Advanced Engineering Materials 18:1847–1870

77. Bhullar SK, Ko J, Ahmed F, Jun MBG (2014) Design and fabrication of stent with negative Poisson's ratio. International Journal of Mechanical and Mechatronics Engineering 8:448–454

78. Bhullar SK, Lekesiz H, Karaca AA, et al (2022) Characterizing the Mechanical Performance of a Bare-Metal Stent with an Auxetic Cell Geometry. Applied Sciences 12:910

79. Jiang Y (2019) Auxetic mechanical metamaterial based stretchable electronics Doctoral thesis, Nanyang Technological University, Singapore

80. Grima-Cornish JN, Grima JN, Attard D (2020) A Novel Mechanical Metamaterial Exhibiting Auxetic Behavior and Negative Compressibility. Materials 13:79

81. Grima JN, Manicaro E, Attard D (2011) Auxetic behaviour from connected different-sized squares and rectangles. Proceedings of the Royal Society A: Mathematical, Physical and Engineering Sciences 467:439–458

82. Dengiz D, Goldbeck H, Curtis SM, et al (2023) Shape memory alloy thin film auxetic structures. Advanced Materials Technology 2201991:1–9

83. Hassanin H, Abena A, Elsayed MA, Essa K (2020) 4D printing of NiTi auxetic structure with improved ballistic performance. Micromachines 11:745

84. Jacobs S, Coconnier C, DiMaio D, et al (2012) Deployable auxetic shape memory alloy cellular antenna demonstrator: design, manufacturing and modal testing. Smart materials and structures 21:75013

85. Yarar E, Fichtner S, Hayes P, et al (2019) MEMS-Based AlScN Resonating Energy Harvester With Solidified Powder Magnet. Journal of Microelectromechanical Systems 28:1019–1031

86. Leung CM, Li J, Viehland D, Zhuang X (2018) A review on applications of magnetoelectric composites: from heterostructural uncooled magnetic sensors, energy harvesters to highly efficient power converters. Journal of Physics D: Applied Physics 51:263002

87. Tu C, Chu Z-Q, Spetzler B, et al (2019) Mechanical-Resonance-Enhanced Thin-Film Magnetoelectric Heterostructures for Magnetometers, Mechanical Antennas, Tunable RF Inductors, and Filters. Materials 12:2259

88. Srinivasan G, Priya S, Sun N (2015) Composite magnetoelectrics: materials, structures, and applications. Elsevier Science

89. Xi H, Qian X, Lu M-C, et al (2016) A room temperature ultrasensitive magnetoelectric susceptometer for quantitative tissue iron detection. Scientific reports 6:29740

90. Röbisch V, Salzer S, Urs NO, et al (2017) Pushing the detection limit of thin film magnetoelectric heterostructures. Journal of Materials Research 32:1009–1019

91. Jahns R, Piorra A, Lage E, et al (2013) Giant Magnetoelectric Effect in Thin-Film Composites. Journal of the American Ceramic Society 96:1673–1681

92. Zhao P, Zhao Z, Hunter D, et al (2009) Fabrication and characterization of all-thin-film magnetoelectric sensors. Applied Physics Letters 94:243507

93. Deuschl G, Agid Y (2013) Subthalamic neurostimulation for Parkinson's disease with early fluctuations: balancing the risks and benefits. The Lancet Neurology 12:1025–1034

94. Group D-BS for PDS (2001) Deep-brain stimulation of the subthalamic nucleus or the pars interna of the globus pallidus in Parkinson's disease. New England Journal of Medicine 345:956–963

95. Schuepbach WMM, Rau J, Knudsen K, et al (2013) Neurostimulation for Parkinson's disease with early motor complications. New England Journal of Medicine 368:610–622

96. Johnson Matthey Medical Components, Nitinol Technical Properties. https://matthey.com/en/markets/pharmaceutical-and-medical/medical-device-components/resource-library/nitinol-technical-properties

97. Röbisch V, Piorra A, de Miranda R, et al (2018) Frequency-tunable nickel-titanium substrates for magnetoelectric sensors. AIP Advances 8:125320

98. Kohl M, Dittmann D, Quandt E, Winzek B (2000) Thin film shape memory microvalves with adjustable operation temperature. Sensors and Actuators A: Physical 83:214–219

99. Vitushinsky R, Schmitz S, Ludwig A (2008) Bistable thin-film shape memory actuators for applications in tactile displays. Journal of Microelectromechanical Systems 18:186–194

100. Quandt E, Halene C, Holleck H, et al (1996) Sputter deposition of TiNi, TiNiPd and TiPd films displaying the two-way shape-memory effect. Sensors and Actuators A: Physical 53:434–439

101. Fu Y, Huang W, Du H, et al (2001) Characterization of TiNi shape-memory alloy thin films for MEMS applications. Surface and Coatings Technology 145:107–112

102. Fu Y, Du H, Zhang S, Gu Y (2005) Stress and surface morphology of TiNiCu thin films: effect of annealing temperature. Surface and Coatings Technology 198:389–394

103. Zannon M (2014) Free Vibration of Thin Film Cantilever Beam. International Journal of Engineering and Technical Research (IJETR) 2:304–314

104. Whitney S (1999) Vibrations of cantilever beams: Deflection, frequency, and research uses. Website 1-9

105. Šittner P, Heller L, Pilch J, et al (2014) Young's modulus of austenite and martensite phases in superelastic NiTi wires. Journal of materials engineering and performance 23:2303–2314

106. Hopcroft MA, Nix WD, Kenny TW (2010) What is the Young's Modulus of Silicon? JOURNAL OF MICROELECTROMECHANICAL SYSTEMS 19(2): 229-238 https://doi.org/10.1109/JMEMS.2009.2039697

107. Zabel S, Kirchhof C, Yarar E, et al (2015) Phase modulated magnetoelectric delta-E effect sensor for sub-nano tesla magnetic fields. Applied Physics Letters 107:152402

108. Hong Y, Sui L, Zhang M, Shi G (2018) Theoretical analysis and experimental study of the effect of the neutral plane of a composite piezoelectric cantilever. Energy Conversion and Management 171:1020–1029

109. Yarar E, Hrkac V, Zamponi C, et al (2016) Low temperature aluminum nitride thin films for sensory applications. AIP Advances 6:75115

110. Hrkac V, Lage E, Köppel G, et al (2014) Amorphous FeCoSiB for exchange bias coupled and decoupled magnetoelectric multilayer systems: Real-structure and magnetic properties. Journal of Applied Physics 116:134302

111. Yarar E, Salzer S, Hrkac V, et al (2016) Inverse bilayer magnetoelectric thin film sensor. Applied Physics Letters 109:22901

112. Piorra A, Jahns R, Teliban I, et al (2013) Magnetoelectric thin film composites with interdigital electrodes. Applied Physics Letters 103:32902

113. Evans KL, Liaw HM, Lin J-K (1996) Method for enhancing aluminum nitride U.S. Patent No. 5,520,785.

114. Pawar S, Singh K, Sharma S, et al (2018) Growth assessment and scrutinize dielectric reliability of c-axis oriented insulating AlN thin films in MIM structures for microelectronics applications. Materials Chemistry and Physics 219:74–81

115. Iqbal A, Mohd-Yasin F (2018) Reactive sputtering of aluminum nitride (002) thin films for piezoelectric applications: A review. Sensors 18:1797

116. Prume K, Tiedke S, Schmitz-Kempen T (2010) Double-Beam and four-point. Mikroniek nr 4:31–35

117. Burianova L, Bowen CR, Prokopova M, Sulc M (2005) Laser interferometric displacement measurements of multi-layer actuators and PZT ceramics. Ferroelectrics 320:161–169

118. Dankwort T, Strobel J, Chluba C, et al (2016) Martensite adaption through epitaxial nano transition layers in TiNiCu shape memory alloys. Journal of Applied Crystallography 49:1009–1015

119. Frenzel J, Wieczorek A, Opahle I, et al (2015) On the effect of alloy composition on martensite start temperatures and latent heats in Ni--Ti-based shape memory alloys. Acta Materialia 90:213–231

120. Pohl M, Heßing C, Frenzel J (2004) Electrolytic processing of NiTi shape memory alloys. Materials Science and Engineering: A 378:191–199

121. Durdaut P, Salzer S, Reermann J, et al (2017) Thermal-mechanical noise in resonant thin-film magnetoelectric sensors. IEEE Sensors Journal 17:2338–2348

122. Lee H-J, Ni H, Wu DT, Ramirez AG (2005) Grain size estimations from the direct measurement of nucleation and growth. Applied Physics Letters 87:124102

123. Mehrer H (2007) Diffusion in solids: fundamentals, methods, materials, diffusion-controlled processes. Springer Science & Business Media

124. Kaur I, Gust W, Kozma L (1989) Handbook of grain and interphase boundary diffusion data. Ziegler Press Stuttgart

125. Neumann G, Tuijn C (2011) Self-diffusion and impurity diffusion in pure metals: handbook of experimental data. Elsevier

126. Tisone TC, Drobek J (1972) Diffusion in thin film Ti--Au, Ti--Pd, and Ti--Pt couples. Journal of Vacuum Science and Technology 9:271–275

127. Murray JL (1981) The Ta- Ti (Tantalum-Titanium) system. Bulletin of Alloy Phase Diagrams 2:62–66

128. Waterstrat RM (1981) Analysis of selected alloys in the systems Cr-Pd, Cr-Ru, V-Pd and Ta-Pt. Journal of the Less Common Metals 80:P31--P36

129. Murray JL (1982) The Pt- Ti (Platinum- Titanium) system. Bulletin Of Alloy Phase Diagrams 3:329–335

130. Larson JM, Taggart R, Polonis DH (1970) Ni 8 Ta in nickel-rich Ni- Ta alloys. Metallurgical and Materials Transactions B 1:485–489

131. Subramanian PR, Laughlin DE (1989) The Cu-Ta (copper-tantalum) system. Bulletin of alloy phase diagrams 10:652–655

132. Errando-Herranz C, Takabayashi AY, Edinger P, et al (2019) MEMS for photonic integrated circuits. IEEE Journal of Selected Topics in Quantum Electronics 26:1–16

133. Ollier E (2002) Optical MEMS devices based on moving waveguides. IEEE Journal of selected topics in quantum electronics 8:155–162

134. Lee H-T, Kim M-S, Lee G-Y, et al (2018) Shape memory alloy (sma)-based microscale actuators with 60\% deformation rate and 1.6 kHz actuation speed. Small 14:1801023

135. König D, Zarnetta R, Savan A, et al (2011) Phase transformation, structural and functional fatigue properties of Ti--Ni--Hf shape memory thin films. Acta Materialia 59:3267–3275

136. Karaca HE, Saghaian SM, Ded G, et al (2013) Effects of nanoprecipitation on the shape memory and material properties of an Ni-rich NiTiHf high temperature shape memory alloy. Acta Materialia 61:7422–7431

137. Winzek B, Schmitz S, Rumpf H, et al (2004) Recent developments in shape memory thin film technology. Materials Science and Engineering: A 378:40–46

138. Watanabe H, Yamada N, Okaji M (2004) Linear thermal expansion coefficient of silicon from 293 to 1000 K. International journal of thermophysics 25:221–236

139. Shuitcev A, Vasin RN, Fan XM, et al (2020) Volume effect upon martensitic transformation in Ti29. 7Ni50. 3Hf20 high temperature shape memory alloy. Scripta Materialia 178:67–70

140. Shuitcev A, Vasin RN, Balagurov AM, et al (2020) Thermal expansion of martensite in Ti29. 7Ni50. 3Hf20 shape memory alloy. Intermetallics 125:106889

141. Winzek B, Schmitz S, Vitushinsky R (2004) Shape Memory Actuators in Mobile Robots

for Planetary Surface Exploration. In: Tools and Technologies for Future Planetary Exploration. pp 115–120

142. Evirgen A, Karaman I, Santamarta R, et al (2016) Relationship between crystallographic compatibility and thermal hysteresis in Ni-rich NiTiHf and NiTiZr high temperature shape memory alloys. Acta Materialia 121:374–383

143. Motemani Y, McCluskey PJ, Zhao C, et al (2011) Analysis of Ti--Ni--Hf shape memory alloys by combinatorial nanocalorimetry. Acta materialia 59:7602–7614

144. Meng XL, Zheng YF, Cai W, Zhao LC (2004) Two-way shape memory effect of a TiNiHf high temperature shape memory alloy. Journal of alloys and compounds 372:180–186

145. Meng XL, Cai W, Fu YD, et al (2008) Shape-memory behaviors in an aged Ni-rich TiNiHf high temperature shape-memory alloy. Intermetallics 16:698–705

146. Mandepudi SK, Ackler HD (2010) Processing and characterization of composite shape memory alloy (SMA) thin film structures for microactuators. In: Behavior and Mechanics of Multifunctional Materials and Composites 2010. p 76440N

147. Grummon DS (2003) Thin-film shape-memory materials for high-temperature applications. JOM 55:24–32

148. Waitz T, Kazykhanov V, Karnthaler HP (2004) Martensitic phase transformations in nanocrystalline NiTi studied by TEM. Acta Materialia 52:137–147

149. Ishida A, Sato M (2003) Thickness effect on shape memory behavior of Ti-50.0 at.\% Ni thin film. Acta Materialia 51:5571–5578

150. König D, Ehmann M, Thienhaus S, Ludwig A (2010) Micro-to nanostructured devices for the characterization of scaling effects in shape-memory thin films. Journal of Microelectromechanical Systems 19:1264–1269

151. Winzek B, Sterzl T, Rumpf H, Quandt E (2003) Composites of different shape memory alloys and polymers for complex actuator motions. In: Journal de Physique IV (Proceedings). pp 1163–1168

152. Sanjabi S, Cao YZ, Barber ZH (2005) Multi-target sputter deposition of Ni50Ti50- xHfx shape memory thin films for high temperature microactuator application. Sensors and Actuators A: Physical 121:543–548

153. Sedlák P, Frost M, Benešová B, et al (2012) Thermomechanical model for NiTi-based shape memory alloys including R-phase and material anisotropy under multi-axial loadings. International Journal of Plasticity 39:132–151. https://doi.org/https://doi.org/10.1016/j.ijplas.2012.06.008

154. Sielenkämper M, Wulfinghoff S (2022) A thermomechanical finite strain shape memory alloy model and its application to bistable actuators. Acta Mechanica 233:3059–3094

155. Hurtado DE, Stainier L, Ortiz M (2014) The special-linear update: An application of differential manifold theory to the update of isochoric plasticity flow rules. International Journal for Numerical Methods in Engineering 97:298–312.

https://doi.org/https://doi.org/10.1002/nme.4600

156. Sielenkämper M, Dittmann J, Wulfinghoff S Numerical strategies for variational updates in large strain inelasticity with incompressibility constraint. International Journal for Numerical Methods in Engineering n/a: https://doi.org/https://doi.org/10.1002/nme.6855

157. Halphen B, Nguyen QS (1975) Sur les matériaux standard généralisés. Journal de mécanique 14(1): 39-63

158. Yang Q, Stainier L, Ortiz M (2006) A variational formulation of the coupled thermo-mechanical boundary-value problem for general dissipative solids. Journal of the Mechanics and Physics of Solids 54:401–424. https://doi.org/https://doi.org/10.1016/j.jmps.2005.08.010

159. Lexcellent C, Boubakar ML, Bouvet C, Calloch S (2006) About modelling the shape memory alloy behaviour based on the phase transformation surface identification under proportional loading and anisothermal conditions. International Journal of Solids and Structures 43:613–626. https://doi.org/https://doi.org/10.1016/j.ijsolstr.2005.07.004

160. Panico M, Brinson LC (2007) A three-dimensional phenomenological model for martensite reorientation in shape memory alloys. Journal of the Mechanics and Physics of Solids 55:2491–2511. https://doi.org/https://doi.org/10.1016/j.jmps.2007.03.010

161. Taylor RL (2017) {FEAP} - Finite Element Analysis Program

162. Tabesh M, Lester B, Hartl D, Lagoudas D (2012) Influence of the latent heat of transformation and thermomechanical coupling on the performance of shape memory alloy actuators. In: Smart Materials, Adaptive Structures and Intelligent Systems. pp 237–248

163. Turner TL (2001) Thermomechanical response of shape memory alloy hybrid composites. National Aeronautics and Space Administration, Langley Research Center

164. Uchil J, Fernandes FMB, Mahesh KK (2007) X-ray diffraction study of the phase transformations in NiTi shape memory alloy. Materials characterization 58:243–248

165. Zamkovskaya A, Maksimova E, Nauhatsky I, Shapoval M (2017) X-ray diffraction investigations of the thermal expansion of iron borate FeBO3 crystals. In: Journal of Physics: Conference Series. p 12030

166. Qiu S, Krishnan VB, Padula SA, et al (2009) Measurement of the lattice plane strain and phase fraction evolution during heating and cooling in shape memory NiTi. Applied Physics Letters 95:141906

167. Fryer DS, Peters RD, Kim EJ, et al (2001) Dependence of the glass transition temperature of polymer films on interfacial energy and thickness. Macromolecules 34:5627–5634

168. Lan T, Torkelson JM (2014) Methacrylate-based polymer films useful in lithographic applications exhibit different glass transition temperature-confinement effects at high and low molecular weight. Polymer 55:1249–1258

169. Kahle O, Wielsch U, Metzner H, et al (1998) Glass transition temperature and thermal

expansion behaviour of polymer films investigated by variable temperature spectroscopic ellipsometry. Thin solid films 313:803–807

170. Reese S, Govindjee S (1997) Theoretical and numerical aspects in the thermo-viscoelastic material behaviour of rubber-like polymers. Mechanics of Time-Dependent Materials 1:357–396

171. Goods SH (2003) Thermal expansion and hydration behavior of PMMA moulding materials for LIGA (No. SAND2003-8000). Sandia National Lab.(SNL-NM), Albuquerque, NM (United States); Sandia National Lab.(SNL-CA), Livermore, CA (United States).

172. Hopcroft MA, Nix WD, Kenny TW (2010) What is the Young's Modulus of Silicon? Journal of microelectromechanical systems 19:229–238

173. Kohl M, Krevet B, Just E (2002) SMA microgripper system. Sensors and Actuators A: Physical 97–98:646–652. https://doi.org/https://doi.org/10.1016/S0924-4247(01)00803-2

174. Zhang Y, Li M, Wang YD, et al (2014) Superelasticity and Serration Behavior in Small-Sized NiMnGa Alloys. Advanced Engineering Materials 16:955–960

175. Jarrige I, Holliger P, Jonnard P (2004) Diffusion processes in NiTi/Si, NiTi/SiO2 and NiTi/Si3N4 systems under annealing. Thin Solid Films 458:314–321

176. Lega P, Nedospasov I, Orlov A, et al (2019) On the Fundamental Limits of the Size of the Shape Memory Nanoactuators Posed by Martensitic Transition in Ti2NiCu Shape Memory Alloy on Nano-Scale. In: 2019 IEEE International Conference on Manipulation, Manufacturing and Measurement on the Nanoscale (3M-NANO). pp 90–93

177. Benafan O, Noebe RD, Padula SA, Vaidyanathan R (2012) Microstructural response during isothermal and isobaric loading of a precipitation-strengthened Ni-29.7 Ti-20Hf high-temperature shape memory alloy. Metallurgical and materials Transactions A 43:4539–4552

178. Kohl M, Krevet B (2002) 3D simulation of a shape memory microactuator. Materials Transactions 43:1030–1036

179. Potapov PL, Shelyakov A V, Gulyaev AA, et al (1997) Effect of Hf on the structure of Ni-Ti martensitic alloys. Materials Letters 32:247–250

180. Kim D-H, Ghaffari R, Lu N, Rogers JA (2012) Flexible and Stretchable Electronics for Biointegrated Devices. Annual Review of Biomedical Engineering 14:113–128. https://doi.org/10.1146/annurev-bioeng-071811-150018

181. Xu S, Zhang Y, Cho J, et al (2013) Stretchable batteries with self-similar serpentine interconnects and integrated wireless recharging systems. Nature Communications 4:1543. https://doi.org/10.1038/ncomms2553

182. Chortos A, Liu J, Bao Z (2016) Pursuing prosthetic electronic skin. Nature materials 15:937–950

183. Wang Y, Li Z, Xiao J (2016) Stretchable Thin Film Materials: Fabrication, Application,

and Mechanics. Journal of Electronic Packaging. https://doi.org/10.1115/1.4032984

184. Fan Z, Zhang Y, Ma Q, et al (2016) A finite deformation model of planar serpentine interconnects for stretchable electronics. International Journal of Solids and Structures 91:46–54. https://doi.org/10.1016/j.ijsolstr.2016.04.030

185. Gonzalez M, Axisa F, Bulcke M Vanden, et al (2008) Design of metal interconnects for stretchable electronic circuits. Microelectronics Reliability 48:825–832. https://doi.org/10.1016/j.microrel.2008.03.025

186. Zhang Y, Xu S, Fu H, et al (2013) Buckling in serpentine microstructures and applications in elastomer-supported ultra-stretchable electronics with high areal coverage. Soft Matter 9:8062. https://doi.org/10.1039/c3sm51360b

187. Hayes GJ, So J-H, Qusba A, et al (2012) Flexible liquid metal alloy (EGaIn) microstrip patch antenna. IEEE transactions on Antennas and Propagation 60:2151–2156

188. Zhang Y, Wang S, Li X, et al (2014) Experimental and theoretical studies of serpentine microstructures bonded to prestrained elastomers for stretchable electronics. Advanced Functional Materials 24:2028–2037

189. Fan JA, Yeo W-H, Su Y, et al (2014) Fractal design concepts for stretchable electronics. Nature communications 5:1–8

190. Kim D-H, Liu Z, Kim Y-S, et al (2009) Optimized structural designs for stretchable silicon integrated circuits. Small 5:2841–2847

191. Bechtold C, de Miranda RL, Chluba C, Quandt E (2016) Fabrication of self-expandable NiTi thin film devices with micro-electrode array for bioelectric sensing, stimulation and ablation. Biomedical microdevices 18:106

192. Fu Y, Du H, Huang W, et al (2004) TiNi-based thin films in MEMS applications: a review. Sensors and Actuators A: Physical 112:395–408

193. Bumke L, Zamponi C, Jetter J, Quandt E (2020) Cu-Rich Ti52. 8Ni22. 2Cu22. 5Co2. 5 Shape Memory Alloy Films with Ultra-Low Fatigue for Elastocaloric Applications. Journal of Applied Physics 127:225105

194. Mech K, Kowalik R, Żabiński P (2011) Cu thin films deposited by DC magnetron sputtering for contact surfaces on electronic components. Archives of Metallurgy and materials 56:903–908

195. Pan C, Kumar K, Li J, et al (2018) Visually imperceptible liquid-metal circuits for transparent, stretchable electronics with direct laser writing. Advanced Materials 30:1706937

196. Su Y, Ping X, Yu KJ, et al (2017) In-Plane Deformation Mechanics for Highly Stretchable Electronics. Advanced Materials 29:1604989

197. Bruederlin F, Ossmer H, Wendler F, et al (2017) SMA foil-based elastocaloric cooling: from material behavior to device engineering. Journal of Physics D: Applied Physics 50:424003

198. Cui J, Chu YS, Famodu OO, et al (2006) Combinatorial search of thermoelastic shape-memory alloys with extremely small hysteresis width. Nature materials 5:286–290

199. Ossmer H, Chluba C, Gueltig M, et al (2015) Local evolution of the elastocaloric effect in TiNi-based films. Shape Memory and Superelasticity 1:142–152

200. Morgiel J, Cesari E, Pons J, et al (2002) Microstructure and martensite transformation in aged Ti-25Ni-25Cu shape memory melt spun ribbons. Journal of materials science 37:5319–5325

201. Jiang H, Lv C, Yu H (2020) Archimedean spiral design for deformable electronics. U.S. Patent No. 10,660,200.

202. Ossmer H, Chluba C, Kauffmann-Weiss S, et al (2016) TiNi-based films for elastocaloric microcooling—fatigue life and device performance. APL Materials 4:64102

203. Bumke L, Chluba C, Ossmer H, et al (2018) Cobalt Gradient Evolution in Sputtered TiNiCuCo Films for Elastocaloric Cooling. physica status solidi (b) 255:1700299

204. Bruederlin F, Bumke L, Chluba C, et al (2018) Elastocaloric cooling on the miniature scale: a review on materials and device engineering. Energy Technology 6:1588–1604

205. Lazarus N, Meyer CD, Bedair SS, et al (2015) Magnetic elastomers for stretchable inductors. ACS Applied Materials and Interfaces 7:10080–10084. https://doi.org/10.1021/acsami.5b02189

206. Yihui Zhang , Shuodao Wang , Xuetong Li , Jonathan A. Fan SX, Young Min Song , Ki-Joong Choi , Woon-Hong Yeo WL, Sharaf Nafees Nazaar , Bingwei Lu , Lan Yin , Keh-Chih Hwang JAR, and Yonggang Huang (2013) Experimental and Theoretical Studies of Serpentine Microstructures Bonded to Prestrained Elastomers for Stretchable Electronics. Adv Funct Mater

207. Frenzel J (2020) On the importance of structural and functional fatigue in shape memory technology. Shape Memory and Superelasticity 6:213–222

208. Curtis SM, Wang H, Anfinrud GP, et al (2020) Deformable Array of Semiconductor Devices U.S. Patent Application No. 16/668,715.

209. Curtis SM, et al., “Superelastic Sputtered TiNiCuCo Thin Film Serpentine Interconnects for Wearable Electronics” Oral Presentation at Fall MRS 2019 (Boston, MA) (12/2019)

210. Curtis SM, et al., “Multifunctional Sputtered NiTi Thin Film Stretchable Electrodes for Wearable Electronics” Oral Presentation at SMST (Konstanz, Germany) (05/2019)

211. Curtis SM, Dengiz D, Quandt E (2022) AUXETISCHE STEG- ODER FELDSTRUKTUR SOWIE VERWENDUNG Patent Application No. PCT/DE2022/100001

212. Lvov VA, Senatov FS, Veveris AA, et al (2022) Auxetic Metamaterials for Biomedical Devices: Current Situation, Main Challenges, and Research Trends. Materials 15:1439

213. Lu N, Wang X, Suo Z, Vlassak J (2007) Metal films on polymer substrates stretched beyond 50%. Applied Physics Letters 91:221909. https://doi.org/10.1063/1.2817234

214. Curtis SM, Gugat JL, Bumke L, et al (2023) Thin-Film Superelastic Alloys for Stretchable Electronics. Shape Memory and Superelasticity pp. 1–15

215. Meena K, Singamneni S (2019) A new auxetic structure with significantly reduced stress concentration effects. Materials & Design 173:107779

216. Bechtold C, de Miranda RL, Chluba C, et al (2016) Method for fabricating miniaturized NiTi self-expandable thin film devices with increased radiopacity. Shape Memory and Superelasticity 2:391–398

217. Velvaluri P, Soor A, Plucinsky P, et al (2021) Origami-inspired thin-film shape memory alloy devices. Scientific reports 11:1–10

218. Dmytriw AA, Salem MM, Yang VXD, et al (2020) Endosaccular flow disruption: a new frontier in endovascular aneurysm management. Neurosurgery 86:170–181

219. Lebedev GA, Gusarov B V, Viala B, et al (2011) Thermal energy harvesting using shape memory/piezoelectric composites. In: 2011 16th International Solid-State Sensors, Actuators and Microsystems Conference. pp 669–670

220. Gusarov B, Gusarova E, Viala B, et al (2016) Thermal energy harvesting by piezoelectric PVDF polymer coupled with shape memory alloy. Sensors and Actuators A: Physical 243:175–181

221. Sukumaran S (2021) Design and preparation of a micro-harvesting device made of hybrid SMA/Piezoelectric polymer composite. Doctoral dissertation - Université de Lorraine

222. Kim HA, Betts DN, Salo AIT, Bowen CR (2010) Shape memory alloy-piezoelectric active structures for reversible actuation of bistable composites. AIAA journal 48:1265–1268

223. Lester BT, Baxevanis T, Chemisky Y, Lagoudas DC (2015) Review and perspectives: shape memory alloy composite systems. Acta Mechanica 226:3907–3960

224. Aïssa KA, Elmazria O, Boulet P, et al (2015) Investigations of AlN thin film crystalline properties in a wide temperature range by in situ X-ray diffraction measurements: correlation with AlN/sapphire-based SAW structure performance. IEEE Transactions on Ultrasonics, Ferroelectrics, and Frequency Control 62:1397–1402

225. Liu S, Ha T, Lu N (2019) Experimentally and numerically validated analytical solutions to nonbuckling piezoelectric serpentine ribbons. Journal of Applied Mechanics 86(5): 051010

226. Arivanandhan G, Li Z, Curtis SM, et al (2023) Power Optimization of TiNiHf/Si Shape Memory Microactuators. Actuators. 12(2): 82, MDPI